

2013

Digital Image-Based Frameworks for Monitoring and Controlling of Particulate Systems

Bing Zhang

Louisiana State University and Agricultural and Mechanical College

Follow this and additional works at: https://repository.lsu.edu/gradschool_dissertations



Part of the [Chemical Engineering Commons](#)

Recommended Citation

Zhang, Bing, "Digital Image-Based Frameworks for Monitoring and Controlling of Particulate Systems" (2013). *LSU Doctoral Dissertations*. 2561.

https://repository.lsu.edu/gradschool_dissertations/2561

This Dissertation is brought to you for free and open access by the Graduate School at LSU Scholarly Repository. It has been accepted for inclusion in LSU Doctoral Dissertations by an authorized graduate school editor of LSU Scholarly Repository. For more information, please contact gradetd@lsu.edu.

DIGITAL IMAGE-BASED FRAMEWORKS FOR MONITORING AND CONTROLLING OF PARTICULATE SYSTEMS

A Dissertation

Submitted to the Graduate Faculty of the
Louisiana State University and
Agricultural and Mechanical College
in partial fulfillment of the
requirements for the degree of
Doctor of Philosophy

in

The Gordon A. and Mary Cain
Department of Chemical Engineering

by

Bing Zhang

B.ChE., Wuhan University of Science and Technology, 2003

M.S., Tsinghua University, 2006

May 2013

©Copyright 2013
Bing Zhang
All rights reserved

ACKNOWLEDGEMENTS

I want to thank my research advisor, Professor Jose A. Romagnoli, for his guidance during my doctoral studies. I also thank him for allowing me to tailor my research as I saw fit, and allowing me to take additional classes to enrich my educational experience.

Secondly, I want to thank Dr. Ali Abbas for the immense amount of work that he did for me during my doctoral studies. His feedback was essential in helping me publish the number of papers that I did.

I also want to thank members of my committee, Professors, John Flake, Francisco Hung, Karsten Thompson and my Dean's Representative, Professor Jerome Hoffman for their helpful feedback during my studies.

I want to thank all of my current and former labmates for providing helpful advice while I was performing my research. In particular, David Widenski and Giuseppe Cogoni helped perform experiments and data analysis. Thank Gregory Robertson and Paritosh Sharma for helping me prepare presentations and for giving general life advice.

I also want to thank the members of the chemical engineering administrative staff. In particular, I want to thank Rob Willis for computer application and hardware support, Darla Dao for financial reimbursement and supply ordering support, and Melanie McCandless and Melissa Fay for administrative support.

Lastly, I'd like to thank my family for being supportive while I pursued my degree. In particular I want to mention, my mother Shanping Dong and my father Fangxin Zhang who were extremely supportive during my studies, and who I know are extremely proud of my accomplishment.

TABLE OF CONTENTS

COPYRIGHT	ii
ACKNOWLEDGEMENTS	iii
LIST OF TABLES	vii
LIST OF FIGURES	viii
ABSTRACT	xi
CHAPTER 1. INTRODUCTION	1
1.1 Problem Statement	1
1.2 Dissertation Motivation	4
1.3 Aims and Contributions of This Dissertation	5
1.4 Structure of This Dissertation	7
1.5 References	10
CHAPTER 2. MULTI-RESOLUTION FUZZY CLUSTERING APPROACH FOR IMAGE- BASED PARTICLE CHARACTERIZATION FOR PARTICLE SYSTEMS MONITORING AND CONTROL	13
2.1 Introduction	13
2.2 Image Analysis by Wavelet Transform	15
2.2.1 Discrete Wavelet Transformation	16
2.2.2 Multi-resolution Analysis and Discrete Function	17
2.2.3 2D Discrete Wavelet Transformation	18
2.2.4 Image Multi-Resolution Denoising	19
2.2.5 The Choice of Wavelet Function and Wavelet Decomposition Level	20
2.3 Clustering Pixel Intensity Values	23
2.3.1 Fuzzy C-Mean Clustering	23
2.3.2 Fuzzy Range Clustering	25
2.4 Methodology for Particle Image Segmentation	26
2.5 Case Study	26
2.5.1 Imaging Setup Used in the Present Study	27
2.5.2 Application	28
2.5.3 Equivalent Diameter and PSD	33
2.6 Architecture of the Image-Based Controlling and Monitoring Framework	37
2.7 Conclusions	40
2.8 References	40
CHAPTER 3. SEPARATION OF TOUCHING AND OVERLAPPING OBJECTS IN PARTICULATE IMAGES BY COMBINING INTENSITY AND GEOMETRY CHARACTERISTICS	42
3.1 Introduction	42
3.2 Image Pre-Processing	43
3.3 Segmentation	45

3.3.1 Thresholding	45
3.3.2 Separate through Intensity Features	46
3.2.3 Separate Combining Geometric Features	48
3.4 Methodology	51
3.5 Case Study	53
3.5.1 Smoothing Strategy on Particle Images	53
3.5.2 Segmentation by Thresholding on Particle Images	56
3.5.3 Segmentation Using Valley Points on Particle Images.....	57
3.5.4 Complete Segmentation Using Geometric Features	59
3.6 Results and Discussion	60
3.6.1 Compare with Watershed Method	60
3.6.2 Compare with Manual Measurement.....	61
3.7 Conclusions.....	64
3.8 References.....	64
CHAPTER 4. AUTOMATIC IMAGE-BASED ESTIMATION OF TEXTURE ANALYSIS AS A MONITORING TOOL FOR CRYSTAL GROWTH	66
4.1 Introduction.....	66
4.2 Thresholding Method.....	70
4.3 Texture Analysis by Wavelet Transform.....	70
4.3.1 Wavelet Energy Signature	71
4.3.2 Fractal-Wavelet Feature.....	72
4.4 Method for Texture Analysis from Crystal Images	74
4.4.1 Methodology.....	74
4.4.2 Case Study	75
4.5 The Relationship between Fractal Dimension and Crystal Growth.....	79
4.6 Conclusions.....	81
4.7 References.....	82
CHAPTER 5. MULTI-RESOLUTION-MULTIVARIATE STATISTICAL IMAGE BASED APPROACH FOR CRYSTAL MEAN SIZE PREDICTION/CHARACTERIZATION	84
5.1 Introduction.....	84
5.2 Crystal Mean Size Prediction.....	84
5.2.1 Partial Least Squares.....	85
5.2.2 Application.....	87
5.3 Crystal Size Detection.....	92
5.3.1 Principal Components Analysis.....	93
5.3.2 Methodology for Size Characterization	97
5.3.3 Case Study of Anti-Solvent Crystallization.....	98
5.4 Conclusions.....	106
5.5 References.....	106
CHAPTER 6. IMAGE-BASED MULTI-RESOLUTION-ANN APPROACH FOR ON-LINE PARTICLE SIZE DISTRIBUTION CHARACTERIZATION.....	108
6.1 Introduction.....	108

6.2 Artificial Neural Network	109
6.3 Methodology of Image-Based Multi-Resolution Sensor	113
6.4 Case Study	115
6.4.1 Experiment	115
6.4.2 Image Acquisition System	117
6.4.3 The Relationship between FD and Crystal Growth at Different Process Conditions	117
6.4.4 ANN Models and Prediction	119
6.5 Conclusions	128
6.6 References	129
 CHAPTER 7. CONCLUSIONS & RECOMMENDATIONS	131
7.1 Conclusions	131
7.2 Future Work	133
 APPENDIX: LETTERS OF PERMISSION	134
 VITA	142

LIST OF TABLES

Table 2.1 Shannon Entropy (1.000e+004) for different wavelet functions and decomposition levels. The minimum values are highlighted in bold	30
Table 2.2 Particle equivalent diameter.....	35
Table 4.1 Detail variance and its 2-base logarithm at four decomposition level.....	79
Table 4.2 The mean Hurst exponent, mean FD and manually measured mean size at each growth stage	81
Table 5.1 Texture analysis results and mean size prediction for training data	90
Table 5.2 Texture analysis results and mean size prediction for testing data	92
Table 5.3 Crystal mean size and Q statistics for each stage	106
Table 6.1 Database from different crystallization conditions and stages	118
Table 6.2 Statistical parameters of ANN-for-size without sampling time for size prediction for both training and testing sets	124
Table 6.3 Statistical parameters of ANN-for-size with sampling time for size prediction for both training and testing sets	124
Table 6.4 Statistical parameters of ANN-for-std without sampling time for STD prediction for both training and testing sets	124
Table 6.5 Statistical parameters of ANN-for-std with sampling time for STD prediction for both training and testing sets.	126
Table 6.6 Number of experimental samples that passed normality (N) or log-normality (LN) test.....	127
Table 6.7 Manually measured and predicted lognormal distribution parameters at each sampling time from the crystallization at changed operation condition.....	127

LIST OF FIGURES

Figure 2.1 Wavelet-FCM methodology for particle image segmentation	27
Figure 2.2 Schematic diagram of the image acquisition setup: (A) Vessel with particle suspension, (B) Circulating pump, (C) Optical flow cell, (D) Camera, (E) Zoom system, (F) Illumination, (G) Computer.....	28
Figure 2.3 (a) Original particle image, (b) First approximation image of (a), (c) Process of wavelet transform on (a) by wavelet function db3 at the first decomposition level (Top left sub-image is approximation coefficients, top right is horizontal detail coefficients, bottom left is vertical detail coefficients and bottom right is diagonal detail coefficients).....	29
Figure 2.4 Thresholded image of Figure 2.3b.....	31
Figure 2.5 (a) High membership of object cluster and (b) High membership of background cluster; (c) Cluster membership value versus pixel intensity	32
Figure 2.6 (a) Values of Fuzzy Range represented as image, (b) Binary version of its complement and (c) Skeleton of Fuzzy Range image	33
Figure 2.7 (a) Separated particle image, (b) Partition results using median filter method	34
Figure 2.8 Particle size distribution of: (a) Manual measurement, (b) Segmentation using thresholded method and (c) Segmentation using Wavelet-FCM approach	36
Figure 2.9 Framework for image-based monitoring and control for particle systems.....	38
Figure 2.10 GUI for Multi-resolution Fuzzy Clustering method.....	39
Figure 3.1 The flow chart of valley detection process.....	47
Figure 3.2 Orientation Vector and Centre of Gravity of a pixel on object boundary	49
Figure 3.3 Flowchart for burrow selection	51
Figure 3.4 Four situations may happen during extension (step size is 3).	52
Figure 3.5 Methodology combining intensity and geometry features for particle image segmentation	53
Figure 3.6 Original image with a horizontal line and particle labels.....	54
Figure 3.7 Intensity variation along the horizontal line.....	54
Figure 3.8 Changes in the mean value of standard deviation as smoothing progress	55

Figure 3.9 Influences of smoothing on the intensity variations along the horizontal line.....	56
Figure 3.10 Smoothed image with $\sigma = 4.2$	56
Figure 3.11 Thresholded image of Figure 3.6 with particle labels	57
Figure 3.12 (a) Valley points and (b) Separation result by subtracting the valley points from the threshold image.	58
Figure 3.13 (a) Selected burrows and (b) Extension of selected burrows. (They were magnified for better visibility).	59
Figure 3.14 Separated image.....	60
Figure 3.15 Watershed algorithm: (a) On gray image (b) On distance transform (c) With markers	62
Figure 3.16 Particle size distribution of: (a) Manual measurement, (b) Segmentation using proposed approach	63
Figure 4.1 Flowchart of automatic texture analysis on crystal images.....	75
Figure 4.2 (a) Pre-processed, (b) Edge detection binary image, (c) Crystal clusters binary image, (d) Crystal clusters image	77
Figure 4.3 $\log_2(\text{detail variance})$ against decomposition level plots with the linear fitted line. The Hurst coefficient can be obtained through the fitted equation.....	79
Figure 4.4 Sample images during crystal growth. a) to i) refers to stage 1 to 9	80
Figure 4.5 The change of mean Hurst exponent (a), mean FD (b), and manually measured mean size (c) during crystallization.	81
Figure 5.1 Overall architecture of mean size prediction.....	85
Figure 5.2 The cumulative percent of explained X- (a) and Y- (b) variance.....	88
Figure 5.3 Manually measured and predicted mean size.....	91
Figure 5.4 Flowchart showing the steps involved in the proposed size monitoring and control technique.....	98
Figure 5.5 (a) Manually measured mean size during crystallization, (b) Fitted CSD for each stage	99

Figure 5.6 Multivariate control chart on the first two principal components. Blue (plus), green (circle) and black (star) represent medium (desired), small and large size respectively	102
Figure 5.7 Multivariate control chart on Q and T2 statistics. Blue plus, green circle and black star represent medium (desired), small and large size respectively. The inset enlarges the bottom left corner of the multivariate control chart for better visibility	103
Figure 5.8 PC1 vs PC2 during growth stages. Stage 1 to 9 is blue (plus), blue (circle), red (circle), green (circle), black (circle), blue (star), red (star), green (star) and black (star) respectively.	104
Figure 5.9 Multivariate control chart Q during growth monitoring test. The signs have the same meaning as in Figure 5.8.....	105
Figure 6.1 A topology structure of three-layer FNN	111
Figure 6.2 Overall architecture of CSD prediction	114
Figure 6.3 (a) Image acquisition setup at LSU, (b) Crystallizer, (c) Thermostatic bath, (d) Peristaltic pump with the antisolvent reservoir, (e) Online sampling device with the optical microscope and the peristaltic pump	116
Figure 6.4 The curves for changed flowrate (a) and temperature (b) versus crystallization time.....	117
Figure 6.5 Manually measured mean size at different crystallization conditions.....	120
Figure 6.6 Estimated FD at different crystallization conditions	121
Figure 6.7 Comparison of manually measured mean size and predicted value for each crystallization run by ANN-for-size without sampling time	123
Figure 6.8 Comparison of expected standard deviation and predicted value for each crystallization run by ANN-for-std without sampling time	125
Figure 6.9 Comparison predicted CSD, raw histogram and the smoothed approximation with the manually measured lognormal distribution parameters at each sampling time from the crystallization at changed operation conditions	129

ABSTRACT

Particulate processes have been widely involved in various industries and most products in the chemical industry today are manufactured as particulates. Previous research and practise illustrate that the final product quality can be influenced by particle properties such as size and shape which are related to operating conditions. Online characterization of these particles is an important step for maintaining desired product quality in particulate processes. Image-based characterization method for the purpose of monitoring and control particulate processes is very promising and attractive.

The development of a digital image-based framework, in the context of this research, can be envisioned in two parts. One is performing image analysis and designing advanced algorithms for segmentation and texture analysis. The other is formulating and implementing modern predictive tools to establish the correlations between the texture features and the particle characteristics.

According to the extent of touching and overlapping between particles in images, two image analysis methods were developed and tested. For slight touching problems, image segmentation algorithms were developed by introducing Wavelet Transform de-noising and Fuzzy C-means Clustering detecting the touching regions, and by adopting the intensity and geometry characteristics of touching areas. Since individual particles can be identified through image segmentation, particle number, particle equivalent diameter, and size distribution were used as the features. For severe touching and overlapping problems, texture analysis was carried out through the estimation of wavelet energy signature and fractal dimension based on wavelet decomposition on the objects.

Predictive models for monitoring and control for particulate processes were formulated and implemented. Building on the feature extraction properties of the wavelet decomposition, a projection technique such as principal component analysis (PCA) was used to detect off-specification conditions which generate particle mean size deviates the target value. Furthermore, linear and nonlinear predictive models based on partial least squares (PLS) and artificial neural networks (ANN) were formulated, implemented and tested on an experimental facility to predict particle characteristics (mean size and standard deviation) from the image texture analysis.

CHAPTER 1. INTRODUCTION

1.1 Problem Statement

Typically, a process is supposed to operate at a given condition according to its design specifications. This operating point is generally the most attractive one, satisfying some performance criteria. If the process deviates from the desired operating point, substantial losses may happen. However, the process behaviour changes with time, consequently monitoring and controlling is essential to meet the standards and requirements of the performance criteria. With the availability of a variety of sensors capable of real-time measurement of various process states, coupled with advances in computer technologies, real-time monitoring systems have become an integral part of the present day industrial processes. Although some sectors of the process industry have taken advantage of the modern tools for process monitoring (petrochemical), other sectors (particle process such as crystallization) are yet to take advantage of these technologies into their operations. Crystallization is a powerful production and separation process. It can mass-produce products with purities that are difficult to achieve using other production processes. Due to this reason, crystallization is the preferred way to manufacture pharmaceuticals and proteins that are subject to United States Food and Drug Administration (FDA) purity regulations. It also is used for the manufacture of agrochemicals and fine chemicals. Any advancement on the on-line optimization and control of crystallization processes will require robust and reliable on-line methods to characterize the product quality (crystal size distribution and shape).

Particle/crystal properties influence final product quality as well as downstream processing requirements and more importantly, depend on operational conditions. In a typical operation the process is subject to disturbances affecting the particle/crystal formation and thus

the final product quality. The operating conditions can be adjusted, if information of the product characteristics is available on-line so that proper control actions/adjustment can be made. Hence characterizing the particle characteristics is very important from the process monitoring and control point of view.

The current challenge in particulate processes which is also preventing of adopting advanced model-based control strategies is the non-availability of on-line sensors. Online characterization of particulate processes for monitoring and feedback control requires direct real-time measurement. This involves defining the measurement technology employed, calculation of various variables and physical attributes of particles, and implementing the characterization in property evaluation or in online process control [1]. Typically, particle size, particle size distribution, and particle shape are critical properties. For a solid material, particles are characterized by both a characteristic size and a representative shape; for a liquid material, particles such as droplets have a spherical shape and their sizes are usually expressed as their diameter [2].

Various measurement technologies exist and many are commercially available for measuring particle size and shape. These commonly include systems based on the technologies of laser diffraction, ultrasound attenuation, and laser reflectance [3-5]. It is safe to say that most of these techniques do not provide an absolute measure of size and shape, but infer the size and shape indirectly based on some secondary variable. However, these devices have further drawbacks such as high costs, unsuitability for in situ or on-line measurements, assumptions of specific shapes of particles, and requirements of particle dispersion prior to size measurement. Naturally a measurement system with acceptable costs and high reliability in an industrial environment would be a preferred choice.

Digital image analysis is a very promising and attractive method for direct measurements, real-time monitoring and control of particle size, size distribution and shape. This is also facilitated by recent progress in high speed imaging devices and equally powerful computers at reasonable costs and the adaptability to real-time application. In addition, digital image analysis can potentially provide absolute size and shape quantification compared with aforementioned measurement techniques. A digital image is defined as a 2D function, $f(x,y)$, where x and y are spatial coordinates, $f(x,y)$ is the amplitude value, and x and y are finite, discrete quantities [6]. Digital images can be obtained by digital cameras such as charge coupled devices (CCDs) which have been used widely at relatively low prices. It is worth to mention that image devices can capture not only the human visible spectra band, but also the full range of the electromagnetic spectrum, ranging from gamma to radio waves. Thus, digital images include both traditional photographic images, ultrasound images, and electron microscopy images, making the application field multi-scaled. Development of an automatic vision-based system which can be integrated to the monitoring and control loop of the process is, however, not without challenge. Direct observation is now considered as the best approach to monitor particle shape and size [7]. Process images can provide more realistic 2D information on particle shape and size and better understanding about the process [8-10].

Because of the advantages and application potential of digital images, they have attracted plenty of researchers' attention, and different image based approaches have been proposed in the last decade for monitoring and control particulate processes. Crystal digital images have many applications, such as: measurement of grain size [11, 12] and crystal morphology [13], growth rates of individual crystal facets [14], monitoring the particle shape [15, 16], and detecting polymorphic transformations [17] during the crystallization process. Larsen et al. proposed an

algorithm of segmentation for High-Aspect-Ration Crystals with images of suspended crystals to monitor crystal size distribution [18]. Khalil used a circular Hough transform to estimate droplet size during an emulsification process to understand the evolution of liquid-liquid dispersion [19]. Automated image analysis had been used as a control tool for multiple emulsions [20]. Image analysis has also been involved in monitoring milling quality of rice in terms of whiteness and percentage of broken kernels in milled rice [21]. Singh and Rao proposed an idea of removing gangue material from the ore of bigger size ranges by image processing and techniques for textural feature extraction from images [22]. Scanning electron microscope (SEM) images of the coating on the surfaces of solar collectors at different deposition times were used to investigate the correlation of optical properties with the microstructure of coatings with the technique of fractal dimension [23]. Multivariate image analysis has been adopted for coating uniformity assessment for coloured immediate release tablets [24].

1.2 Dissertation Motivation

Based on the previous discussion, accurate extraction of size and shape features of particles from images is necessary for reliable particle image analysis and important since whether to change operating conditions or not and the direction of change depend on it. In reality, challenges still exist for image analysis. One of these challenges is that particle images always contain various noises. The susceptibility of images to noise depends on the sensitivity of imaging sensor and transmission methods to external disturbances. Another challenge is the problem of touching and overlapping regions in particle images [25, 26]. Although some kind of particle dispersion method can be used to avoid/reduce this phenomenon, they cannot eliminate touching and overlapping events. Consequently, touching and overlapping areas of particle

images need to be separated or analysed texturally otherwise erroneous size and shape features will be generated.

Given the correct size features, decision making to maintain desired processes are needed. This aim can be realized through building monitoring and control methods that address these challenges and can be used to detect off-specification conditions and/or provide the current values (particle characteristics) of the controlled targets.

1.3 Aims and Contributions of This Dissertation

The aim of this work is to contribute towards the development of an image-based framework, for the purpose of monitoring and control of particulate processes and that accurately will allow extracting size and shaping information for on-line implementation.

Specifically, this dissertation has addressed the following key problems:

- **Image acquisition.** A robust and reliable process imaging setup is one of the key components of an image based monitoring system. Some of the defects that occur during acquisition such as serious blurs are not easily rectified by digital processing of the captured images or lead to high cost in analysis time. Avoidance of such defects is very important towards the overall efficiency of the monitoring system.
 - A laboratory scale software/hardware online and offline framework for capturing particle/crystal images was set up at the LSU Process Systems laboratory. The set-up includes a crystallization reactor fully automated using computer control system for guiding the system along the optimal trajectories
- **Image analysis.** Extracting the accurate relevant information related to the particle properties which are needed to be monitor and control can be realized through image processing. The

steps of image analysis are determined by the challenges of accurately extracting information. The first step is noise removal. This is because images are always degraded because of various noises hidden in both high and low frequencies, and in both space and frequency. Noises can be a disturbance to influence the accuracy of extracted features. Thus it's necessary to deal with them.

- An approach for removal of high frequency noise in particle images was formulated and implemented and an automatic selection of parameters has been proposed.
- Low frequency noise can be handled when necessary.

The second step can be achieved by formulating and implementing two techniques: segmentation and texture analysis. Segmentation, in our approach, involves separating the background and object areas as well as segmenting individual objects in the image. However, texture analysis is appropriate when touching and overlapping problem is severe and regular segmentation methods cannot obtain individual objects.

- Separation methods have been proposed and implemented exploiting the characteristics of the touching and overlapping area in particle images.
- A wavelet multi-resolution approach for texture analysis was formulated and implemented on crystal images obtained to characterize the time evolution of the particle characteristics during a crystallization operation.

The third step is feature representation. Length is a common used to describe size. Others can also available during in image analysis field. The suitability of size representation depends on the technique applied in the previous step.

- Units in pixels and length, area, diameter, size distribution and so on have been used when individual objects/particles can be identified.

- Statistical measurements such as energy and fractal dimension were suitable to characterize if texture analysis was performed.
- **Models for process monitoring and control.** Given the possibility of obtaining feature information from particle images, a key component towards an image-based measurement system is the combination/integration of all the individual components.
 - Principal Component Analysis (PCA), Partial Least Square (PLS) and Artificial Neural Network (ANN) models have been formulated and built towards and on-line automated particle size distribution characterization to be used for online monitoring and control purposes.
 - An integrated framework was formulated and implemented within an experimental facility encompassing image acquisition, processing for feature extraction, and evaluation of system state from trends in the object features.
 - Finally, experimental work was conducted to validate the performance of the proposed approach to characterize the crystal size distribution (CSD) in a crystallization unit. The framework was tested and validated experimentally through investigations in the non-isothermal operation of NaCl-water-ethanol antisolvent crystallization system.

1.4 Structure of This Dissertation

The following paragraphs detail how the dissertation is structured. The first chapter highlights the motivation for the dissertation, generalizes the different contributions in the dissertation, and gives a brief literature background of image-based frameworks for particulate systems.

The second and third chapters focus on image segmentation approaches for particulate systems which involves limited touching and overlapping problems between particles. Chapter 2 presents a novel technique based on combining wavelet transform and Fuzzy C-means Clustering (FCM) for particle image segmentation. Through performing wavelet transform on images, the noise and high frequency components of images can be eliminated and the textures and features can be obtained. FCM is then used to divide data into two clusters to separate touching objects. To quantitatively evaluate this method, a case study involving a particle image is investigated. The procedure of selecting optimum wavelet function and decomposition level for this image is presented. ‘Fuzzy range’ is used as a derived feature for segmentation. The number of particles, particle equivalent diameters, and size distribution before and after partition are discussed. The results show that this method is effective and reliable. An architecture for an image-based feedback monitoring and control framework for particulate processes is proposed.

In Chapter three, an algorithm is proposed to separate the touching and overlapping particles, which is based on the detection of both intensity and geometric features of touching and overlapping regions since they show distinct characteristics in these two profiles. Their intensities have values between objects’ and backgrounds’. The regions where the boundaries of the objects touch or cross show a high level of concavity. Such an approach gives a robust separation method. The performance of the algorithm is compared with that of the watershed segmentation algorithm as well as manual examination of particulate images.

The fourth chapter investigates the use of texture analyses in the form of fractal dimension (FD) and energy signatures as characteristic parameters to track the crystal growth when the touching and overlapping problems become severe. The algorithm uses a combination of thresholding and wavelet-texture analysis. The thresholding method is used to identify crystal

clusters and remove empty backgrounds. Wavelet–fractal and energy signatures are performed afterwards to estimate texture on crystal clusters. A series of images obtained at different crystal growth stages during a NaCl–water–ethanol anti-solvent crystallization system is investigated and their texture characteristics as well as transform tendency during the crystallization process are evaluated.

The fifth chapter, as an extension section of chapter 4, the methodology of establishing PLS model comprising FD and energy signatures to predict the mean size from images is proposed and a PLS model is built with the images taken along the crystallization run in chapter 4. Also PCA models are established for the purpose of mean size characterization / detection. Experimental data from the previous crystallization run are used for illustrating the proposed methodology of designing PCA models.

In chapter six, an image-based multi-resolution sensor for online prediction of crystal size distribution (CSD) is proposed. The mean and standard deviation of lognormal probability density function as the CSD can be predicted through the on-line sensor. In the proposed approach, the texture information extraction strategy is the same to the one as described in chapter 4. Following a nonlinear mapping consisting of an artificial neural network (ANN) is incorporated using as inputs the texture information in conjunction with the available on-line process conditions (flowrate and temperature). The output data for training the ANN models, i.e. the mean and standard deviation of the crystal size distribution, are measured manually at different sampling times as well as in a range of operating conditions. A series of NaCl-water-ethanol anti-solvent crystallization experiments is carried out. A software framework developed in MATLAB enables the configuration of the image acquisition parameters as well as the processing of the on-line images. Validations against experimental data are presented.

Finally chapter seven concludes the dissertation, and provides a list of possible future extensions.

List of publications arising from this thesis:

- **B. Zhang**, A. Abbas, J. A. Romagnoli. (2011). Multi-Resolution Fuzzy Clustering Approach for Image-Based Particle Characterization for Particle Systems Monitoring and Control. *Chemometrics and Intelligent Laboratory Systems*, 107, 155-164.
- **B. Zhang**, A. Abbas, J. A. Romagnoli. (2012) “Monitoring crystal growth based on image texture analysis using wavelet transformation”, *Proceedings ADCHEM International Symposium on Advanced Control of Chemical processes*, July Singapore
- **B. Zhang**, A. Abbas, J. A. Romagnoli. (2013). Automatic image-based estimation of Texture Analysis as a monitoring tool for crystal Growth. *Chemometrics and Intelligent Laboratory Systems*, 121, 42-51.
- **B. Zhang**, R. Willis, J. A. Romagnoli, C.A.M. Fois, S. Tronci, R. Baratti (2013), “Image-Based Multi-Resolution-ANN Approach for On-line Particle Size Characterization”, *Chemical Engineering Transactions*, Vol. 32
- **B. Zhang**, J. Khorat, A. Abbas, J. A. Romagnoli (2013). Separation of Touching and Overlapping Objects in Particulate Images, Submitted to *Chemometrics and Intelligent Laboratory Systems*.
- **B. Zhang**, R. Willis, J. A. Romagnoli, C.A.M. Fois, S. Tronci, R. Baratti (2013). Image-Based Multi-Resolution-ANN Approach for On-line Particle Size Characterization, to be submitted to *Industrial & Engineering Chemistry Research*

1.5 References

- [1] D. M. Scott, Characterizing particle characterization, Particle and Particle Systems Characterization, 20 (2003) 305-310.
- [2] M. A. Larson, A. D. Randolph, Theory of particulate processes, Academic press, INC., 1988.
- [3] H. G. Merkus, Particle size measurements: Fundamentals, Practice, Quality. 2009.
- [4] J. R. Allegra, S. A. Hawley, Attenuation of sound in suspensions and emulsions - theory and experiments, Journal of the Acoustical Society of America, 51 (1972) 1545-1564.

- [5] P. J. Coghill, M. J. Millen, B. D. Sowerby, On-line particle size analysis using ultrasonic velocity spectrometry, *Particle and Particle Systems Characterization*, 14 (1997) 116-121.
- [6] R. E. Wood, R. C. Gonzalez, S. L. Eddins, *Digital Image Processing Using Matlab*, Dorling Kindersley, 2004.
- [7] Y. Zhou, R. Srinivasan, S. Lakshminarayanan, Critical evaluation of image processing approaches for real-time crystal size measurements, *Computers & Chemical Engineering*, 33 (2009) 1022-1035.
- [8] R. F. Li, G. B. Thomson, G. White, X. Z. Wang, J. C. De Anda, K. J. Roberts, Integration of crystal morphology modeling and on-line shape measurement, *Aiche Journal*, 52 (2006) 2297-2305.
- [9] S. M. S. David M. Scott, H. McCann, *Process imaging for automatic control*, Taylor & Francis, Inc., 2005.
- [10] S. E. Umbaugh, *Computer imaging: digital image analysis and processing*, Taylor & Francis, Inc., 2005.
- [11] A. Z. Mhlongo, M. J. Alport, Application of artificial neural network techniques for measuring grain sizes during sugar crystallization, *Proceedings Congress of the South African Sugar Technologists Association*, (2002) 460-468.
- [12] G. A. Argaw, M. J. Alport, S. B. Malinga, Automatic measurement of crystal size distribution using image processing, *Proceedings of the 80th Annual Congress of the South African Sugar Technologists Association*, (2006) 399-411.
- [13] X. Z. Wang, K. J. Roberts, C. Ma, Crystal growth measurement using 2D and 3D imaging and the perspectives for shape control, *Chemical Engineering Science*, 63 (2008) 1173-1184.
- [14] X. Z. Wang, J. C. De Anda, K. J. Roberts, Real-time measurement of the growth rates of individual crystal facets using imaging and image analysis - A feasibility study on needle-shaped crystals of L-glutamic acid, *Chemical Engineering Research & Design*, 85 (2007) 921-927.
- [15] J. C. De Anda, X. Z. Wang, K. J. Roberts, Multi-scale segmentation image analysis for the in-process monitoring of particle shape with batch crystallisers, *Chemical Engineering Science*, 60 (2005) 1053-1065.
- [16] D. B. Patience, J. B. Rawlings, Particle-shape monitoring and control in crystallization processes, *Aiche Journal*, 47 (2001) 2125-2130.
- [17] S. Dharmayat, J. C. De Anda, R. B. Hammond, X. J. Lai, K. J. Roberts, X. Z. Wang, Polymorphic transformation of L-glutamic acid monitored using combined on-line video microscopy and X-ray diffraction, *Journal of Crystal Growth*, 294 (2006) 35-40.

- [18] P. A. Larsen, J. B. Rawlings, N. J. Ferrier, An algorithm for analyzing noisy, in situ images of high-aspect-ratio crystals to monitor particle size distribution, *Chemical Engineering Science*, 61 (2006) 5236-5248.
- [19] A. Khalil, F. Puel, Y. Chevalier, J. M. Galvan, A. Rivoire, J. P. Klein, Study of droplet size distribution during an emulsification process using in situ video probe coupled with an automatic image analysis, *Chemical Engineering Journal*, 165 (2010) 946-957.
- [20] I. Scherze, R. Knofel, G. Muschiolik, Automated image analysis as a control tool for multiple emulsions, *Food Hydrocolloids*, 19 (2005) 617-624.
- [21] B. K. Yadav, V. K. Jindal, Monitoring milling quality of rice by image analysis, *Computers and Electronics in Agriculture*, 33 (2001) 19-33.
- [22] V. Singh, S. M. Rao, Application of image processing and radial basis neural network techniques for ore sorting and ore classification, *Minerals Engineering*, 18 (2005) 1412-1420.
- [23] E. Barrera, F. Gonzalez, E. Rodriguez, J. Alvarez-Ramirez, Correlation of optical properties with the fractal microstructure of black molybdenum coatings, *Applied Surface Science*, 256 (2010) 1756-1763.
- [24] S. Garcia-Munoz, D. S. Gierer, Coating uniformity assessment for colored immediate release tablets using multivariate image analysis, *International Journal of Pharmaceutics*, 395 (2010) 104-113.
- [25] P. A. Larsen, J. B. Rawlings, Assessing the reliability of particle number density measurements obtained by image analysis. *Particle and Particle Systems Characterization*, 25 (2009) 420-433.
- [26] D. M. Scott, Characterizing particle characterization. *Particle and Particle Systems Characterization*, 20 (2003) 305-310.

CHAPTER 2. MULTI-RESOLUTION FUZZY CLUSTERING APPROACH FOR IMAGE-BASED PARTICLE CHARACTERIZATION FOR PARTICLE SYSTEMS MONITORING AND CONTROL*

2.1. Introduction

Accurate extraction of size and shape features of particles from images is necessary for reliable particle image analysis. In reality, particle images always contain touching and overlapping regions. Physical particle dispersion is used to avoid this phenomenon prior to capturing the images. This can reduce but cannot eliminate touching and overlapping events because of the fact that dispersed particles will flow together or ecliptically. Touching and overlapping areas of particle images need to be separated otherwise erroneous size and shape features will be generated. Image segmentation refers to the techniques used in image processing for separating touching and overlapping areas in images and is the concern of this chapter with a focus on particle image segmentation.

Image segmentation is one of the most crucial and challenging tasks in image analysis. It is widely used in object detection [1, 2]. Since most image processing procedures are executed after the separation step, the eventual success or failure of image analysis largely relies on segmentation accuracy. The goal of segmentation is to divide the digital image into different visually distinct regions or objects. Image segmentation can be formally defined [3] as follows: supposing F represents all the pixels of an image, partition of the set F into n regions can be:

$$F = \bigcup_{i=1}^n S_i, \text{ For all the regions}$$
$$S_i \cap S_j = \emptyset, i \neq j \quad (2.1)$$

where S_i and S_j are the i -th and j -th region respectively, \emptyset is the empty set. For each region, all the pixels possess similar characteristics or properties; while different regions, even adjacent

*Portions reprinted from *Chemometrics and Intelligent Laboratory System*, Copyright 2011

ones are non-homogeneous. The criterion P to decide which region a pixel belongs to can be intensity, texture, color and any other measurable features. Segmentation should satisfy the following two conditions:

$$\begin{aligned} P(S_i) &= true \\ P(S_i \cup S_j) &= false, i \neq j \end{aligned} \quad (2.2)$$

Many segmentation techniques have been reported and developed. Fu and Mui [4] reviewed segmentation techniques and categorized proposed techniques in the area of biomedical image segmentation into three classes: characteristic feature thresholding or clustering, edge detection and region extraction. Pal and Pal [5] summarised segmentation techniques in the situations of gray tone images, color images and images with high noisy environments. Cufi et al. [6] defined and classified segmentation techniques based on integrating boundary and region approaches. Image segmentation has to address the challenge that no specific approach can be suitably applied to all the kinds of images. For example, a segmentation technique used in images for remote control applications may not be suitable for medical images. The separation efficiency of applied segmentation technique largely depends on how much accurate information can be abstracted from images. Since images come from different application fields and environments have their own manners of noise presentation and information storage, a segmentation technique may only perform successfully or efficiently on images that have the similar characteristics.

In this chapter, a novel approach is proposed for particle image segmentation based on combining wavelet transform (Multi-Resolution) and Fuzzy C-means Clustering (FCM) for image segmentation. Wavelet transform has been widely used for multi-resolution analysis in the last two decades. Basically it is used for 1D signal (time series) processing. An image can be taken as

a 2D signal where the temporal is replaced by spatial information. Wavelet transform makes it possible to investigate a signal (image) in both time (space) and frequency domain at the same time [7-9]. In our research, wavelet transform is used to identify the image surface self without noise and high frequency components. Pattern recognition analysis, in terms of FCM is then incorporated for clustering analysis of the image at the surface self. With FCM method, we differentiated objects and background, identified the objects and boundaries and separated the touching areas. A new derived feature called ‘fuzzy range’ is incorporated to extract the touching area for segmentation. No neighborhood based calculation is needed when using fuzzy range other than traditional features like standard deviation. The proposed approach not only efficiently separates touching and overlapping areas in particle images, but also makes on-line monitoring and controlling of particle systems based on image analysis a feasible technique.

This chapter is organized as follows. The methodology of Multi-resolution Fuzzy Clustering is introduced in detail in Section 2.2 and 2.3. In Section 2.4, we demonstrate our methodology. In Section 2.5, a case study involving a particle image sample is carried out to illustrate the methodology. An architecture for a monitoring system for particle size and size distribution is proposed in Section 2.6. Finally, conclusions are presented in the last section.

2. 2 Image Analysis by Wavelet Transform

Any image can be considered as a combination of the image self and imaging artifacts (noise). Three main components are very often isolated for an image self, namely the roughness, the waviness and the form which can be considered as a multi-resolution signal combination. Once an image is taken, it is difficult to distinguish the contribution of each resolution by ordinary analysis methods, which focus on either spatial distribution at one resolution or frequency distribution only. Both image spatial and frequency information are important to de-

correlate the contribution of different process steps. A recent Multi-Resolution technique, wavelet decomposition, can successfully separate the image underlying structure, in the form of the low frequency sub-image, image details, in the form of high frequency sub-images, as well as the imaging noise. High-frequency details and the imaging artifacts are difficult to differentiate, since they all fall into the high frequency range. The most convenient way to calculate different image characterizing features are also obtained from wavelet coefficients.

Particle images are either intensity of pixels or height of the surface in a 2D array. A wavelet decomposition is to be done for this 2D array of data. Since the data are discrete, a 2D discrete wavelet transformation is to be performed. This is discussed next.

2.2.1. Discrete Wavelet Transformation

In a discrete wavelet transformation, discrete value of scale a and location parameter b are used. They are discretized in such a manner that a and b are linked. The scale a is generally discretized in a logarithmic way a_0^m where m is an integer. Each location b can be reached in discrete steps n (an integer) from an origin. It is also proportional to the scale a_0^m . Thus it can be represented as $nb_0a_0^m$. The wavelet function $\psi_{m,n}$ in the discrete form is

$$\psi_{m,n}(x) = \frac{1}{\sqrt{a_0^m}} \psi(a_0^{-m}x - nb_0) \quad (2.3)$$

where a_0 is a fixed dilation parameter and is greater than 1 and b_0 is the location parameter and is greater than zero. The discrete wavelet transformation of function $f(x)$ is thus a function of m and n instead of a and b respectively:

$$T_{m,n} = \int_{-\infty}^{+\infty} f(x) \psi_{m,n}(x) dx \quad (2.4)$$

Discrete wavelet transformation $T_{m,n}$ is known as wavelet coefficient or detail coefficient. The most common way of discretization is to use a dyadic grid where a_0 and b_0 are 2 and 1 respectively. Discrete dyadic wavelets are orthonormal in nature. The original function can be reconstructed using the wavelet coefficients:

$$f(x) = \sum_{m=-\infty}^{+\infty} \sum_{n=-\infty}^{+\infty} T_{m,n} \psi_{m,n}(x) \quad (2.5)$$

2.2.2 Multi-resolution Analysis and Discrete Function

Like wavelet functions, there is another set of functions called scaling function $\phi_{m,n}(x)$. The scaling function when convoluted with the function $f(x)$ gives approximation coefficient [10]:

$$S_{m,n} = \int_{-\infty}^{+\infty} f(x) \phi_{m,n}(x) dx \quad (2.6)$$

The scaling function is orthogonal to translation (n) but not to dilation (m). So, an approximation of the function (x), which is also considered as low frequency information, at scale index m can be obtained as

$$f_m(x) = \sum_{n=-\infty}^{+\infty} S_{m,n} \phi_{m,n}(x) \quad (2.7)$$

Using the approximation coefficient and detail coefficient we can get the function $f(x)$ - as a sum of approximation of the function at arbitrary scale index m_0 and detail function from scale m_0 to $-\infty$:

$$f(x) = \sum_{n=-\infty}^{+\infty} S_{m_0,n} \phi_{m_0,n}(x) + \sum_{m=-\infty}^{m_0} \sum_{n=-\infty}^{+\infty} T_{m,n} \psi_{m,n}(x) \quad (2.8)$$

The detail function or high frequency information at scale index m can be written as

$$d_m(x) = \sum_{n=-\infty}^{+\infty} T_{m,n} \psi_{m,n}(x) \quad (2.9)$$

Thus we can write the function $f(x)$ using Equations (2.8) and (2.9) as

$$f(x) = f_{m_0}(x) + \sum_{m=-\infty}^{m_0} d_m(x) \quad (2.10)$$

where when m is low the resolution is high and vice versa.

If the original function is discrete then it is seen as an approximation at scale index $m=0$. If the function $f_0(x)$ is of finite length N and the scale index varies from $0 < m < M$, then it is a dyadic grid $N = 2^M$. Since N is the length through which the wavelet function can be translated (b), when the scale index is m we have $b = n2^m = N = 2^M$ or $n = 2^{M-m}$. Thus n ranges between $0 < n < 2^{M-m} - 1$ for each m . In that case, by Equation (2.8) the function $f_0(x)$ can be written as

$$f_0(x) = S_{M,n} \phi_{M,n}(x) + \sum_{m=1}^M \sum_{n=0}^{2^{M-m}-1} T_{m,n} \psi_{m,n}(x) \quad (2.11)$$

By Equations (2.7) and (2.9) it can also be written as

$$f_0(x) = f_M(t) + \sum_{m=1}^M d_m(x) \quad (2.12)$$

2.2.3 2D Discrete Wavelet Transformation

In the application of the image, the data set is a 2D array of pixels. To perform 2D wavelet composition on the image, 2D discrete wavelet transformation must be applied. In

moving from 1D to 2D wavelet transformation, the rows and columns of the data matrix (x and y coordinates) that represent the image are treated as independent. Therefore, the 2D filters become the tensor products of their 1D counterpart. The scaling and wavelet functions for a 2D transform are obtained from tensor product of the one dimensional scaling and wavelet functions.

$$\begin{aligned}\phi(x_1, x_2) &= \phi(x_1)\phi(x_2) \\ \psi^v(x_1, x_2) &= \psi(x_1)\phi(x_2) \\ \psi^h(x_1, x_2) &= \phi(x_1)\psi(x_2) \\ \psi^d(x_1, x_2) &= \psi(x_1)\psi(x_2)\end{aligned}\tag{2.13}$$

where ϕ is the scaling function and ψ^v , ψ^h and ψ^d are the vertical, horizontal and diagonal wavelet respectively. The corresponding approximation coefficients are $S_{m,n}$ and detail coefficients are $T_{m,n}^v$, $T_{m,n}^h$ and $T_{m,n}^d$ respectively. Modifying Equation (2.8), the image $f(x)$ is:

$$f(x) = \sum_{n=-\infty}^{+\infty} S_{m_0,n} \phi_{m_0,n}(x) + \sum_{m=-\infty}^{m_0} \sum_{n=-\infty}^{+\infty} T_{m,n} \psi_{m,n}(x)\tag{2.14}$$

At level one, the image data is visually decomposed into four sub-images, representing the smoothed approximation, the horizontal detail, the vertical detail and the diagonal detail. This performance can be iterated on the smoothed approximation sub-image.

2.2.4 Image Multi-resolution Denoising

An image is always affected by noise. The main source of noise contained in images is the presence of various types of optical, electrical and thermal interference during the process of image acquisition and associated steps. The susceptibility of acquired images to noise largely depends on the sensitivity of image sensors and transmission methods to external disturbances. Images suffering from noise are in a degraded state. Before proceeding with image segmentation,

removing noise in images or restoring the degraded images into its original upgraded state is carried out. In general, spatial (linear and nonlinear) [11] and frequency (Fourier transform) [12] filters are the widely adopted method for noise removal. However, those filters can only process images on either spatial or frequency domains. For example, when Fourier transform makes transformation on the frequency domain, the spatial information is lost in this process. Wavelet transform on the other hand makes it possible to investigate an image in both space and frequency domain at the same time. It can distinguish meaningful variability of the pixel light intensity in an image from random fluctuations and discard noise.

The Multi-resolution approach deals with denoising problems through decomposing images with wavelet transform and examining the detail coefficients at different decomposition levels. Upgraded images are achieved by subtracting the unwanted part of the noise from detail coefficients. As mentioned before, a given image can be modelled by Equation (2.8). While its corresponding upgraded image has models of the form:

$$f(x) = \sum_{n=-\infty}^{+\infty} S_{m_0,n} \phi_{m_0,n}(x) + \sum_{m=-\infty}^{m_0} \sum_{n=-\infty}^{+\infty} T_{m,n}^{denoised} \psi_{m,n}(x)$$

$$T_{m,n}^{denoised} = \begin{cases} 0 & m \geq M_1 \\ T_{m,n} & m < M_1 \end{cases} \quad (2.15)$$

where M_1 is the decomposition level selected for the image denoising problem. Detail coefficients generated before level M_1 are removed as noise.

2.2.5 The Choice of Wavelet Function and Wavelet Decomposition Level

Since there are several wavelet functions available, the selection of optimal wavelet function, for the particular application, is the first problem to be tackled when applying the transform on an image. Wavelet functions are catalogued into various wavelet families and the

most common ones are: Haar, Daubechies, Biorthogonal, Coiflets, Symelets. For some wavelet families, such as Daubechies, their member numbers are not constrained to only one. Different wavelet functions will generate different transforms, central frequencies and vanishing moments. By performing the transform using a wavelet function on a specific image, the decomposed sub-images will present the features in terms of frequency and spatial localization in response to the characteristics of the wavelet function. However, that wavelet function may or may not be able to capture the actual information from the image. Also an optimal function selected for one image may not be the best for another situation. The accuracy of image analysis results therefore depends on the selection of wavelet function.

Another issue that needs to be addressed is level of decomposition where we get the surface self without image artifacts. Theoretically, for an image whose pixel number is m in both directions, n decomposition levels can be performed if n satisfies the condition of $2^n \leq m < 2^{n+1}$. As the image is decomposed to a certain level, the intrinsic information is totally smoothed out. However, the artifacts of the wavelet function will be added to the corresponding approximation if the decomposition process continues. In order to maintain the true characteristics and also remove irrelevant noise and high frequency components of the image at the same time, it is necessary to find a suitable decomposition level.

Entropy measures can be employed to help identify the appropriate wavelet function and decomposition level which would yield an approximate sub-image with maximum information with respect to the key features for proper image segmentation. Among different entropy criteria, Shannon Entropy is applied. The concept of Shannon Entropy is sometimes referred to as a measure of uncertainty and is defined for a discrete probability distribution p_i :

$$S(p) = - \sum_{i=1}^n p_i \log(p_i)$$

$$\text{where } \sum_{i=1}^n p_i = 1 \quad (2.16)$$

n is the total number of possible classes. The probability distribution is obtained from the normalized wavelet coefficient energies:

$$\bar{T}_{m,n}^2 = \frac{T_{m,n}^2}{\sum_{m=1}^M \sum_{n=1}^N T_{m,n}^2} \quad (2.17)$$

The idea of Shannon Entropy as the criteria to identify the ‘best’ decomposition level is based on the measurement of the randomness for a given image. The more random parts existing, the more Shannon Entropy value the approximation image has. By performing the wavelet analysis on an image using a particular wavelet function, the Shannon Entropy will decrease at first due to the removal of noises and high frequency components. However, as the procedure goes on, it will increase after a certain level because of the added artifacts from the wavelet. So the decomposition level at which the first minimum Shannon Entropy value is present or the critical point changing the trend of Shannon Entropy can be considered as the optimum level.

The selection of wavelet basis functions by Shannon Entropy depends on the amount and distribution of information it captures from the original image. The entropy values obtained at optimal decomposition levels will not be the same for different wavelet functions, which means that their information contents will also be different. Among different wavelet functions, higher entropy value can be explained as more underlying information are recovered and contained in the approximation image. The maximum entropy value will probably appear when the information is evenly spread whereas the minimum entropy occurs when all the information

squashes in a single location. Thus, we look for the wavelet function which provides the maximum Shannon Entropy value at its optimal decomposition level.

2.3 Clustering Pixel Intensity Values

Clustering analysis is a statistical method of partitioning a set of observations into several subsets which can be called clusters [13]. The components in the same subset have a similar property to some extent [14]. This feature in one subset is different from those in the other clusters so that clusters can be distinguished. The way to determine the similarity among components is based on a distance measure. A common used distance function for clustering analysis is the Euclidean distance. Clustering methods can be classified into three categories: hierarchical clustering, partitional clustering and spectral clustering. Fuzzy C-means Clustering belongs to the category of partitional clustering.

2.3.1 Fuzzy C-Mean Clustering

Fuzzy C-means Clustering assigns each observation partly into a cluster [15]. Since data points can always be considered in one cluster and also in another one in practical situations, the concept of fuzzy theory is applied in clustering method. Rather than belonging completely to one cluster, every observation has a degree of becoming a member of that cluster. In this way, all partitions are connected to each other. Thus FCM has special advantages over conventional clustering methods. For all the c clusters, the sum of the degree or the membership of each point should be 1.

$$\begin{aligned}
\sum_{i=1}^c u_{ik} &= 1, \text{ for all the } c \text{ clusters} \\
0 &\leq u_{ik} \leq 1 \\
0 &< \sum_{k=1}^n u_{ik} < n
\end{aligned} \tag{2.18}$$

where u_{ik} is interpreted as the degree of point k in the i -th cluster. The total number of input points and clusters are n and c respectively. u_{ik} satisfies the condition that its value is between 0 and 1. When u_{ik} equals 1, it means point i belongs to the i -th cluster completely; otherwise it is not the member of the i -th cluster at all if the value of u_{ik} is 0.

The degree u_{ik} itself can be calculated as the inverse of the distance measure between the point x_k and its corresponding cluster centre. The normalized and fuzzyfied form is used more widely. Introducing the weighting exponent m

$$u_{ik} = \frac{1}{\sum_j^c \left(\frac{d_{ik}}{d_{jk}} \right)^{2/(m-1)}}$$

where $d_{ik} = |x_k - v_i|$; $d_{jk} = |x_k - v_j|$ (2.19)

The cluster centre v_i is nothing but the average of all the observations in i -th cluster:

$$v_i = \frac{\sum_{k=1}^n u_{ik}^m x_k}{\sum_{k=1}^n u_{ik}^m} \tag{2.20}$$

Similarly, v_j denotes the mean in j -th cluster. To divide observations into desired c clusters, FCM algorithm minimizes an objective function consisting of summation of weighted membership and squared error of the distance to the cluster centre through an iterative process.

$$J_{FCM} = \sum_{k=1}^n \sum_{i=1}^c u_{ik}^m d_{ik}^2 \tag{2.21}$$

The FCM algorithm can be performed in the following steps:

- a. Decide the number of clusters c according to the requirement and set a sensitivity threshold ε (a small positive constant).
- b. Initially guess all the cluster centers and distribute every point the degree belonging to each cluster.
- c. Iteratively update the cluster centers with Equation (2.20) and the degrees of all the points with Equation (2.19) until the difference of the objective function (Equation (2.21)) between two consecutive iterations is less than ε .

2.3.2 Fuzzy Range Clustering

Fuzzy Range Clustering (FRC) was originally proposed by Khorat [1] and is embedded into the multi-resolution approach described before. FRC mainly investigates the differences in membership values of clusters generated from pixel intensities through FCM. Supposing only two clusters (one for objects and one for background) are created and Mo_i and Mb_i are the membership values for point i in one fuzzy cluster and the other respectively. The fuzzy range for both clusters (R_i) is formulated as:

$$R_i = Mo_i - Mb_i, \text{ for all the point } i \quad (2.22)$$

R_i is a new and typical feature of touching areas besides traditional features such as gradient, standard deviation, etc.. From the standpoint of fuzzy clustering theory, the pixel intensities of touching areas have a similar degree of belonging to both clusters. It may be noted that the advantage of FRC over traditional features is that only the pixel intensities of interest is involved and is independent of the size of the neighborhood [13].

2.4 Methodology for Particle Image Segmentation

The essential and sequence of steps for implementing the proposed methodology for particle image segmentation are given in Figure 2.1. An input image is treated as a 2D array of pixel intensities by several wavelet functions at multiple decomposition levels and approximation images are then generated. Shannon entropy is calculated for each approximation image. The optimal decomposition level by one wavelet function is achieved through finding the first minimum entropy. The most suitable wavelet function is selected by comparing the entropy values at their optimal decomposition level among all the wavelet functions and identifying the maximum one. The approximation image which is transformed by the most suitable wavelet function at the optimal decomposition level is processed in two segmentation ways, thresholding method and fuzzy clustering method. A base separated image in a binary format is formed (thresholded image) by thresholding method and is prepared to be used as a basis. Performing fuzzy cluster method obtains membership values of objects and background clusters. The touching areas in particle images are recognized by fuzzy range method because their membership values for belonging to objects or background are similar. The final segmentation image is obtained by subtracting touching regions from thresholded image.

2.5 Case Study

Detecting and extracting accurate information from on-line or off-line process is the key step for any control and monitoring system. Usually, particle size and size distribution are parameters measured from particle image. However, particle images always contain touching and overlapping regions, making segmentation important and a necessary step. In this case study, the proposed separation technique combining wavelet transform and FCM algorithm is applied to

particle image analysis to identify and separate objects and the result are compared with conventional segmentation approaches.

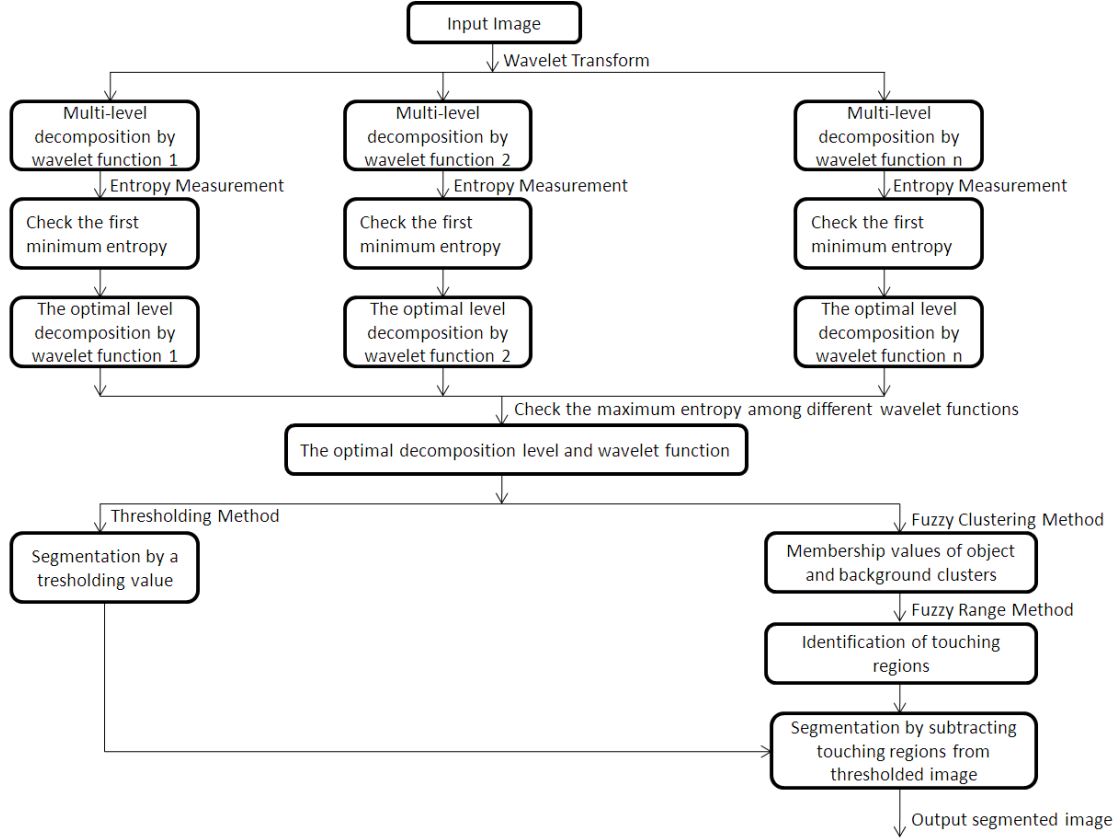


Figure 2.1: Wavelet-FCM methodology for particle image segmentation.

2.5.1 Imaging Setup Used in the Present Study

A laboratory scale software/hardware framework for capturing particle images for this case study was originally setup at the University of Sydney [16] and the images utilized are from that work. The experimental setting includes a system with a flow cell and pump, through which particles are continuously circulated, an illumination system for lighting up the imaged region of the flow cell, an optical zoom system for providing magnification and a digital video camera for continuous image capture. Figure 2.2 illustrates the schematic diagram of the experimental set up. The camera used is a CMOS chip based video camera (BASLER make, model A620f) with a

resolution of 1024 X 1280 pixels and is connected to the computer using a IEEE 1394 cable. The particles were circulated with water using a pump (Watson Marlow UK). An optical zoom system (Thales Optem zoom125C) with maximum magnification of 150X was fitted to the camera lens. A software framework developed in MATLAB enables the configuration of image acquisition parameters. The particles used are Poly Vinyl Chloride (PVC) particles of refractive index of about 1.5.

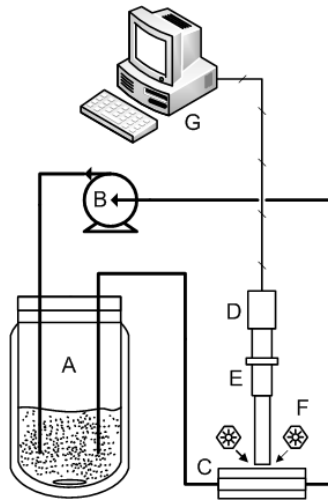


Figure 2.2: Schematic diagram of the image acquisition setup: (A) Vessel with particle suspension, (B) Circulating pump, (C) Optical flow cell, (D) Camera, (E) Zoom system, (F) Illumination, (G) Computer (Khorat, 2008)

2.5.2 Application

The original grey particle image in a JPG format was imported into MATLAB for processing. To simplify the calculation, it was cropped into an image possessing 1024x1024 pixels shown in Figure 2.3a. Visual observation reveals a total of 15 particles in this image, all of which are sequentially labelled from 1 to 15. Manual partition and measurements were determined in the software of ImageJ (V1.42q, NIH, USA). In previous work, a nonlinear filter namely order statistics filters was chosen to process the image [1]. In the current work wavelet

transform will be used to improve image quality by decomposing an image into four sub-images, since noise and high frequency parts contained in an image exist in frequency and spatial domain.

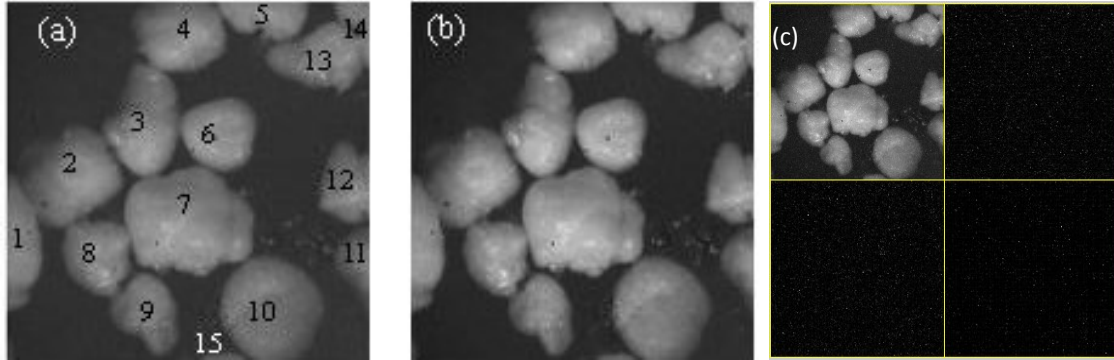


Figure 2.3: (a) Original particle image, (b) First approximation image of (a), (c) Process of wavelet transform on (a) by wavelet function db3 at the first decomposition level (Top left sub-image is approximation coefficients, top right is horizontal detail coefficients, bottom left is vertical detail coefficients and bottom right is diagonal detail coefficients).

To obtain the optimal solution, four common wavelet families and six decomposition levels for each wavelet function were considered. The entropy values of the approximation images are listed in Table 2.1. In each data column, the first minimum number was highlighted in bold. Some of them reached the minimum at the first decomposition level. Implementation of the wavelet transform only once by wavelet functions such as db3, coif1, and coif3 would be enough to remove noise and high frequency components and obtain smooth surfaces of the particles. On the other hand, for wavelet functions Haar, db6, sym4, and sym8, their spatial and frequency characteristics cannot remove surface noise in the first approximation so that more decomposition steps are needed to reach the lowest entropy value. Once this first minimum entropy is reached, on further decomposition, the artifacts from the wavelet function will be added to the particle surface which will make the surface irregular and correspondingly increase the Shannon Entropy. The decrease of entropy value after this increase in further decomposition

level is due to the relative smooth surface shaped as a result of the removal of irregular parts. Taking this into consideration, the second or the third minimum point is meaningless since plenty of real information has been eliminated. By comparing those minimum values among different wavelet functions, the greatest was found to be 2.2661. This indicates that db3 can retain more information than the other wavelet functions. It can be said that a smoothed image containing maximum meaningful information can be obtained through performing wavelet transform on Figure 2.3a by wavelet function of db3 at the first decomposition level.

The process of wavelet decomposition on Figure 2.3a is presented in Figure 2.3c. Four sub-images are produced. The approximation sub-image (top left) are the low frequency components and retained to obtain the improved image, while the other three detail sub-images are the high frequency components and considered as noise to remove. Figure 2.3b shows the improved image through inverse wavelet transform only on approximation coefficients.

Table 2.1: Shannon Entropy (1.000e+004) for different wavelet functions and decomposition levels. The minimum values are highlighted in bold.

	Haar	db3	db6	sym4	sym8	coif1	coif3
1 st	1.9968	2.2661	2.2644	2.348	2.1095	2.1579	2.0987
2 nd	1.9696	2.2736	2.2558	1.9792	2.0698	2.2484	2.2659
3 rd	1.944	2.2401	2.1278	2.3523	2.065	1.9628	1.9866
4 th	1.9176	2.2152	2.0458	2.4132	2.2069	2.2373	2.2663
5 th	1.9171	2.2372	2.0195	2.4357	2.2773	2.3616	2.2801
6 th	1.9865	2.4014	2.0196	2.3321	2.1604	2.3121	2.1435

The improved image was then simply divided into objects and backgrounds by thresholding which is a segmentation method based on a threshold value. The Otsu's method of selecting a threshold from grey level histograms was chosen in this work. Objects were formed where the pixel intensities are greater than the threshold value and the background is assigned where they are less than the threshold value. The binary image with labels on each particle

shown in Figure 2.4 shapes the objects whose values are 1 and the rest are the background with the value of 0. Some particles are connected to each other in the binary image. They were considered as a single object resulting in wrong particle sizing. The number of particles and particle size calculated from this binary image is used as a comparison to the partition result from the FCM approach.

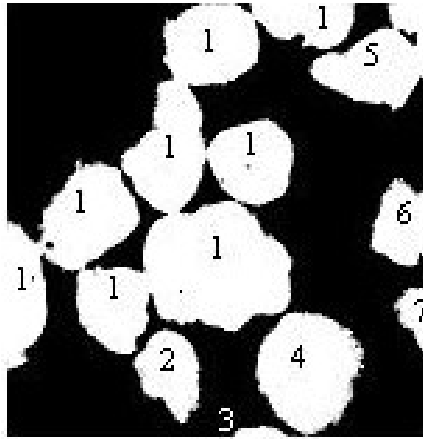


Figure 2.4: Thresholded image of Figure 2.3b.

When partitioning the first approximation image into two clusters, representing the objects and the background, two membership images are generated as shown in Figures 2.5a and 2.5b. Figure 2.5c describes the membership value versus pixel intensity. The weighting exponent m , the maximum number of iterations and objective error as the FCM parameters used in this paper are 2, 500 and 10^{-5} respectively. The influence of iterations number has been investigated as well and it is found that the same result can be obtained if the iterations number is chosen between 500 and 1000.

On closer examination of the membership values of the boundary including touching regions in both membership images, it can be observed that they are similar. This may be due to the fact that their pixel intensity values are between those in the two clusters. The boundary

region image was obtained by subtracting the two membership images using FRC. The subtraction result was represented as an image like Figure 2.6a for better visualization [1]. The boundary regions have low values close to zero while objects and background parts show values close to 1 as expected. The boundary regions were highlighted with value of zero through transferring the subtraction results into a binarized version with the threshold method previously described. A binary complement was generated, with the result of boundary regions showing value of 1 like Figure 2.6b. However, the boundary lines were rather wide which could lead to severe area losses after removal of boundary lines from the above mentioned thresholded image. To minimize this problem, morphological thinning operation was performed producing a skeleton of the boundary regions. The thin boundary regions are shown in Figure 2.6c.

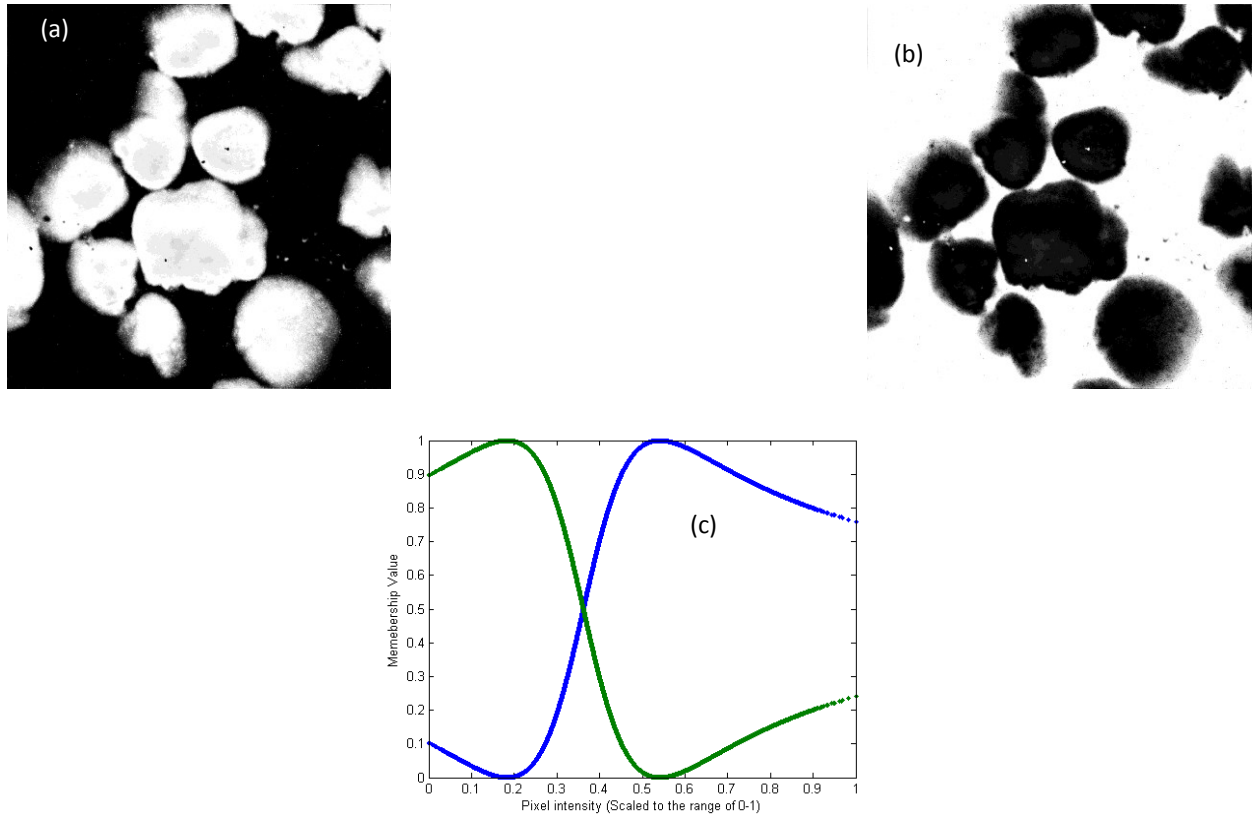


Figure 2.5: (a) High membership of object cluster and (b) High membership of background cluster; (c) Cluster membership value versus pixel intensity.

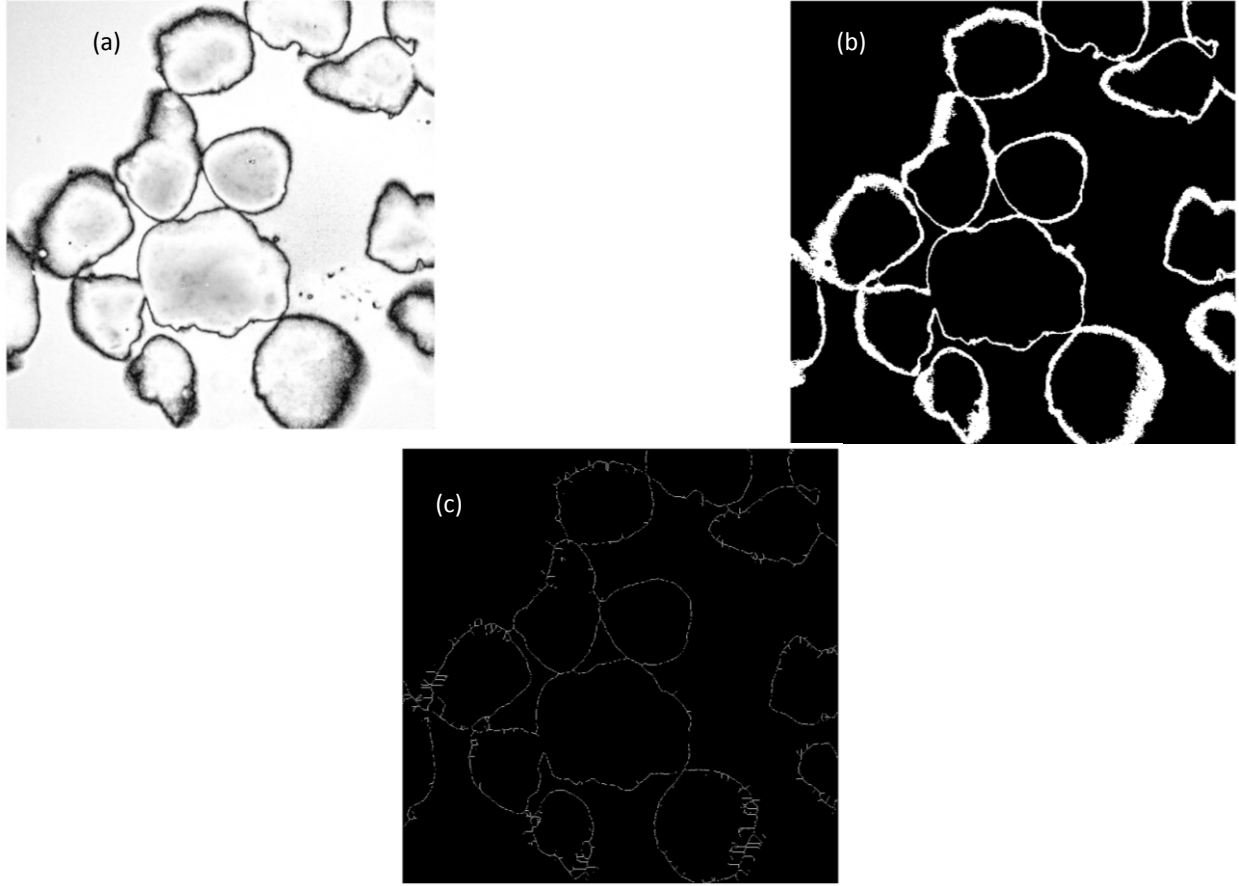


Figure 2.6: (a) Values of Fuzzy Range represented as image, (b) Binary version of its complement and (c) Skeleton of Fuzzy Range image.

To achieve the separation, the thin boundary including touching regions were removed from the thresholded image. After performing proper morphological operations deleting holes and spurs, the final results shown in Figure 2.7a were obtained. The labels of separated particles are printed on the image. Figure 2.7b shows the separated particle image using median filter [1].

2.5.3 Equivalent Diameter and PSD

The particle number, particle equivalent diameter, and particle size distribution (PSD) are considered to illustrate the separation efficiency. The comparison involves Figure 2.3a (the manual processed image), Figure 2.4 (thresholded image) and Figure 2.7a (resulting from

Wavelet-FCM approach). The comparison of the Wavelet-FCM method with the median filter approach with respect to segmentation level (Figure 2.7b) is also discussed as well. The thresholded image (Figure 2.4) results in 7 particles and the separated image (Figure 2.7a) results in 13 particles. The extra number was coming from separation of the touched objects which were considered as one single connected particle. However, the approximation image was not over partitioned since there are actually 15 particles by visual examination (Figure 2.3a). Although some particles are successfully separated, particle 4, 5, and 11 remain connected in Figure 2.7a.

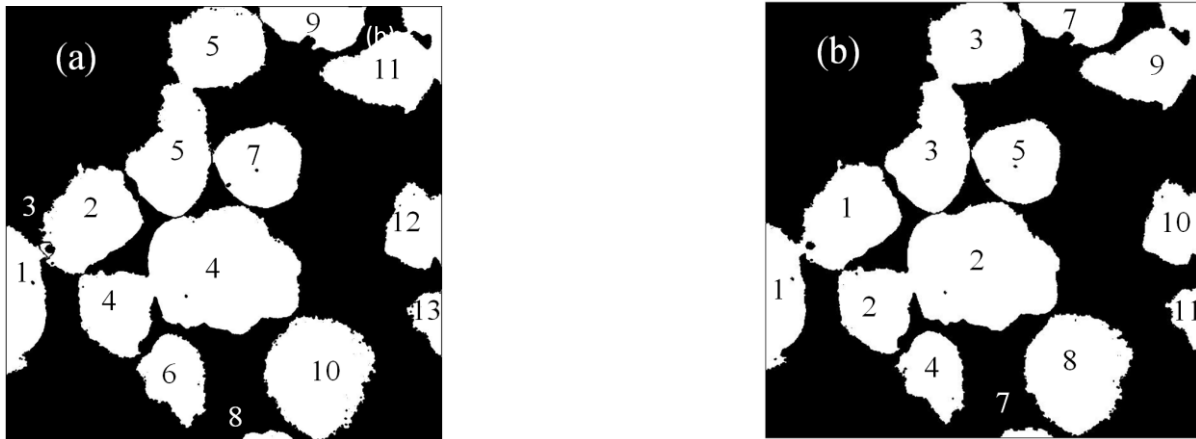


Figure 2.7: (a) Separated particle image, (b) Partition results using median filter method.

The equivalent diameter, defined as the diameter of a circle that has the same area of that object, is used to describe the size of the particles. It is counted as the number of pixels. Their values in the manual processed image, thresholded image and separated one using Wavelet-FCM approach, are listed in Table 2.2. Particles in Figure 2.3a were identified manually as circles or ellipses. The same particle was chosen from the above mentioned three images to compare their sizes. For example, particle 9 in the original image, particle 2 in thresholded image and particle 6 in separated image, are selected. The diameter found in the separated image is smaller compared with that from the thresholded image while both are greater than manual measurements. The

differences between thresholded image and separated image are generated due to the algorithms' differences in identification of the particles' boundary region. The particles shrink after segmentation because of the deletion of missing parts in edges considered as components of touching regions. The differences with manual measurements are caused by non-accuracy of modelling particles with ellipses. The shapes of some particles are irregular so that considering them as circles or ellipses in the manual measurement will lead to area loss or addition.

Table 2.2: Particle equivalent diameter

Particle label	Manual processed image	Thresholded image	Wavelet-FCM approach processed image
1	126.6	630.3	176.3
2	175.9	171.4	227.9
3	169.0	55.8	21.79
4	153.9	262.0	375.5
5	106.6	230.0	310.9
6	139.9	164.4	169.4
7	216.7	99.3	53.3
8	135.0	--	199.0
9	131.7	--	156.1
10	196.4	--	260.4
11	85.9	--	224.8
12	120.9	--	161.7
13	134.1	--	95.7
14	82.9	--	--
15	41.8	--	--

PSD provides direct information of the distribution of the equivalent diameters in a certain range and their normalized frequencies. The histogram of equivalent diameters and their fitting curves through Weibull density probability function are used to describe the PSD. PSD of the manual processed image, thresholded image and separated image are shown in Figure 2.8a, Figure 2.8b and Figure 2.8c respectively. PSD obtained by manual processing (Figure 2.8a)

illustrates that a large proportion of particles actually have equivalent diameters in the range of 50 to 250. This proportion and equivalent diameter range are considered as a reference for PSD generated via threshold method and the Wavelet-FCM approach. Comparing them (Figures 2.8b and 2.8c), we can find that the latter has high frequency of appearance of the particles with similar size and less dispersion of the large diameter values and conclude that by separating the touched objects, the mean size decreases and the size distribution reduces in broadness. Segmentation by Wavelet-FCM approach brings the PSD closer to the reference than by threshold method.

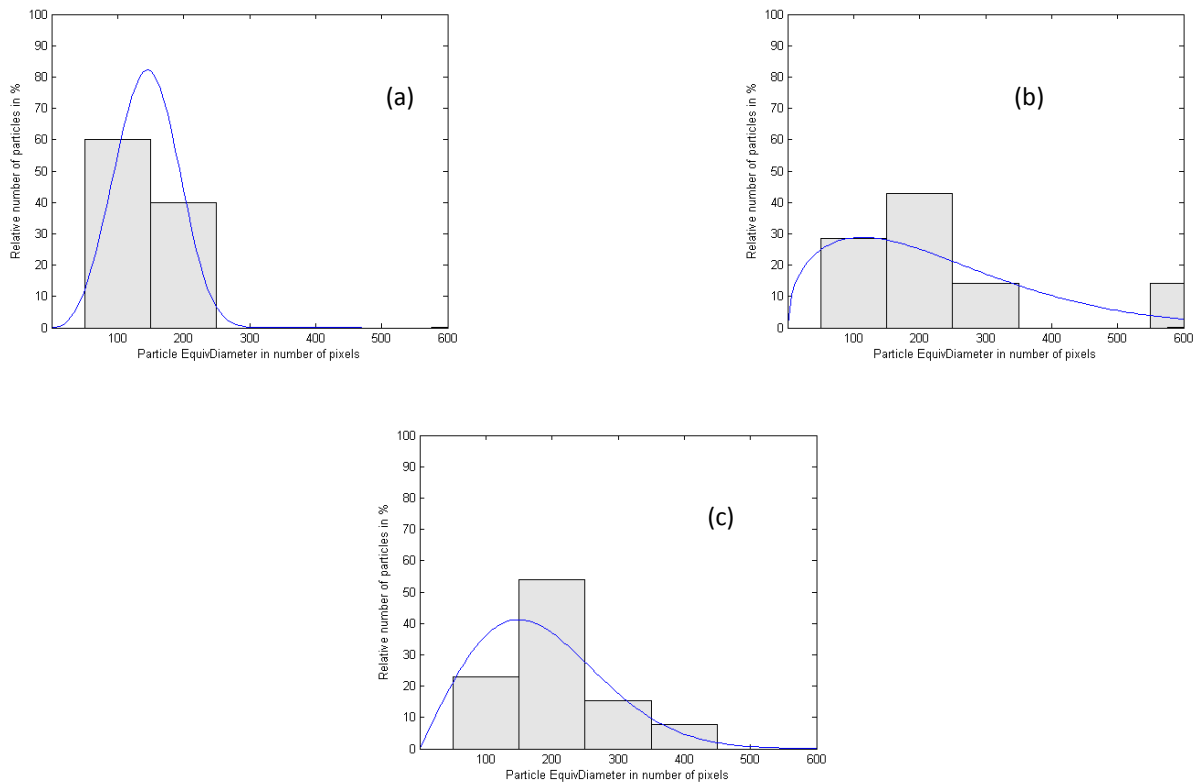


Figure 2.8: Particle size distribution of: (a) Manual measurement, (b) Segmentation using thresholded method and (c) Segmentation using Wavelet-FCM approach.

It is also interesting to compare the partition results using the wavelet transform method instead of the median filter method as reported in [1]. The partition results using median filter method can be seen in Figure 2.7b. Particle 1 in Figure 2.7b cannot be separated by median filtering technique but it was successfully separated in Figure 2.7a. The noise in the original image has not been removed completely by the median filter and the remaining noise was considered as misleading information for the FCM analysis. Wavelet transform can eliminate enough noise and capture meaningful information. From this point of view, the introduction of the wavelet transform improves the segmentation of particle images

2.6 Architecture of the Image-Based Controlling and Monitoring Framework

Following the successful separation of touching and overlapping areas in particle images using Wavelet-FCM, we propose the use of this approach for real-time image-based size measurement for particle process monitoring and control applications. Although the measurement is estimated from 2D images, statistically meaningful results are attainable via analysis of sufficient numbers of images. The basic architecture of a framework for particle size control that utilises this technique is presented in Figure 2.9. The monitoring system is shown inside the dotted rectangle in Figure 2.9. This architecture comprises a feedback control loop, with intensities of images as the measurement inputs, particle size and PSD as the measurement output (or the controlled variable), process operational parameters as the manipulated variable, and target particle size and PSD as the set point. During online analysis, the measured value of the output is compared with the set point value. The difference (tracking error) between the output value and the set point value is fed through the controller. If the output value largely deviate from the set point value, a control action for modifying process parameters is generated.

The most important feature of this feedback control system is that it learns the process behaviour through this new image-based measurement as the feedback signal to the controller that commands a certain change in the manipulated variable to maintain target process conditions.

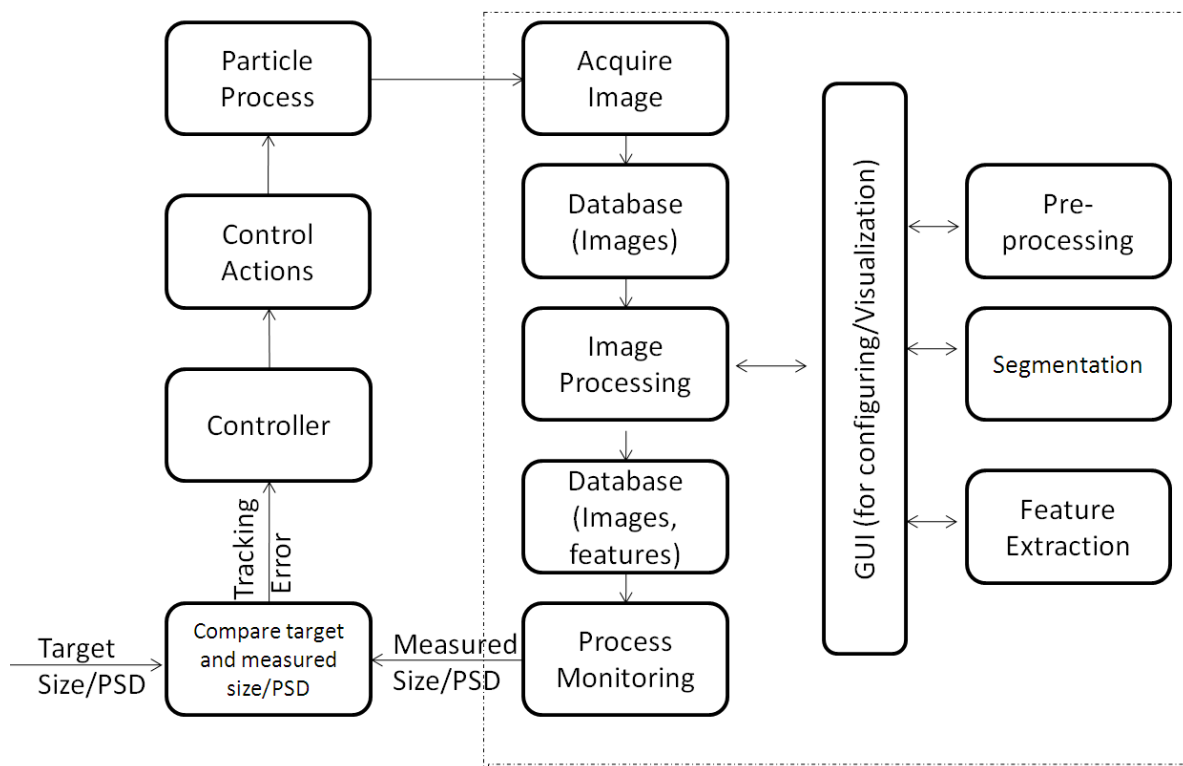


Figure 2.9: Framework for image-based monitoring and control for particle systems.

For reliable performance, a monitoring system must include components of acquisition, storage and processing of the data as well as display and storage of the information content of the data. The hardware, software and associated communication interfaces have to suitably constitute to satisfy the requirements in terms of speed, scale and interoperability with other systems in an industrial environment. In the case of image-based monitoring, the acquired images form the primary input data and they are stored in a database. Information of this data is

to be extracted and made available in a form required by the process monitoring methodologies. The input data repository should be available for different schemes of information extraction and have to reach to the performance requirements with respect to storage and retrieval. The data base of information extracted from images, such as features of objects, also has to meet similar criteria of storage and accessibility by multiple methodologies. The image processing algorithms constitute the main software module of the proposed system. The procedures of processing images include pre-processing, segmentation and feature extraction. The pre-processing methods have to be chosen depending on the kind of degradation the images in a particular system and environment are exhibiting.

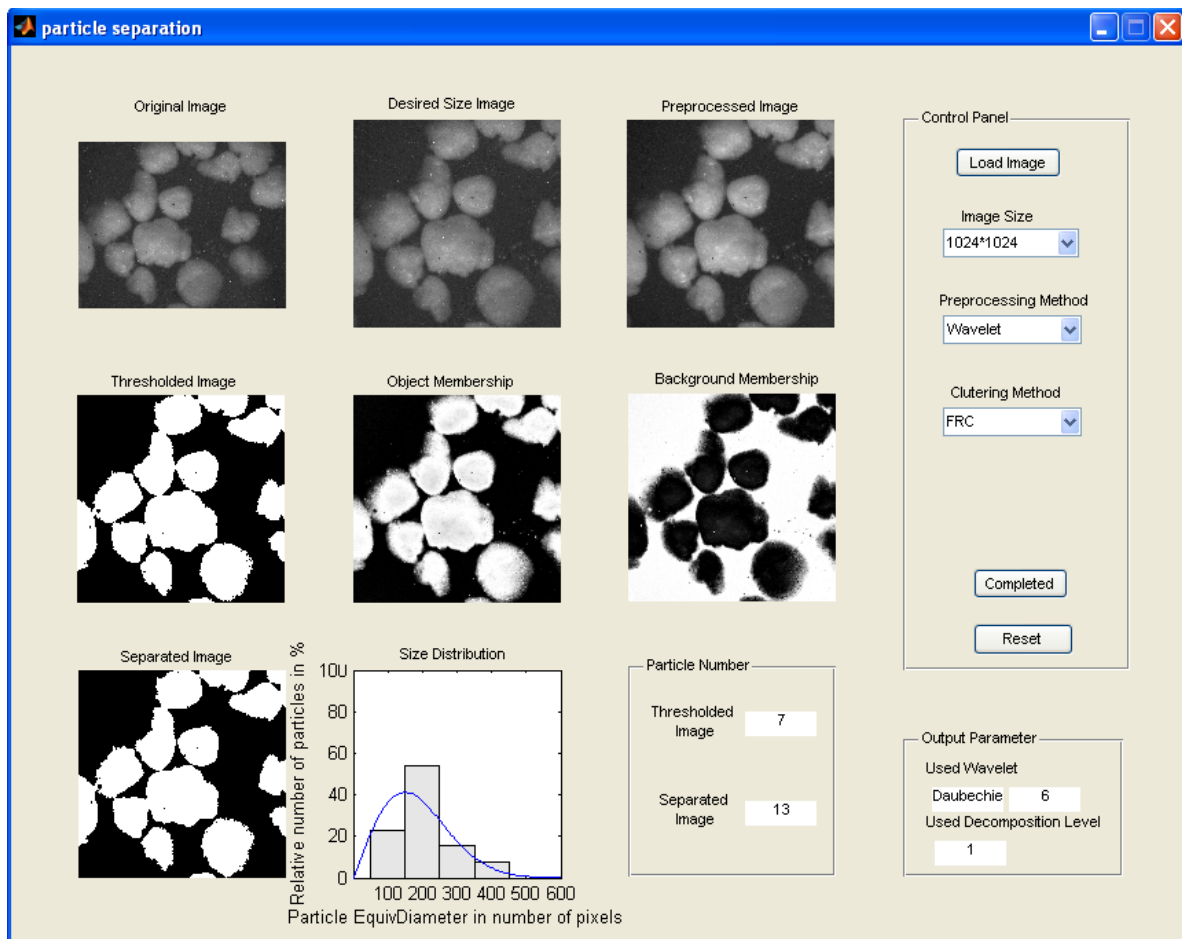


Figure 2.10: GUI for Multi-resolution Fuzzy Clustering method.

The procedures of processing images can be visualised and executed through a Graphical User Interface (GUI). GUI provides the human interaction with the system for visualization, conducting manual analysis and system configuration/management. A sample GUI for the current study is presented in Figure 2.10. The interface includes configuring the image acquisition setup, selecting the pre-processing and segmentation methods, viewing the images when they are analyzed, visualization of feature data in charts or trends curves, and displaying the comparison between before and after segmentation. The image size, de-noising methods of wavelet transform and median filter, clustering basis of fuzzy range and traditional features can be selected through the GUI. Also, the processed image for each stage, size distribution graph, the particle numbers of thresholded image and separated image, and the adopted wavelet function and decomposition level are shown.

2.7 Conclusions

An image segmentation approach combining wavelet transform and FCM was proposed and applied in the case study of particle image segmentation. This method could successfully identify 13 out of a total of 15 objects and it was found to be superior to previous approaches. The image was not over partitioned and the particle equivalent diameters and size distribution in the separated image were more meaningful. These results attest the potential of an image-based particle process monitoring and control system. A feed-back control architecture with the proposed measurement methodology has been conceptualised for real-time application.

2.8 References

- [1] J. M. Korath, A. Abbas, J. A. Romagnoli, A clustering approach for the separation of touching edges in particle images, *Particle and Particle Systems Characterization*, 25 (2008) 142-153.

- [2] W. Sun, R. Mukherjee, P. Stroeve, A. Palazoglu, J. A. Romagnoli, A multi-resolution approach for line-edge roughness detection, *Microelectronic Engineering*, 86 (2009) 340-351.
- [3] S. L. Horowitz, T. Pavlidis, Picture segmentation by a directed split-and-merge procedure, in: *Proceedings of 2nd International Joint Conference on Pattern Recognition*, (1974) 424-433.
- [4] K. S. Fu, J. K. Mui, A survey on image segmentation, *Pattern Recognition*, 13 (1981) 3-16.
- [5] N. R. Pal, S. K. Pal, A review on image segmentation techniques, *Pattern Recognition*, 26 (1993) 1277-1294.
- [6] X. Cufi, X. Munoz, J. Freixenet, J. Marti, A review of image segmentation techniques integrating region and boundary information, *Advances in Imaging and Electron Physics*, 120 (2002) 1-39.
- [7] I. Scherze, R. Knofel, G. Muschiolik, Automated image analysis as a control tool for multiple emulsions, *Food Hydrocolloids*, 19 (2005) 617-624.
- [8] W. Sun, J. A. Romagnoli, J. W. Tringe, S. E. Letant, P. Stroeve, A. Palazoglu, Line edge detection and characterization in SEM images using wavelets, *IEEE Transactions on Semiconductor Manufacturing*, 22 (2009) 180-187.
- [9] J. Malek, A. Sebri, S. Mabrouk, K. Torki, R. Tourki, Automated breast cancer diagnosis based on GVF-snake segmentation, wavelet features extraction and fuzzy classification, *Journal of Signal Processing Systems for Signal Image and Video Technology*, 55 (2009) 49-66.
- [10] P. S. Addison, *The illustrated wavelet tranform handbook*, Institute of Physics Publishing Bristol and Philadelphia, Napier University, Edinbrugh, UK, 2002.
- [11] A. K. Jain, *Fundamentals of digital image processing*, Prentice-Hall, Inc., New Jersey, 1989.
- [12] R. Bracewell, *The Fourier transform and its applications*, McGraw-Hill Science/Engineering/Math; 3 edition, New York, 1999.
- [13] Y. Yang, Image segmentation based on fuzzy clustering with neighborhood information, *Optica Applicata*, 39 (2009) 135-147.
- [14] C. T. Sun, J. S. R. Jang, E. Mizutani, *Neuro-Fuzzy and soft computing*, Prentice Hall Inc. , New Jersey, 1997.
- [15] J. C. Bezdek, *Pattern recognition with fuzzy objective function algorithms*, Plenum Press, New York, 1981.
- [16] J. M. Korath, *Image-based Monitoring of Particulate Processes*, PhD thesis, The University of Sydney, 2008.

CHAPTER 3. SEPARATION OF TOUCHING AND OVERLAPPING OBJECTS IN PARTICULATE IMAGES BY COMBINING INTENSITY AND GEOMETRY CHARACTERISTICS

3.1 Introduction

The promising perspective usage of images for process monitoring and control has been described in previous chapter. Also the issue of touching and overlapping objects in particulate images and its negative effect on image were highlighted. Multi-Resolution Fuzzy Clustering Approach to identify touching and overlapping regions was presented in the Chapter 2 as well. The motivation for the clustering methodologies was based on the fact that pixel intensity of the touching and overlapping regions is distinctly different from that of other regions in the image. The touching areas show a similar fuzzy degree of belongs to either backgrounds or objects. The approach based on the derived feature ‘fuzzy range’ presented in Chapter 2 shows an effective method to identify the touching regions. However, although Multi-Resolution Fuzzy Clustering Approach is very effective in identifying touching regions, it is not successful in identifying the overlapping regions.

Recently, an approach for the separation of touching and overlapping objects in particulate images by combining intensity and geometric features was proposed by Korath [1] and will be used in our approach. The methodology focuses on separating touching and overlapping objects in particulate images by making use of both intensity information and geometric features of touching and overlapping regions since these areas have distinct characteristics on intensity and geometric profiles. Their intensities are relatively low compared to these of objects’ bodies, but many not to be low enough to be considered as the backgrounds [2]. Pixels from these regions show a higher level of concavity than those from the boundary of other regions [3, 4]. The segmentation algorithm starts at detection of valley points whose intensity values are between those of objects’ bodies and backgrounds, followed by linking

discontinuity valley segments. Geometric features of the boundaries are used as a criterion to screen detected valley segments. The final segmentation is then achieved through the extension of these segmentation candidates.

The chapter is structured as follows. Pre-processing, where the image is processed to remove noise and other kinds of degradations, is given in Section 3.2. Segmentation including thresholding which is basically a classification process where objects of interest are separated from the background, detecting valleys which is based on investigating on intensity profiles and final separation by combining geometric features, is discussed in Section 3.3. A conceptual framework on this methodology and a case study are provided in Section 3.4 and 3.5 respectively. Comparisons of segmentation results to watershed and manual analysis are carried out in Section 3.6 before concluding in Section 3.7.

3.2 Image Pre-Processing

Almost all acquired images from image acquisition processes suffer from noises due to external disturbances such as electrical, thermal and optical variations. Noise removal is an indispensable preprocessing step in image processing to obtain accurate information and is done by filtering the image in either spatial or frequency domain with corresponding noise removal filters. Noise removal filters can be broadly categorized as linear and nonlinear filters [5]. In linear filtering, a pixel value is replaced by a linear combination of the pixel values in a small neighborhood around that particular pixel. These filters are smoothing filters that smooth out the effects of noise. However, smoothing can cause blurring of the images to some extent. In nonlinear filtering, the result depends on the relative value of the processed pixel to its neighbors. As the type of noise varies from system to system, it is necessary to choose the right kind of filter

depending on the specific system under consideration. In this methodology, linear spatial filter is used to remove the noise from images under the consideration of capturing intensity features of touching and overlapping regions in the next processing step.

The linear filtering operation requires a filter with a neighborhood size of $M \times N$. For each pixel (x, y) , its corresponding response of the filter by linear filtering operation is the sum of products of the filter and its neighborhood pixels. The important issue which arises while attempting image smoothing through linear spatial filtering without losing features of interest is about the extent of smoothing. Smoothing the image with Gaussian kernel is the most preferred method to solve this problem [6]. The two dimensional Gaussian function is given by:

$$g(x, y; \sigma) = \frac{1}{2\pi\sigma} \exp\left(-\frac{(x^2 + y^2)}{2\sigma^2}\right) \quad (3.1)$$

where σ^2 is the variance parameter which determines the spread of the Gaussian kernel. The filtering operation for the image $f(x, y)$ using the above kernel is given by the equation:

$$F(x, y; \sigma) = f(x, y) * g(x, y; \sigma) = \int_{\mu=-\infty}^{\infty} \int_{\varepsilon=-\infty}^{\infty} g(x, y; \sigma) f(x - \varepsilon, y - \mu) d\varepsilon d\mu \quad (3.2)$$

where F is the smoothed image and ‘*’ denotes filtering. For digital image which can be treated as a discrete function, working with an odd size filter, this equation needs appropriate summing notations:

$$F(x, y; \sigma) = \sum_{m=-\frac{M-1}{2}}^{\frac{M-1}{2}} \sum_{n=-\frac{N-1}{2}}^{\frac{N-1}{2}} g(x, y; \sigma) f(x - m, y - n), M, N \text{ are odd integers} \quad (3.3)$$

The above process approaches unsmoothed image for small values of the parameter σ of the Gaussian kernel and higher approximations of the image as σ increases. Selecting an optimum value of σ is very critical for obtaining meaningful results from the smoothed image. The criterion adopted to arrive at optimal smoothing is the rapid random variations in the pixel

values which can be quantified by a measure of disorder like standard deviation or entropy. As the image becomes smoother this measure of disorder will become lesser.

3.3 Segmentation

3.3.1 Thresholding

Thresholding is a segmentation approach operating in a way of comparing objects' intensity values with a certain threshold value. If only one feature is of interest in an image, separating the image into two classes, a foreground and a background, by applying a single threshold value is sufficient during the thresholding process. The foreground is those pixels with higher intensity values than the threshold value and the upper boundary for thresholding implementation is the highest pixel value in the image; otherwise it is the background. This process can be described as the following equation:

$$\begin{aligned} G_1 &= \{f(x, y) > T\} \\ G_2 &= \{f(x, y) \leq T\} \end{aligned} \tag{3.4}$$

where G_1 and G_2 represent object and background respectively. T is the threshold value. $f(x, y)$ is the value of the pixel located in the x^{th} row and y^{th} column.

In a thresholding algorithm, the threshold value is the significant parameter for successfully dividing segments, thus appropriately selecting the threshold value becomes the major concern. Otsu's global thresholding is a method for finding the optimum threshold value among the candidates under the circumstance of identification of only two classes in an image [7]. The algorithm is performed by comparing the variance within class as the summation of weighted variance in each class (Equation (3.5)) with the variance between classes shown in

Equation (3.6). The optimum value is the one which can generate the lowest within class variance and highest between classes variance.

$$\sigma_W^2(t) = w_b(t)\sigma_b^2(t) + w_f(t)\sigma_f^2(t) \quad (3.5)$$

where w and σ^2 are the weight and variance. The subscripts W, b, f mean within class, background and foreground. t represents a threshold value.

$$\sigma_B^2(t) = \sigma^2(t) - \sigma_W^2(t) \quad (3.6)$$

The subscript B means between classes.

3.3.2 Separate through Intensity Features

3.3.2.1 Intensity Features of Touching and Overlapping Regions

The touching and overlapping regions show distinct characteristics in intensity profile. They exhibit valleys where intensity rises on either side with a minimum in between. These valleys are different from the object/background boundaries which are more of step changes. The slopes of these valleys vary widely depending on the orientation and relative size of the particles involved. Some are very rapidly changing while others are relatively slow. Nevertheless, there always exists a valley along the regions of touch and overlap. It is this peculiar feature of intensity variation to identify the regions of touch and overlap in particle images.

3.3.2.2 Algorithm for Detecting Valleys

According to the characteristics of valleys, a method which can detect presence of the minima based on its depth and over an extended neighborhood would be able to capture the valley points effectively. A strategy to trap the valley points is proposed and plotted in Figure 3.1. In this process, firstly, the two parameters needed to be fixed are the minimum depth a valley

and the size of the search window. The factors influencing these parameters are the extent of intensity valley in the touch and overlap regions and the size of objects respectively. Suitable values for these two parameters can be decided for a class of images by manual examination of a few images from the class. Next, a convolution of scanning image at horizontal, vertical and diagonal directions is involved. They can be defined as an Ones vector of $1 \times n$, an Ones vector of $n \times 1$, a unit matrix and its mirror matrix respectively, where n is the size of the search window. In each loop, the image is processed with appropriate ranking filters to obtain local extreme in the search window and points satisfying criteria of minimum depth and equaling the minimum value in the neighborhood are stored as a binary image.

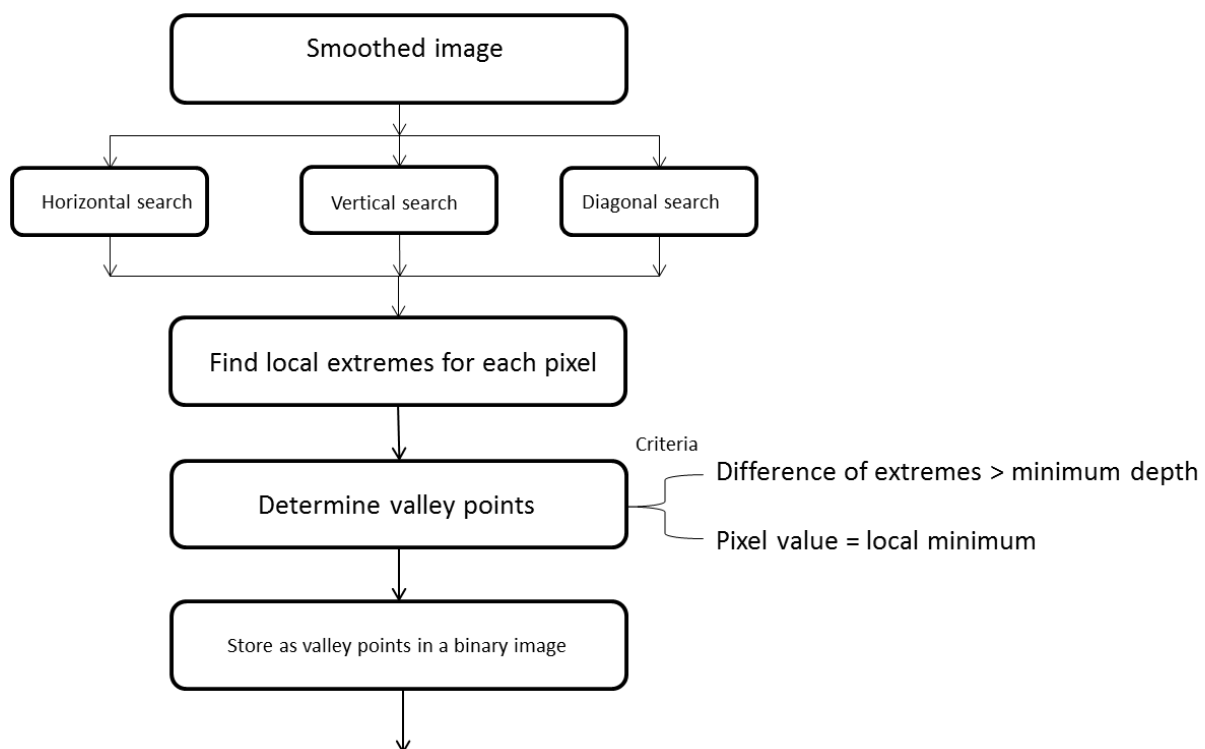


Figure 3.1. The flow chart of valley detection process

The detected valley points can form into three classes. One is dividers which can completely divide the joint object along the touch or overlapping regions. The others can be categorized as burrows which start from the object boundary and proceed deeper inside the object and inner dips which lie along a possible touching or overlapping region but isolate inside the object. The burrows contain the information helpful in segmentation but need further processing to realize the goal of complete separation. The inner dips are segment but separated from burrows because of disturbances or non-removed noises. Both burrows and inner dips are real regions of touching and overlapping in ideal situation. To form more dividers, it is necessary to extend burrows or to link burrows with inner dips. However, some of the detected burrows and inner dips are disturbances due to the complex of real life. In this scenario, selection of burrows becomes necessary. Geometric features of boundary curves can help to select burrows. Disturbances of inner dips can be dealt by morphological operations after new dividers being formed.

3.3.3 Separate Combining Geometric Features

Touching and overlapping regions do have distinct characteristics on intensity profile, such as relative low intensities than object itself. However, points which satisfy this condition may not all belong to touching and overlapping regions. A typical reason can be the roughness of object surface. A method to solve the problem of distinguishing real touching/overlapping regions and disturbances resorts to geometric profile.

3.3.3.1 Geometric Features of Touching and Overlapping Regions

The touching and overlapping regions also show different features in geometric profile of their boundaries. Whenever objects touch or overlap, the regions where the boundaries of the

objects touch has a high level of concavity. Moreover, the wedges formed on both sides of a touch/overlap are oriented in opposite directions. Such sharp magnitude and orientation of the concavity of boundary curves can be quantitatively captured by the concept of center of gravity (COG) and local eccentricity [3]. For a particular pixel on the boundary, the coordinates of COG are calculated by the following formulas:

$$X_{cog} = \frac{1}{N} \sum_{i=1}^N x_i$$

$$Y_{cog} = \frac{1}{N} \sum_{i=1}^N y_i \quad (3.7)$$

where x_i and y_i are relative coordinates of the N neighboring points (also lying on the boundary) with respect to the particular boundary pixel i . Then the eccentricity is calculated as:

$$\varepsilon = \sqrt{X_{cog}^2 + Y_{cog}^2} \quad (3.8)$$

The orientation vector of COG relative to the pixel under consideration is represented by its coordinates (X_{cog}, Y_{cog}) . Figure 3.2 depicts the concept of COG and its orientation.

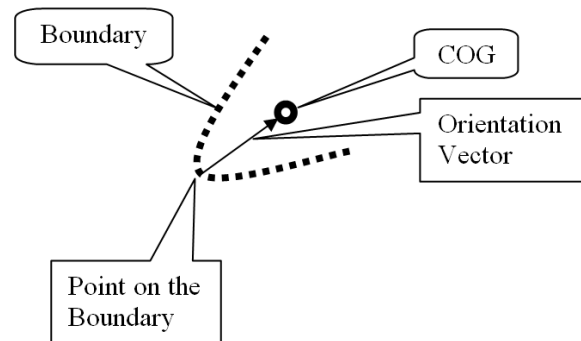


Figure 3.2. Orientation Vector and Centre of Gravity of a pixel on object boundary (Korath, 2008)

Eccentricity is the distance from the point on the boundary to its COG or in other words, the length of the orientation vector as shown in Figure 3.2. The higher the value of the eccentricity, the stronger the indentation on the boundary curve is. The eccentricity of the touching and overlapping regions will have a very high value compared with that from other regions in the boundary. Locations on the boundary where their eccentricities are above a certain value are selected as possible regions of crossing between boundaries of touching/overlapping objects.

3.3.3.2 Algorithm for Segmentation Combining Geometric Features

A brief outline for the selection of burrows is given in Figure 3.3. It begins by finding the boundary of the binary image obtained from previous valley detection operation which contains dividers, burrows and inner dips. To utilize geometry information, the eccentricity of every point on the boundary is calculated. A threshold value indicating high concavity will be chosen to determine potential touching/overlapping points on the boundary. Any burrows starting from these regions are considered as the real burrows and stored for the process of extension. The tips of burrows which are located on the boundary are called as base tips. The others inside the objects are front tips.

The extension of burrows starts from front tips. A step of front tip selection is needed when a burrow has more than one front tip. The front tip which has the farthest Euclidean distance from the base tip will be chosen. Each of the selected front tips is extended along the direction from its corresponding base tip to the front tip in a step by step process. During each extension step, four situations may happen to burrows. Figure 3.4 illustrates them from Figure 3.4a to 3.4d respectively, with an extension step size of 3. First, extended burrows may do not

cross any inner dips or burrows or boundaries. Then they will go to the next extension step. Second, they may cross with boundaries, in this case extended burrows will be reduced to the cross point and the extension stops. Third, crossing of another burrow in the extension process leads to formation of a divider. Fourth, they may get connected with inner dips. Then the burrows can be automatically extended up to the tip of the inner dips. The redundant parts of extended burrows, which cross over the intersection point, will be deleted. The selection of the tip of the inner dips depends on the direction between the intersection point and tips. The favorable tips will be the ones which deviate least from the burrow direction. Further extension starts from the new front tip points. In this way, burrows and inner dips can become dividers.

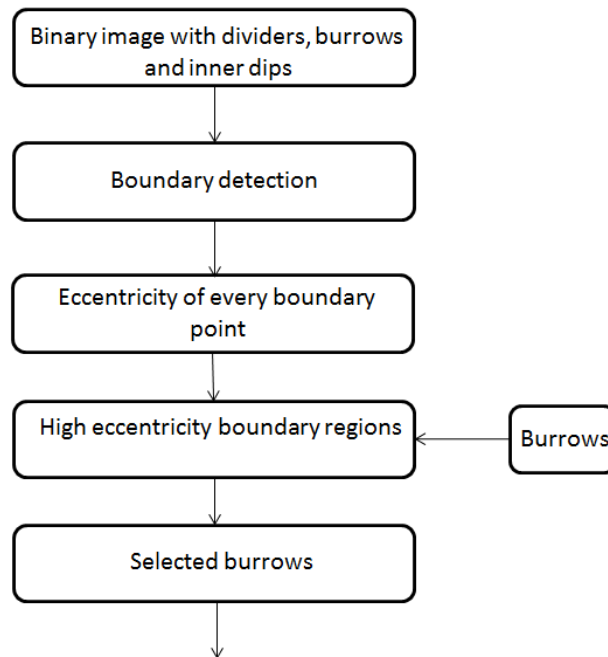


Figure 3.3. Flowchart for burrow selection

3.4 Methodology

The essential sequence of steps for implementing the proposed methodology for particle image segmentation are given in Figure 3.5. An input image is treated as a 2D array of pixel

intensities and Gaussian lowpass filter is applied to remove noises but remain intensity and geometry features of touching and overlapping regions. The smoothed image is processed in two segmentation ways, thresholding and the approach combining intensity and geometry features. A base separated image in a binary format is formed (thresholded image) by thresholding method. Valley points as the intensity feature of touching and overlapping regions, which have relative low intensity compared with object bodies but not low enough to be calculated as the backgrounds, are detected. The valley points are named into dividers, burrows and inner dips according to their locations on object bodies. They then are subtracted from thresholded image, generating a binary image containing dividers, burrows and inner dips. Burrows which locate on the boundary of the binary image with high eccentricity are chosen to extend. The extension operation can form more dividers and they are combined with dividers obtained by intensity feature detection to be subtracted from the thresholded image to get the final segmentation image.

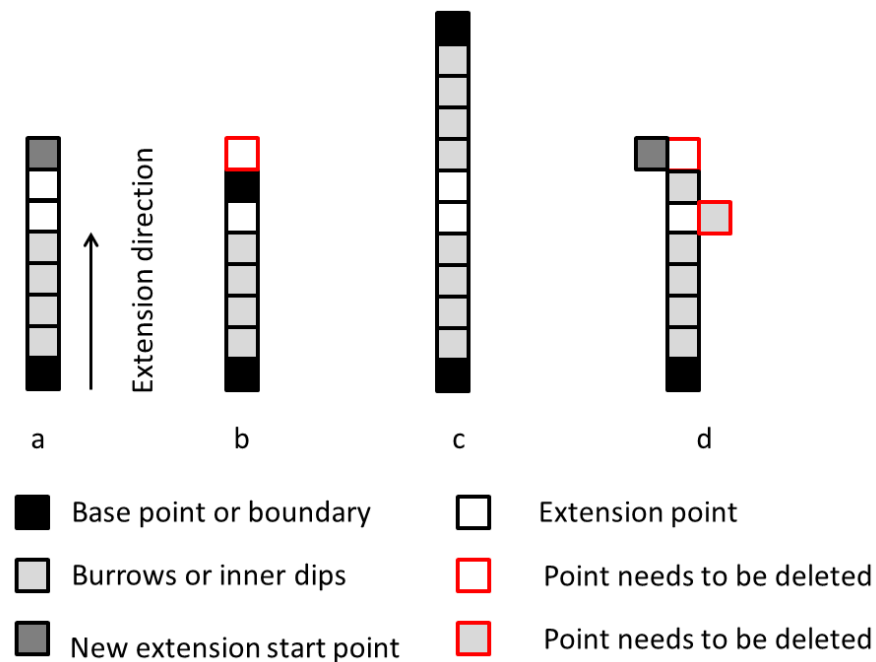


Figure 3.4. Four situations may happen during extension (step size is 3).

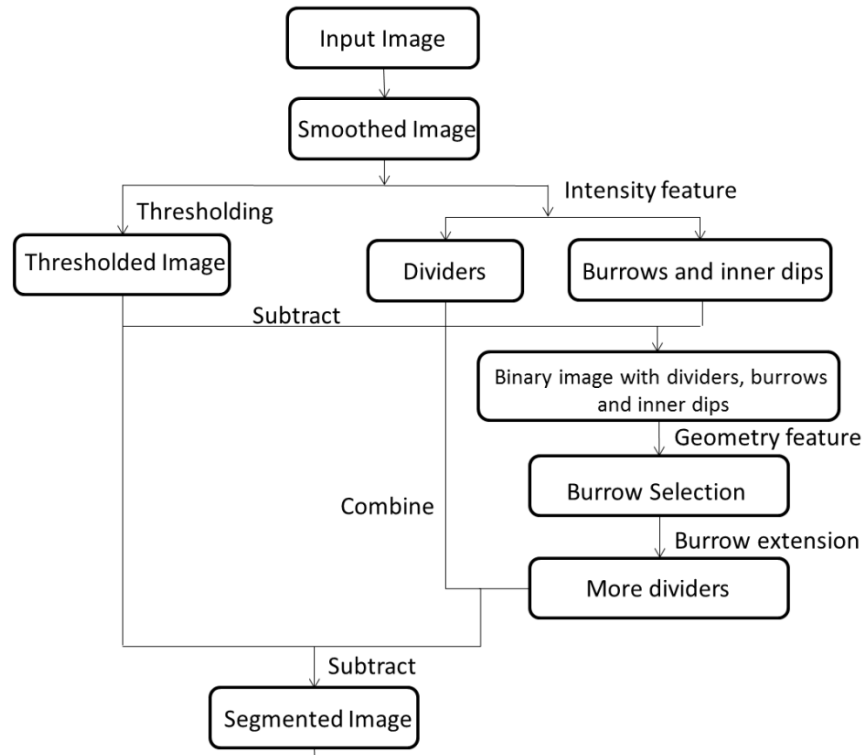


Figure 3.5. Methodology combining intensity and geometry features for particle image segmentation.

3.5 Case Study

A sample of particle image, which is the same one used in Chapter 2, with particle labels and a white horizontal line passing through a region of overlap marked by the oval is shown in Figure 3.6. The original grey particle image in a JPG format was imported into MATLAB for processing. Visual observation reveals a total of 16 particles in this image, all of which are sequentially labeled from 1 to 16. The original image has been normalized that all the pixel values are in the range of 0 to 1 for the purpose of easy calculation.

3.5.1 Smoothing Strategy on Particle Images

Although the whole image will go through noise removal steps, the pixels along the white horizontal line in Figure 3.6 will give an example of this strategy without losing the features of

interest. Figure 3.7 shows the intensity variation along the line. The valley in the intensity profile which highlighted by an ellipse indicates the overlapping region. The aim of smoothing is to remove noises but keep the valley regions.

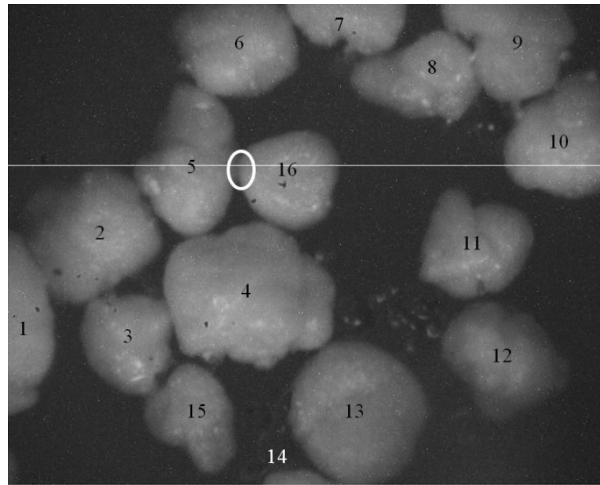


Figure 3.6. Original image with a horizontal line and particle labels

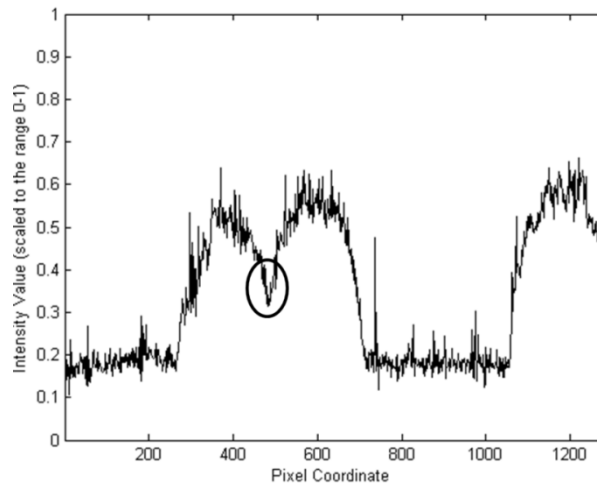


Figure 3.7. Intensity variation along the horizontal line

The smoothing process starts by filtering the image with Gaussian kernel of spread $\sigma = 1$ and then filters the resultant image again with a kernel of increased spread. This process is repeated with spread of Gaussian kernel being incremented in a small step of 0.2 each time. The

mean value of a measure of disorder (standard deviation or entropy) of the image at every step is calculated. This measure of disorder decreases considerably during initial iterations of smoothing and as the image gets smoothened, the change becomes less. The percentage change in the measure of disorder between two consecutive convolution results is used as the stopping criterion for smoothing. When the percent change is less than a predefined value, the smoothing is stopped and the result image is used for further processing. In this work, the predefined value is set as 0.01 and the smooth iteration stops at the 17th run with the σ of 4.2. The change of mean value of standard deviation of the pixel intensity for successively smoothened images is shown in the graph of Figure 3.8. Figure 3.9 gives the intensity plot along the horizontal line for various levels of smoothing (with increasing value of σ at several values). Offsets are applied to shift the graph vertically for better visual comparison. The arrow is kept as an index to the region of overlap / touch. As can be seen from the uppermost graph, which correspond to the condition when the percentage change is very less in standard deviation, the curve becomes smooth and valley regions corresponding to the touching / overlapping regions are quite well preserved. Figure 3.10 gives the smoothed image with σ equals to 4.2.

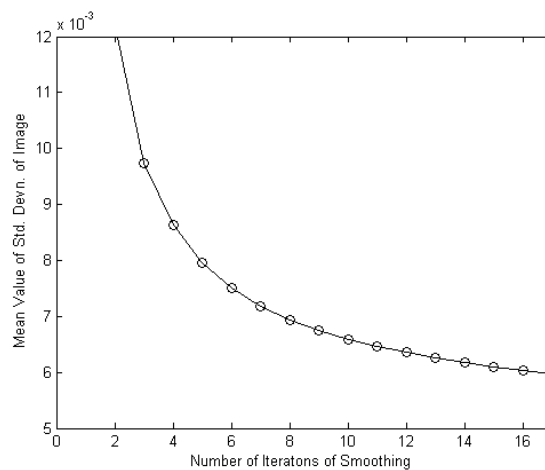


Figure 3.8. Changes in the mean value of standard deviation as smoothing progress

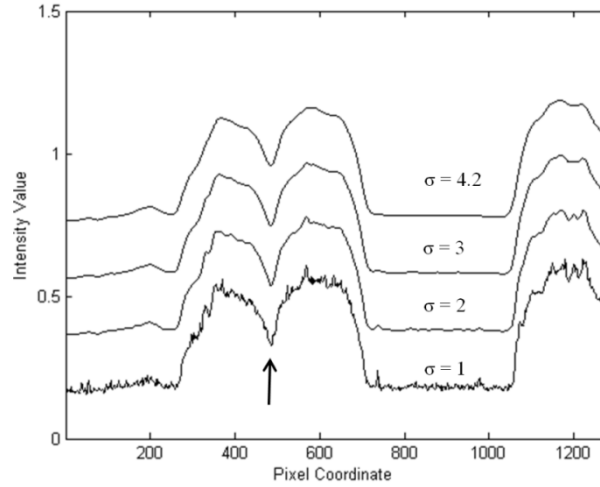


Figure 3.9. Influences of smoothing on the intensity variations along the horizontal line

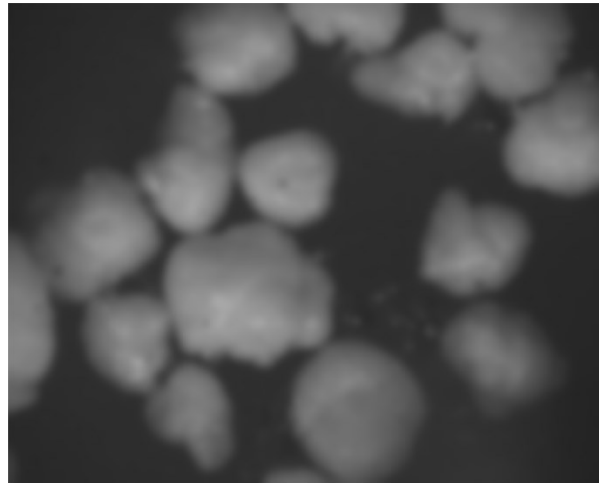


Figure 3.10. Smoothed image with $\sigma = 4.2$.

3.5.2 Segmentation by Thresholding on Particle Images

Performing thresholding operation on Figure 3.10 with Otsu's threshold value selection method generates a binary image as shown in Figure 3.11. The thresholding value calculated is 0.3255, thus any intensity above 0.3255 is considered as objects, otherwise backgrounds. However, in the case where a single particle touches many others, or one particle touching another which in turn touching another and so on, the result is one single large object labeled 1 in

the binary image rather than many individual particles. This is because that the regions in the gray image where the particles touch and overlap appear darker compared to the particle body and indeed have lesser intensity relatively but the intensity level in many of those regions is not as low as the background level. Hence thresholding alone cannot achieve the goal of obtaining individual objects and further segmentation operations are necessary.

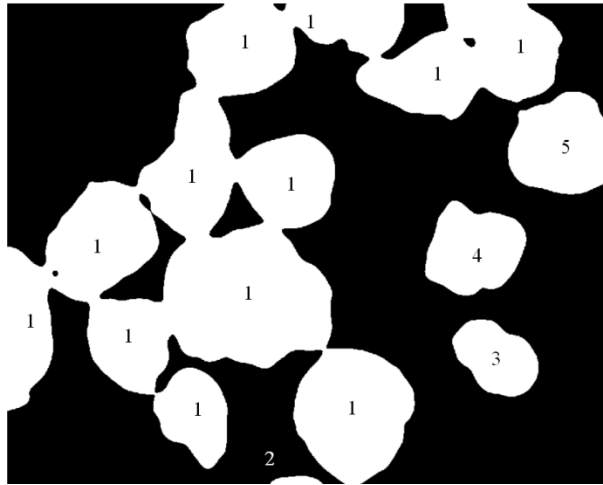


Figure 3.11. Thresholded image of Figure 3.6 with particle labels

3.5.3 Segmentation Using Valley Points on Particle Images

When applying the algorithm for detecting valley points on the processed reference image shown as Figure 3.10, the two parameters, the minimum valley depth and the search window, were chosen as 0.007 and 21 on experience. The neighborhood masks for the search along horizontal, vertical and diagonal directions were $H (1 \times 21)$ of 1s, $V (21 \times 1)$ of 1s, and $D (21 \times 21)$ as the identity matrix and its left-to-right flip matrix. 2-D order statistic filtering was used to find local maximum and minimum values for each pixel. Pixels which generate differences of the local extreme less than or equal to the minimum valley depth were considered as flat regions such as the object bodies themselves in this case. The other pixels contain

information of large intensity change but only the ones whose values are just the minimum in the search window could be the desired points. To reduce the influence of non-removed noises, the valley points belonging to the object area which was demarcated by the thresholded image were retained and any other (noise) presenting in the background region was ignored. The remained valley points are shown in Figure 3.12a. Most of these valley points form lines of connected pixels though some are broken due to effect of noise still left in the smoothened image or the roughness of the object surfaces.

Subtracting the valley point image (Figure 3.12a) from the thresholded image (Figure 3.11) leads to Figure 3.12b. Dividers completely separate some of the joints giving rise to new objects, identifying 15 particles. Burrows and inner dips scatter on the objects. Eye examination shows that most of them are disturbances expect the one along the touching area in Particle 12. Disturbances happen commonly in real life experiences. An automatic approach, using the geometric features of touching and overlapping area, can quantitatively identify the real burrows from disturbances.

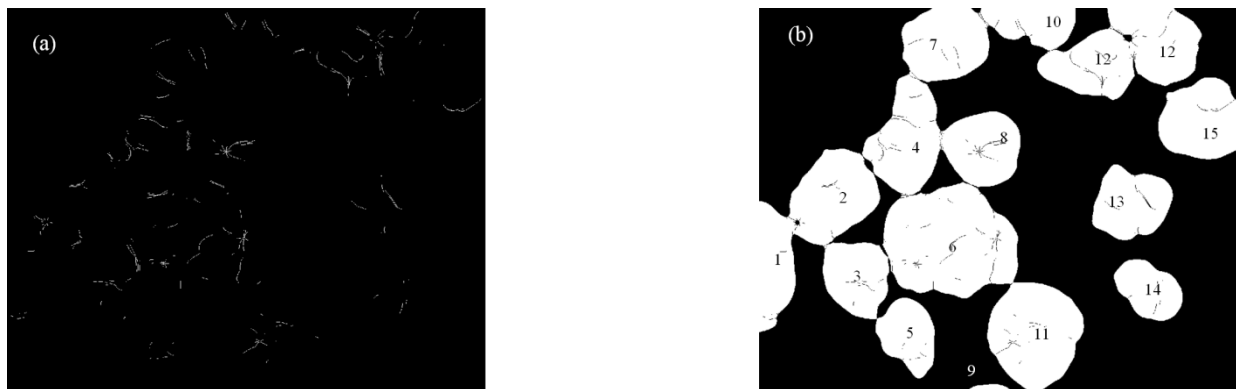


Figure 3.12. (a) Valley points and (b) Separation result by subtracting the valley points from the threshold image.

3.5.4 Complete Segmentation Using Geometric Features

To utilize geometry information, the eccentricity of every point on the boundary for each identified particle in Figure 3.12b was calculated. A threshold value determining high concavity was set as 1.5 in this case. Burrow selection indicated that burrows in all the detected particles in Figure 3.12b were disturbances except Particle 12. Also not all the burrows in Particle 12 were real ones; only three were. The selected burrows, A, B and C, are shown in Figure 3.13a (they were magnified for better visibility).

Burrow extension carried out with a step size of 3. Figure 3.13b gives the extended burrows. Burrow A is a kind of divider since its end points 1 and 3 are located at the boundary, thus it was not extended. Tip 6 of Burrow B in Figure 3.13a was chosen as the front tip to start extension other than tip 5 because tip 6 has the longer distance from base point 4. Burrow B and C connect to each other during extension and form a divider. The extended burrows plus previous dividers detected from intensity profile led to the final segmentation. Figure 3.14 shows the segmented image after morphology operations to remove the redundant parts of extended burrows.



Figure 3.13. (a) Selected burrows and (b) Extension of selected burrows. (They were magnified for better visibility).

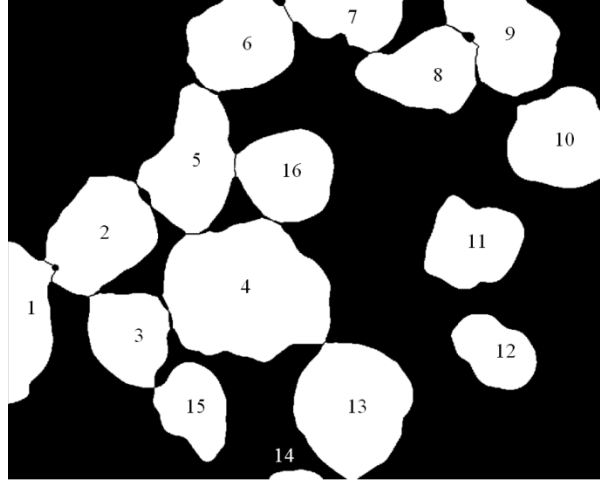


Figure 3.14. Separated image

3.6. Results and Discussion

The particle number, particle equivalent diameter, and particle size distribution (PSD) are considered to characterize particles. The equivalent diameter, defined as the diameter of a circle that has the same area of that object, is used to describe the size of the particles. It is counted as the number of pixels. PSD provides direct information of the distribution of the equivalent diameters in a certain range and their normalized frequencies. The histogram of equivalent diameters and their fitting curves through Weibull density probability function are used to describe the PSD. The segmentation results by watershed and manual methods are compared with those by the proposed algorithm to illustrate the separation efficiency.

3.6.1 Compare with Watershed Method

The use of watershed segmentation and its variants for separating touching and overlapping objects in particle images is reported in literatures [8] and a comparison of the results from the present method is made against results from the watershed algorithm. Watershed algorithm suffers from the disadvantage of severe over segmentation more so when objects are of

irregular shape and the intensity variations are present within the single object as shown in Figure 3.15a. The image is severely over segmented that the result is meaningless. To overcome this deleterious effect, two variants of watershed algorithm namely, the one based on distance transform and the one using pre flooding are normally employed. In the first variant, the distance transform of the complement of the binary image is taken and watershed algorithm is applied to it. The result is shown in Figure 3.15b. This method is too shape sensitive and fails when particles are of irregular shape which is the case for the particle domain of our interest. In the other variant, over segmentation is prevented by pre flooding very small minima and enforcing minima only at predefined locations with use of markers. Markers for object and back ground areas are to be identified first in this method. The object markers were chosen as those pixels which belong to the peak on the higher side of the threshold value in the image histogram. Object pixels with highest frequency can be a good choice for marking objects. Markers for the background are obtained from the thresholded image directly. Using such imposed minima, watershed segmentation was done and the result is shown in Figure 3.15c for the reference image. Though the level of over segmentation is less than that in other watershed methods, still the result is much inferior to that of the algorithm proposed in the present work.

3.6.2 Comparison with Manual Measurement

The touching and overlapping phenomena will have impact on the count of particles and calculated particle sizes since such objects in the thresholded image will be treated as single connected components. There were only 5 objects in the as thresholded image in Figure 3.11 and the largest object had an equivalent diameter of 768 pixels. The largest object corresponds to the central object in Figure 3.6 which consists of a number of overlapped and touching objects. On

the other hand, the proposed algorithm decomposes such overlapping and touching objects and the effect of this separation is reflected in the number and size of objects in the separated image. The image in Figure 3.15 has got 16 objects and the largest object has an equivalent diameter of 325 pixels. It can be seen that the highly overlapped central object as well as other touching and overlapping ones have been decomposed into individual objects by the separation algorithm.

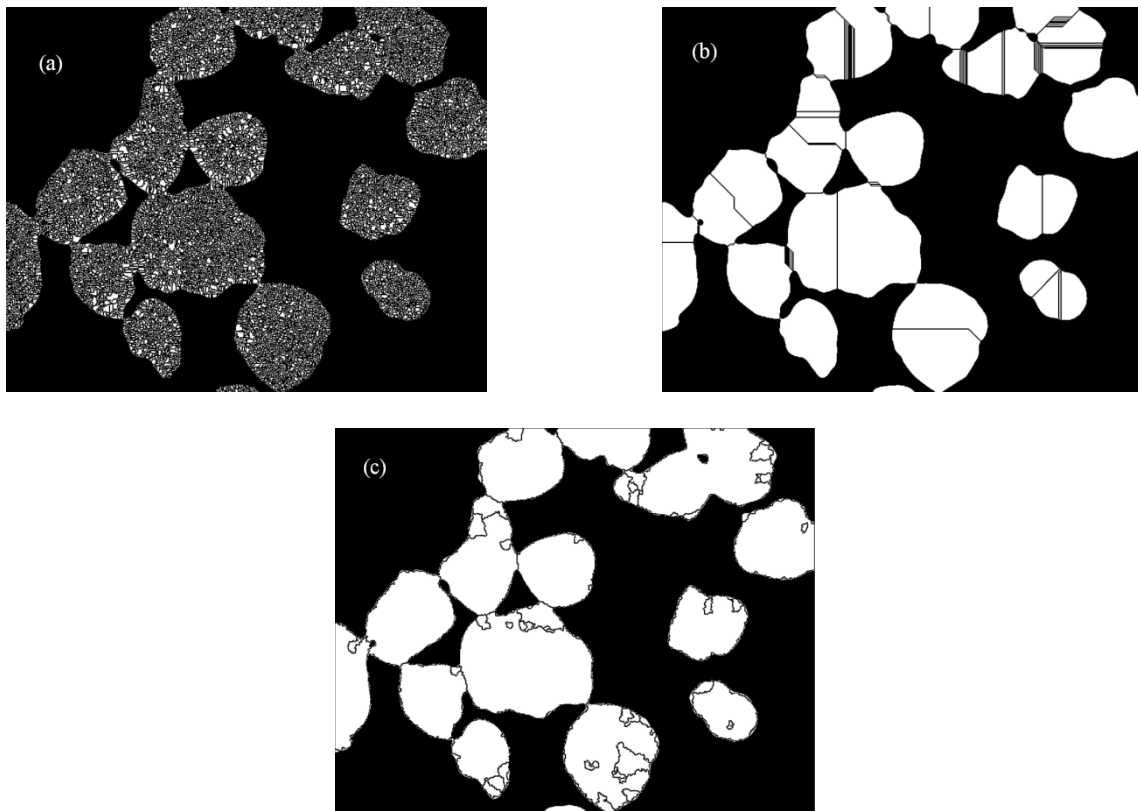


Figure 3.15. Watershed algorithm: (a) On gray image (b) On distance transform (c) With markers.

This algorithm generates segmentation results much close to the actual situation. Visual examination shows that 16 particles contained in the original image and the largest object has an equivalent diameter of 330 pixels measured by software AMSCOPE. PSD of the manual processed image and separated image are shown in Figure 3.16a and 3.16b respectively. PSD

obtained by manual processing (Figure 3.16a) illustrates that a large proportion of particles actually have equivalent diameters in the range of 150 to 250 with a small amount of particles have sizes between 50 and 150, and between 250 and 350. This proportion and equivalent diameter range are considered as a reference for PSD generated via the intensity-geometry approach. From PSD for the proposed method (Figure 3.16b), we can find that it is very close to the reference.

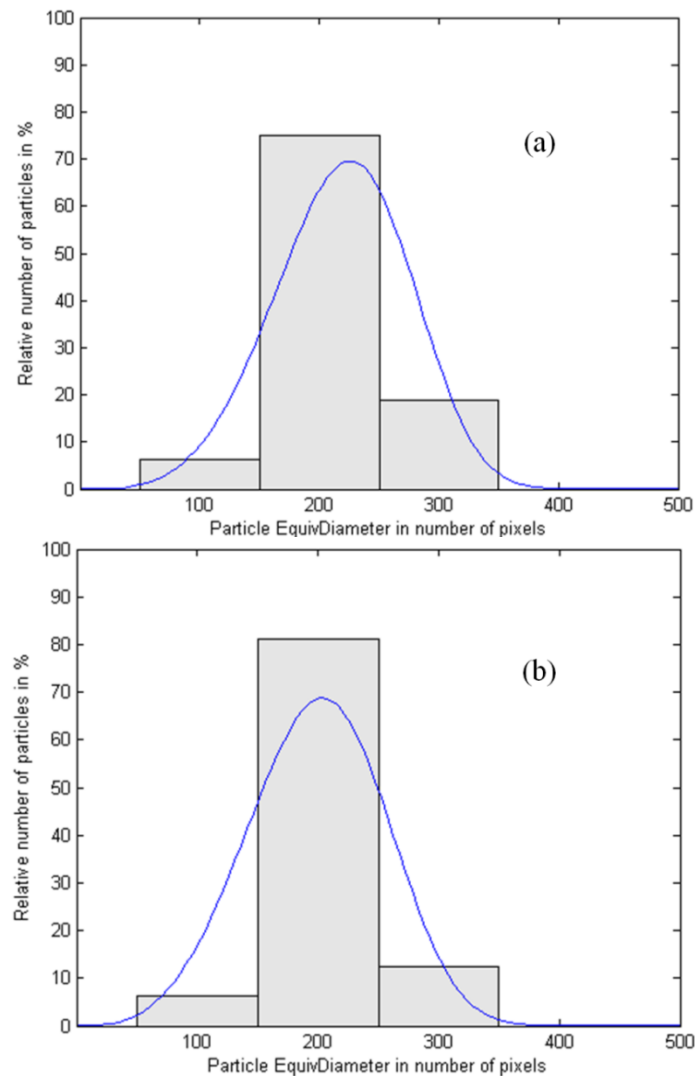


Figure 3.16. Particle size distribution of: (a) Manual measurement, (b) Segmentation using proposed approach.

3.7. Conclusions

An approach for segmentation of touching and overlapping areas contained in particle images is proposed. A strategy for automatic termination of smoothing process of the image based on rate of change of an appropriate measure of disorder like standard deviation of pixel intensity is proposed as the noise removal method. Segmentation includes thresholding, detecting and applying intensity features of the touching and overlapping regions, and separating combining with their geometric features. Valley points in intensity along the regions of touching and overlapping objects are found. The discontinuities in the detected valley lines are reduced by linking the segments using perceptual grouping factors of proximity and orientation. Orientations of the tips of the segments are determined by a novel approach to get more realistic results. The valley lines which do not completely cut the joints are extended in an iterative manner subject to their suitability of becoming a dividing line based on their orientation and presence of concavity on the boundary curve. The proposed method was compared against watershed algorithm and gave better results than the watershed methods. It can generate results close to the real situation. This approach can be used as a potential monitoring tool for particulate systems.

3.8 References

- [1] J. M. Korath, Image-based Monitoring of Particulate Processes, PhD thesis, The University of Sydney, 2008
- [2] B. Zhang, A. Abbas, J. A. Romagnoli, Multi-resolution fuzzy clustering approach for image-based particle characterization for particle systems, *Chemometrics and Intelligent Laboratory Systems*, 107 (2011) 155-164.
- [3] E. H. van den Berg, A. Meesters, J. A. M. Kenter, W. Schlager, Automated separation of touching grains in digital images of thin sections, *Computers & Geosciences*, 28 (2002) 179-190.
- [4] L. P. Shen, X. Q. Song, M. Iguchi, F. Yamamoto, A method for recognizing particles in overlapped particle Images, *Pattern Recognition Letters*, 21 (2000) 21-30.

- [5] R. E.W. Rafael, C. Gonzalez, S. L. Eddins, Digital image processing using matlab, Dorling Kindersley, 2004.
- [6] J. Babaud, A. P. Witkin, M. Baudin, R. O. Duda, Uniqueness of the Gaussian Kernel for scale-space filtering, IEEE Transactions on Pattern Analysis and Machine Intelligence, 8 (1986) 26-33.
- [7] N. Otsu, Threshold selection method from gray-level histograms, IEEE Transactions on Systems, Man, and Cybernetics, 9 (1979) 62-66.
- [8] S. Kucheryavski, K. H. Esbensen, A. Bogomolov, Monitoring of pellet coating process with image analysis-a feasibility study, Journal of Chemometrics, 24 (2010) 472-480.

CHAPTER 4. AUTOMATIC IMAGE-BASED ESTIMATION OF TEXTURE ANALYSIS AS A MONITORING TOOL FOR CRYSTAL GROWTH *

4.1 Introduction

Extracting accurate size information has been brought up as the key issue when introducing computer vision system for process inspection application in the first section. Touching and overlapping problem in particulate images is common a barrier to obtain real information. Chapter 2 proposed the multi-resolution fuzzy clustering approach that can successfully deal with touching areas. Advance segmentation algorithms based on taking advantage of the characteristics of both intensity and geometry of the touching and overlapping regions has been introduced in Chapter 3. As the overlapping problem becomes severe, effective and low cost methodologies are in high demand. The following chapters take this challenge.

Crystallization, as one of the widely used production and separation process, is a typical particulate system which provides an excellent challenge to investigate the image-based approach for particle characterization.

The optimization of properties of crystals such as shape, size, orientation and distribution plays an important role in chemical, biotechnological and pharmaceutical engineering since they determine textural and physical properties of the final commercial products. In recent decades, the relationship between the properties of end products and the crystal structure including both internal [1] and external has been intensively investigated. Crystal size, as an important external crystal structure, can largely influence the textural and physical properties of the final commercial products. For example, crystal size can potentially reduce the bioavailability of formulated products if it slows down dissolution [2]. Properties of end-product crystals are related to process parameters including temperature, flowrate of anti-solvents, seeding variables

*Portions reprinted from *Chemometrics and Intelligent Laboratory System*, Copyright 2013

and agitation and so on [3]. In reality, inevitable process disturbances occur during crystallization affecting these properties and hence product quality. Monitoring and controlling crystal growth by characterizing crystals such as size is critical not only for quality control of end products but also for proper design and development of crystallization processes.

Existing measurement methods of crystal size include sieving analysis, sedimentation analysis, sensing zone methods, optical methods, Fraunhofer diffraction, light pulses and image particle counters [4]. The sieve method is probably widely used in production environments since it requires low technology equipment and the technique is simple and relatively straightforward. However, it has disadvantages such as needs of a relatively long preparation and measurement time, making limited application in on-line control and monitoring, and generating inaccurate results when dealing with samples containing excessive agglomeration [5]. Sedimentation analysis, sensing zone methods, optical methods, Fraunhofer diffraction and light pulses for determining size are based on a crystal suspension. The properties of the fluid in which crystals are dispersed, for example, density, viscosity, the degree of crystal agglomeration in the fluid, affect analysis accuracy. The concentration of the suspension is a considerable factor when using those methods. For example, optical techniques are constrained by the concentration of the suspension which render on-line measurement of crystal size feasible only if at dilute concentrations [4].

Digital images obtained from on- or off-line cameras, have become a powerful measurement tool due to developments in high speed digital imaging devices, equally powerful computers at reasonable costs and the adaptability to real-time application [6]. The determination of crystal mean size can be achieved by manual and automatic methods. Manual method, counting and measuring crystals by hands (using especial software), involves tedious and

arduous physical work and is time consuming. Automatic counting and size measurement techniques for a given image, on the other hand, are more interesting and practical especially for on-line process control and monitoring applications. Dalziel et al [7] developed an image analysis system for crystal sizing depending on the crystals' roundness. This system works well if single crystals can be recognized, but would not perform well when clusters of crystals and overlapping and touching crystals exist. Mhlongo and Alport [8] proposed a crystal size prediction technique using wavelet analysis and an artificial neural network. The mean percentage error between predicted and actual mean size for crystal images obtained from a laboratory crystaloscope immersed in a glycerine solution of sugar crystals was 12.9%. However, the concentration of the solution and the scenario of crystals suspended in the solution are unknown, making the application rather specific. The SHARC algorithm reported by Larsen et al [9] can extract particle size distribution information for moderate solids concentrations but declines for high levels of particle agglomeration. Adopting digital images to automatically measure size is promising but still faces challenges.

A key challenge for automatic crystal imaging techniques is the touching and overlapping or agglomeration problem existing in crystal images. For low or medium solid concentration suspensions, physical dispersion is used to avoid this phenomenon prior to capturing the images. This can reduce but cannot eliminate touching and overlapping events because of the fact that dispersed crystals will flow together or ecliptically. For high solid concentration suspensions, this problem is even more common and no practical algorithm is available for on-line use. Reported algorithms for measuring size on individual crystals may not be reliable when the touching and overlapping problem happens [10]. Zhang [11] proposed a multi-resolution fuzzy clustering approach to segment the touching areas between particles. However, the overlapping

problem is very difficult to be solved by this approach or other available computer techniques to identify individual crystals [12]. Instead of detecting and characterising every crystal, it is possible to extract size information by performing texture analysis on crystals irrespective of whether they are individuals or are touching and overlapping each other. It can be shown that images for small size crystals have a ‘rough’ texture, while those for large size are relatively ‘flat’.

In this chapter, a novel approach is proposed for crystal image texture analysis based on combining thresholding and wavelet-fractal-energy algorithms. Thresholding method can quickly detect crystal clusters and remove the background based on the intensity value and is a good choice for real-time application. Fractal dimension (FD) as the texture analysis parameter [13-16], estimated through a wavelet-fractal approach [14,17,18], is a useful and quantitative analytical parameter to characterize many kinds of complicated self-similar substances in nature. Wavelet power spectra have been widely adopted for analysis in chemical fields [11, 19-22]. FD provides a non-integer value to describe crystal growth from crystal images from the point of view of surface roughness. Generally, the higher the value of the fractal dimension, the more rough the surface is. The pre-processing step of subtracting backgrounds eliminates their contribution to surface roughness. Furthermore, energy signatures, obtained from the wavelet coefficients, are utilized in the approach to build a statistical model towards the estimation and prediction of the mean crystal size from images taken along a typical crystallization run. The proposed approach can not only provide automatic texture estimation from crystal images but also has potential application for future use in on-line monitoring and control of crystal production processes.

The chapter is organized as follows: The algorithms of thresholding and wavelet-fractal are first introduced in detail in Sections 4.2 and 4.3. In Section 4.4, we illustrate the proposed methodology using a case study involving a crystal image sample. The results and discussion of fractal dimension from crystal images obtained during a crystal growth process are given in Section 4.5. Finally, conclusions are presented in the last section.

4.2 Thresholding Method

Crystal images always contain background information which is removed leaving behind only information related to the crystals for the purpose of texture analysis and crystal feature extraction. The texture properties of the background such as smoothness can largely affect the analysis of the texture of the crystals. For instance, the presence of more background information leads to the texture of an image being smoother. In another case, the texture of crystals will also be smoother when larger crystals exist in the image. Thus, detecting crystals themselves or removing backgrounds are essential to accurately perform texture analysis. Typically, the edges of crystals appear darker in crystal images and thus have lower intensity values compared with backgrounds and with crystals themselves. Crystals, on the other hand, have similar intensity values as the background due to the fact that crystals are transparent and illuminations on both of them are similar during the image acquisition process. The threshold method is applied here to identify the crystal edges and remove the background.

4.3 Texture Analysis by Wavelet Transform

On the examination of crystal images, it can be found that crystal size information reflects on the intensity variation in a given small neighborhood: images for small crystals

contain more variations compared with those for large crystals. Capturing crystal size information equals describing these spatial variations in pixel intensities. Implementing texture analysis can catch the spatial variations and present them as textural features.

Wavelet transform, a recent multi-resolution technique, can extract textural characteristics from crystal images. It can decompose a signal into several details and an approximation. Details carry the characteristic information such as edges of distinct objects distinguishing its corresponding signal from others. The approximation, on the other hand, usually reflects the intensity variance generated by lighting or illumination [21]. Thus extracting features from details is more appropriate than from the approximation. As the number of crystal edges is the distinction between small and large crystals in images, texture features can be obtained from the point of energy distribution. Wavelet energy signature, the variances of details at several scales, is adopted as texture features under the assumption that each texture displays its unique energy distribution at all scales. Under the consideration of the combination of energies at all scales, fractal dimension which is acquired from the scaling of energies is another texture feature.

4.3.1 Wavelet Energy Signature

After wavelet decomposition, the energy E_m stored in the detail coefficients at scale index m is calculated in the following equation

$$E_m = \sum_{n=0}^{2^{M-m}-1} (T_{m,n})^2 \quad (4.1)$$

Dividing the 2^{M-m} on both sides, we get

$$\frac{E_m}{2^{M-m}} = \frac{\sum_{n=0}^{2^{M-m}-1} (T_{m,n})^2}{2^{M-m}} \quad (4.2)$$

where the left-hand side is also equal to the commonly used coefficient variance at scale m , which is labeled $\langle T_{m,n}^2 \rangle_m$. According to this expression, wavelet coefficient variance can be explained as the average energy wrapped up per coefficient at each scale m . In this context, the detail variance is used as the wavelet energy signature.

4.3.2 Fractal-Wavelet Feature

Fractal dimension (FD) is a statistical real number that measures how complicated a fractal is. Fractals are objects that possess self-similar property, where fractals appear identical at different scales or numerical or statistical measures of fractals are consistent across scales. The reason why FD is selected as the texture feature is that the dynamics of crystal growth follows a fractal process [15] and crystals in images exhibit statistical self-similarity in reality. Several approaches are available for calculating FD and we here use fractal-wavelet method which requires not only wavelet decomposition but also fractional Brownian motion (fBm) model.

A fBm is a continuous-time Gaussian process defined as a non-stationary and zero-mean Gaussian random function shown in the following equation [23]:

$$\begin{aligned} B_H(0) &= 0 \\ B_H(t) - B_H(s) &= \frac{1}{\Gamma(H + 0.5)} \left\{ \int_{-\infty}^0 [(t-s)^{H-0.5} - s^{H-0.5}] dB_H(s) \right. \\ &\quad \left. + \int_0^\infty (t-s)^{H-0.5} dB_H(s) \right\} \end{aligned} \quad (4.3)$$

where B_H represents the Gaussian process with observation time at 0, t and s . Γ is the Gamma function.

The Hurst exponent, H , has a value between 0 and 1 characterizing fBm. It is an indicator to reflect the smoothness of the fBm function: the higher the Hurst exponent is, the smoother the fBm function is. Hurst exponent is directly related to FD via the relationship

$$FD = D_E + 1 - H \quad (4.4)$$

Here D_E is the Euclidean dimension.

For an fBm, it also scales to wavelet power spectra $P_w(f_m)$ and frequency f_m such as:

$$P_w(f_m) \propto f_m^{-(2H+1)} \quad (4.5)$$

where \propto means the constraint is proportional. Meanwhile, wavelet power spectra $P_w(f_m)$ is related to the variance of discrete wavelet coefficients as:

$$P_w(f_m) \propto \langle T_{m,n}^2 \rangle_m \quad (4.6)$$

Combing Equation (4.5) with (4.6), and the fact that frequency f_m is inversely proportional to the wavelet scale a_m , the scaling relationship becomes:

$$\langle T_{m,n}^2 \rangle_m \propto a_m^{(2H+1)} \quad (4.7)$$

Computing Hurst exponent, then FD, can be achieved through taking base 2 logarithms of both sides of Equation (4.7), showing in Equation (4.8). The logarithmic plot of variance of discrete wavelet coefficients provides a method of deciding Hurst exponent from the slope of the plot.

$$\log_2(\langle T_{m,n}^2 \rangle_m) = (2H + 1)m + \text{constant} \quad (4.8)$$

where the constant depends both on the wavelet function and the Hurst exponent.

4.4 Method for Texture Analysis from Crystal Images

To illustrate the procedures of texture analysis from crystal images, a methodology flowchart and a case study on a single image are discussed and implemented in this section. The flowchart provides an explicit and concise schematic view on how this approach operates combining thresholding and wavelet-texture algorithms. A case study, including a single image taken during an experimental run at the initial crystallization stage, shows the application of the methodology step by step. The remaining crystal images at other crystallization stages (samples at different time during the crystallization process) were also investigated and their analysis will be discussed in the remaining sections.

4.4.1 Methodology

The essential and sequence of steps for implementing the proposed methodology for texture analysis from crystal images are given in Figure 4.1. An input image is treated as a 2D array of pixel intensities. A thresholding algorithm is applied for extracting features of interest which are the crystal clusters in this work. This is accomplished through a series of three sub-steps: a) detection of crystal edges by a threshold value differentiating them from the background, b) detection of the locations of the crystal clusters with the help of x-y coordinates on the binary image of crystal clusters, and c) determining and extracting the intensity values belonging to the crystal clusters. The information data of the clusters is then restored into a vector, being processed to generate the texture features by means of wavelet-fractal-energy algorithm. In this regard, it is first decomposed by wavelet transformation at several levels into details and an approximation. The detail from lower decomposition level and the approximation are considered as the high and low frequency noise to be removed. The remained details are then used for

finding their variance and 2-based logarithm of the variance. The 2-based logarithm of the variance at each scale and decomposition scales are then plotted and fitted by a line whose slope is used to calculate the Hurst exponent and consequently the FD. The texture features can be used for further application such as establishing PLS model for the prediction of crystal mean size.

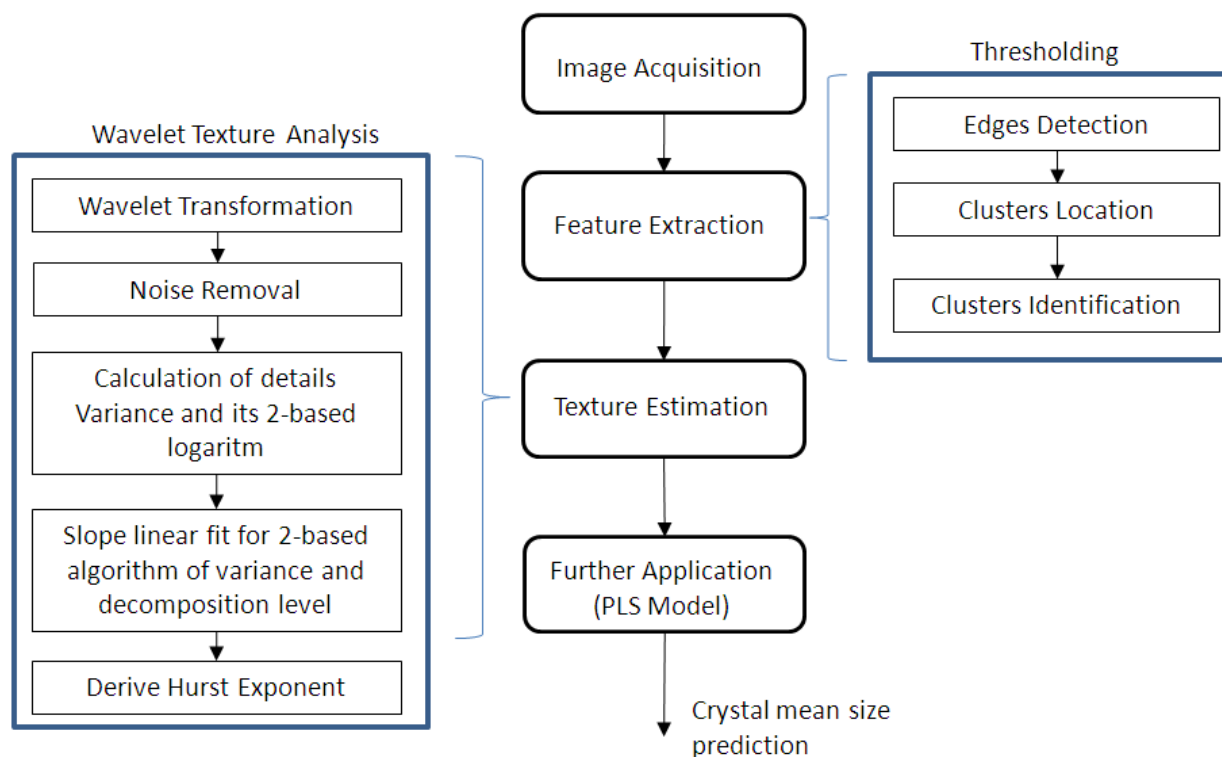


Figure 4.1: Flowchart of automatic texture analysis on crystal images.

4.4.2 Case Study

4.4.2.1 Experimental and Image Acquisition Setup

An experiment of an anti-solvent crystallization process was carried out, through the combination of the two main variables which can influence the speed of crystal growth (temperature and anti-solvent flowrate). In this study, the temperature was 30°C and anti-solvent flowrate was 1.5mL per min. The initial solution comprises 34g of NaCl with reagent grade

purity of 99.9% and 100g of deionised water. The solution was added into a 1L Erlenmeyer flask which was immersed into an isothermal temperature bath and mixing was provided by a magnetic stirrer. Ethanol whose reagent grade is 190 proof was added with a constant flowrate to the stirred solution using a peristaltic pump. 5 mL solution samples at 20min, 30min, 60min, 90min, 120min, 180min, 240min, 360min and 480min (labelled as Stages 1 to 9) were taken and filtered over filter paper with a vacuum pump and dried for further processing.

A laboratory scale software/hardware framework for capturing crystal images for this case study was setup. The experimental setting utilizes a USB microscope camera (model MD900) with a resolution of 2592 x 1944 pixels, which fits into the side tube on the side of the microscope with one of the supplied adapters and connects to a computer. The AMSCOPE software is utilized to capture images and for manual measurement (individual particle analysis). The magnification used is 25x which corresponds to 0.775 Microns/pixel. This conversion factor was used to manually measure individual crystal sizes on each image. At each crystal growth stage, a set of 7 images capturing different amount of crystals were utilized.

4.4.2.2 Fractal Dimension Estimation

A sample image from stage 1 is used to illustrate the method of FD estimation from crystal images. The original grey crystal image in TIF format was imported for image analysis. The original grey crystal image was compressed and cropped with Microsoft Office Picture Manager into a size of 700*760 in JPG format as shown in Figure 4.2a to improve execution time for further analysis. Then the cropped image was imported in Matlab for image analysis, wavelet analysis and PLS modelling. To make calculations simpler, the image intensities have been normalized with intensity value into a range of 0 to 1. The normalized image then

underwent thresholding and morphological operations to detect crystal clusters. Otsu's method generated a threshold value of 0.5020 for the normalized image; implying pixels with intensity value below 0.5020 belong to edges. Threshold method gave birth to a binary image shown in Figure 4.2b. The holes presented in the edge detection binary image correspond to crystal bodies in the original image. A morphological operation was used to fill the holes and generated the image shown in Figure 4.2c (crystal cluster binary image) which provides the location information of crystal clusters.

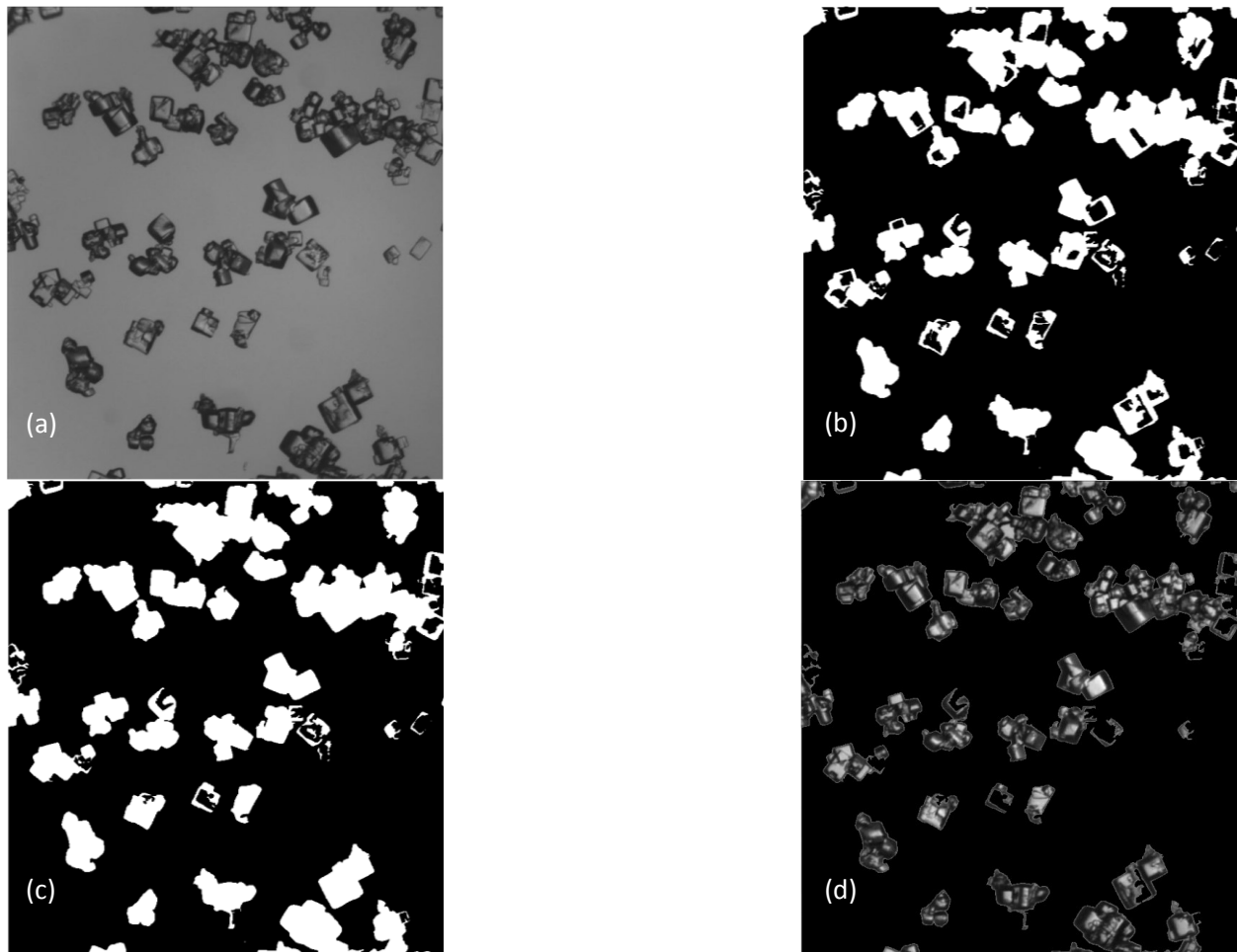


Figure 4.2: (a) Pre-processed, (b) Edge detection binary image, (c) Crystal clusters binary image, (d) Crystal clusters image.

The locations of each crystal cluster in crystal cluster binary image are the same as those in the original image since the size of the former image is the same as the latter. Identifying crystal clusters or subtracting backgrounds was achieved through determining the locations of crystal clusters and storing them in an empty image. The detected crystal clusters are depicted in Figure 4.2d.

The intensities of the crystal clusters were then rearranged in a sequence of the same column order connecting with the next row as a vector with a length of 113699. The rearrangement transfers the 2-D image problem into 1-D problem. The intensity vector was the input data for the wavelet-fractal analysis.

The wavelet function and decomposition level are the two parameters for wavelet transformation. In this study, wavelet function ‘db3’ was chosen and decompositions at five levels were performed. The transformation results can be written in the form:

$$W = \{cd_1, cd_2, \dots, cd_5, ca_5\} \quad (4.9)$$

where, W represents the signal data and cd and ca are details and approximation respectively. The subscript number indicates the decomposition level. We select details cd_2 to cd_5 for further analysis because cd_1 contains the high frequency noise and ca_5 captures the low frequency noise as non-uniform illumination. The variance of the detail coefficients and their 2-based logarithm were calculated as listed in Table 4.1. Performing a least-square linear fit for 2-based logarithm of the detail variance and its corresponding decomposition level, as shown in Figure 4.3, we found the slope was 1.94. Using equations (4.8) and the previously calculated slope, we calculated the Hurst exponent to be 0.47 and FD, according to equation (4.4), to be 1.53 when 2 was adopted as the Euclidean dimension for 1-D situation.

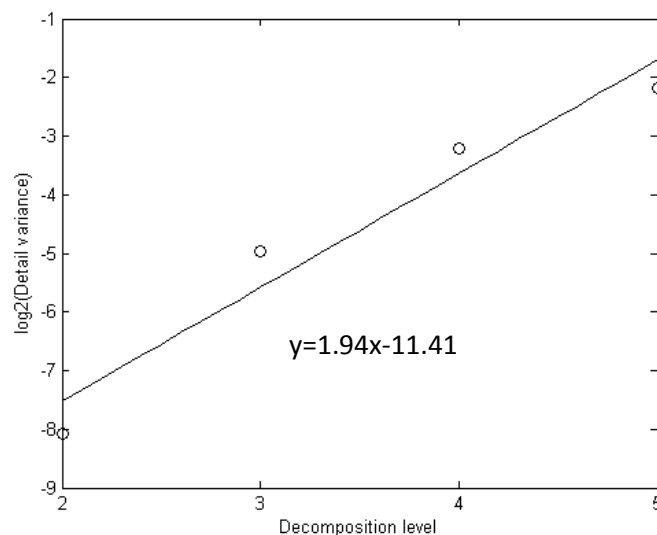


Figure 4.3: $\log_2(\text{detail variance})$ against decomposition level plots with the linear fitted line. The Hurst coefficient can be obtained through the fitted equation.

Table 4.1: Detail variance and its 2-base logarithm at four decomposition level

Decomposition level	2	3	4	5
Detail Variance	0.004	0.032	0.108	0.219
2-based logarithm of detail variance	-8.075	-4.958	-3.216	-2.190

4.5 The Relationship between Fractal Dimension and Crystal Growth

This section focuses on investigating the relationship between the FD (and Hurst exponent) and the growth of crystals with the sets of images from nine crystal growth stages during the antisolvent crystallization batch (for each sample a total of seven images were used, five for training and the remaining two for testing). One sample image at each stage of the crystallization process is given in Figure 4.4. The methodology for Hurst exponent/FD determination was applied on each image. The mean Hurst exponent/FD for each stage was the average value obtained from the set of images for that stage. The mean size for each stage was obtained from its corresponding image set which was measured manually by means of the sizing computer

software (Amscope®). Polygons were used, choice in the software, to approximate the crystals. The length, as the size information, was then transferred into micron units. Averages of the mean size for the crystals in the first 5 images were obtained, and provide the manually measured mean size in a confidence level of 90%.

The mean Hurst exponent, mean FD and measured mean size for each stage are listed in Table 4.2. Charts for the three prior items are plotted as well in Figure 4.5, distinctly displaying their tendency over time. During the crystallization process, the mean Hurst exponent and measured mean size increase sharply at the beginning and then increase gradually until they reach relatively constant values. The mean FD decreased quickly as time goes by to reach another relatively constant value. As expected, the figures illustrate that mean Hurst exponent/FD follows a similar/inverse changing pattern to measured mean size.

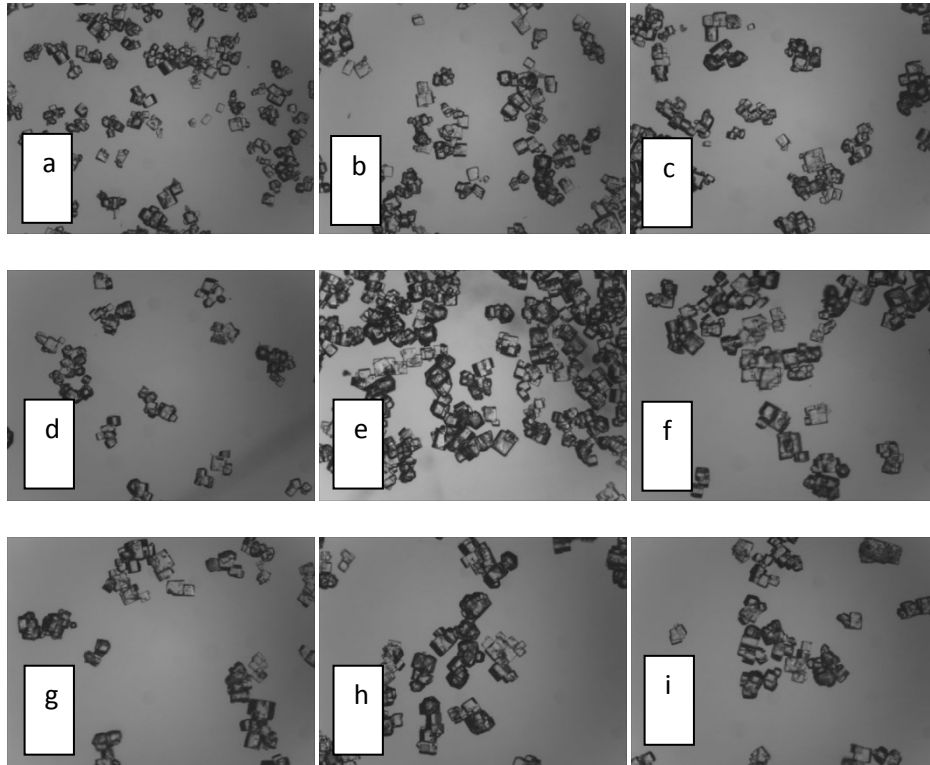


Figure 4.4: Sample images during crystal growth. a) to i) refers to stage 1 to 9.

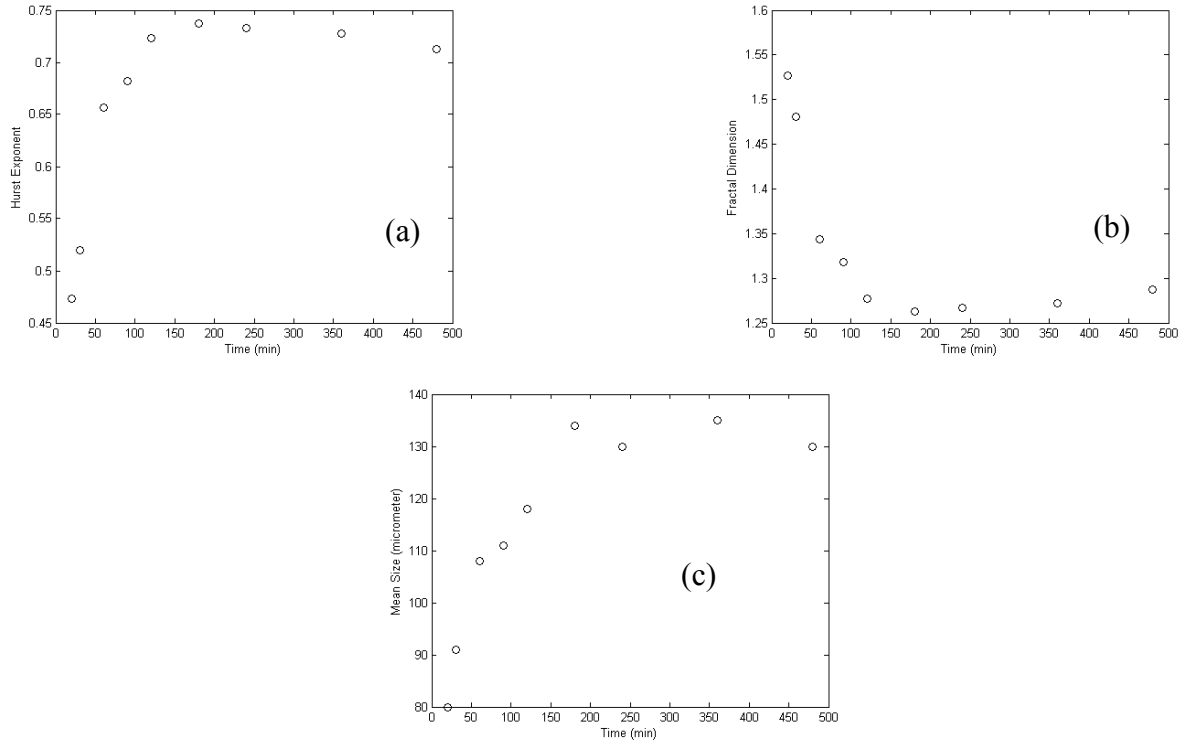


Figure 4.5: The change of mean Hurst exponent (a), mean FD (b), and manually measured mean size (c) during crystallization.

Table 4.2: The mean Hurst exponent, mean FD and manually measured mean size at each growth stage.

Stage	Mean Hurst Exponent	Mean Fractal Dimension	Manually Measured Mean Size(μm)
1	0.47	1.53	80
2	0.52	1.48	96
3	0.66	1.34	108
4	0.68	1.32	111
5	0.72	1.28	118
6	0.74	1.26	134
7	0.73	1.27	130
8	0.73	1.27	136
9	0.71	1.29	132

4.6 Conclusion

An image-based approach of texture analysis combining thresholding and wavelet-fractal for crystal growth monitoring was proposed and applied on a case study. This method could

successfully and automatically identify crystal clusters and estimate the texture by means of FD and wavelet energy signature. The FD transformation tendency during the crystallization process had been investigated with the results that FD decreases fast at the beginning of crystallization and slowly as time goes by. The changing pattern of FD and crystal mean size during crystal growth was compared showing their similarity.

4.7 References

- [1] B. Zhang, Z. H. Ni, A. L. Cui, H. Z. Kou, Heterometallic trinuclear (CuM₂III)-M-II (M = Fe or Cr) complexes with novel bridges and unusual magnetic properties, *New Journal of Chemistry*, 30 (2006) 1327-1332.
- [2] X. Z. Wang, K. J. Roberts, C. Ma, Crystal growth measurement using 2D and 3D imaging and the perspectives for shape control, *Chemical Engineering Science*, 63 (2008) 1173-1184.
- [3] K. Sangwal, *Additives and crystallization processes: from fundamentals to applications*, Wiley, John & Sons, Incorporated 2007.
- [4] J. Garside, A. Mersmann, J. Nyvlt, *Measurement of crystal growth and nucleation rates*, 2nd Edition ed., Institution of Chemical Engineers, 2002.
- [5] K. F. Miller, A. C. Beath, The measurement of raw sugar crystal size by sieving and by laser diffraction, *Proceedings of the 2000 Conference of the Australian Society of Sugar Cane Technologists* (2000) 393-398.
- [6] I. Scherze, R. Knofel, G. Muschiolik, Automated image analysis as a control tool for multiple emulsions, *Food Hydrocolloids*, 19 (2005) 617-624.
- [7] S. T. Dalziel, S. Y. White, E. T. Broadfoot, R., An image analysis system for sugar crystal sizing, *Proceedings of the Australian Society of Sugar Cane Technologists* (1999) 366-372.
- [8] A. Z. Mhlongo, M. J. Alport, Application of artificial neural network techniques for measuring grain sizes during sugar crystallization, *Proceedings Congress of the South African Sugar Technologists Association*, (2002) 460-468.
- [9] P. A. Larsen, J. B. Rawlings, N. J. Ferrier, An algorithm for analyzing noisy, in situ images of high-aspect-ratio crystals to monitor particle size distribution, *Chemical Engineering Science*, 61 (2006) 5236-5248.

- [10] P. A. Larsen, J. B. Rawlings, Assessing the reliability of particle number density measurements obtained by image analysis, *Particle and Particle Systems Characterization*, 25 (2009) 420-433.
- [11] B. Zhang, A. Abbas, J. A. Romagnoli, Multi-resolution fuzzy clustering approach for image-based particle characterization for particle systems, *Chemometrics and Intelligent Laboratory Systems*, 107 (2011) 155-164.
- [12] E. H. van den Berg, A. Meesters, J. A. M. Kenter, W. Schlager, Automated separation of touching grains in digital images of thin sections, *Computers & Geosciences*, 28 (2002) 179-190.
- [13] T. Hagiwara, H. L. Wang, T. Suzuki, R. Takai, Fractal analysis of ice crystals in frozen food, *Journal of Agricultural and Food Chemistry*, 50 (2002) 3085-3089.
- [14] K. M. Iftekharruddin, J. Zheng, M. A. Islam, R. J. Ogg, Fractal-based brain tumor detection in multimodal MRI, *Applied Mathematics and Computation*, 207 (2009) 23-41.
- [15] O. Velazquez-Camilo, E. Bolanos-Reynoso, E. Rodriguez, J. Alvarez-Ramirez, Fractal analysis of crystallization slurry images, *Journal of Crystal Growth*, 312 (2010) 842-850.
- [16] E. Barrera, F. Gonzalez, E. Rodriguez, J. Alvarez-Ramirez, Correlation of optical properties with the fractal microstructure of black molybdenum coatings, *Applied Surface Science*, 256 (2010) 1756-1763.
- [17] T. J. Kang, S. C. Kim, I. H. Sul, J. R. Youn, K. Chung, Fabric surface roughness evaluation using wavelet-fractal method - Part I: Wrinkle, smoothness and seam pucker, *Textile Research Journal*, 75 (2005) 751-760.
- [18] S. C. Kim, T. J. Kang, Fabric surface roughness evaluation using wavelet-fractal method - Part II: Fabric pilling evaluation, *Textile Research Journal*, 75 (2005) 761-770.
- [19] F. R. George, E. Klinzing, R. Marcus, L. S. Leung, *Pneumatic conveying of solids: a theoretical and practical approach*, Springer, 1997.
- [20] K. Jetter, U. Dępczyński, K. Molt, A. Niemöller, Principles and applications of wavelet transformation to chemometrics, *Analytica Chimica Acta*, 420 (2000) 169-180.
- [21] M. S. Reis, A. Bauer, Wavelet texture analysis of on-line acquired images for paper formation assessment and monitoring, *Chemometrics and Intelligent Laboratory Systems*, 95 (2009) 129-137.
- [22] P. Facco, A. Masiero, F. Bezzo, M. Barolo, A. Beghi, Improved multivariate image analysis for product quality monitoring, *Chemometrics and Intelligent Laboratory Systems*, 109 (2011) 42-50.
- [23] F. Biagini, Y. Hu, B. Oksendal, T. Zhang, *Stochastic calculus for fractional Brownian motion and applications*, Springer-Verlag New York, LLC, 2008.

CHAPTER 5. MULTI-RESOLUTION-MULTIVARIATE STATISTICAL IMAGE BASED APPROACH FOR CRYSTAL MEAN SIZE PREDICTION/CHARACTERIZATION*

5.1 Introduction

Texture analysis on particle clusters is appropriate on characterizing the crystal size if the overlapping problems are severe in images. Chapter 4 illustrates the algorithms of extracting size features by performing texture analysis. Wavelet energy signature, Hurst exponent and fractal dimension are used as the size features. However, those features are less direct and commonly used to represent size than length or diameters. Models that can link the statistical features and length will be welcome and required. Also it will be interesting to develop models that can monitor processes by using these statistical features without transfer them into length.

The paper is structured as follows. The multi-resolution-multivariate-statistics prediction methodology is provided in Sections 5.2, with Section 5.2.1 illustrating the sequence of steps for implementing the proposed methodology and the application in Section 5.2.2. The multi-resolution-multivariate-statistics prediction methodology is provided in Sections 5.2, with Section 5.2.1 illustrating the sequence of steps for implementing the proposed methodology and the application in Section 5.2.2. Section 5.3 develops multi-resolution-multivariate-statistics detection models, including illustration of principle component analysis, the architecture of corresponding methodology and the case study. Finally, Section 5.4 gives a conclusion.

5.2 Crystal Mean Size Prediction

Given the fact that mean Hurst exponent/FD has a similar/inverse change pattern to measured mean size during crystallization process from the Section 4.5, it is attractive to investigate the relationship between Hurst exponent/FD and measured mean size and then to

*Portions reprinted from *Chemometrics and Intelligent Laboratory System*, Copyright 2013

predict crystal mean size with new data. In this regard, partial least squares (PLS) regression, is used to find the linear relations between two blocks of data. PLS has been shown to be an effective prediction tool [1]. In this section, a PLS model will be established to find the linear relationship between Hurst exponent/FD and measured mean size and this model will be used to predict mean size as new information (new images) arrive at different sampling times. The overall architecture of the approach is illustrated in Figure 5.1, where both the training and testing steps are clearly described.

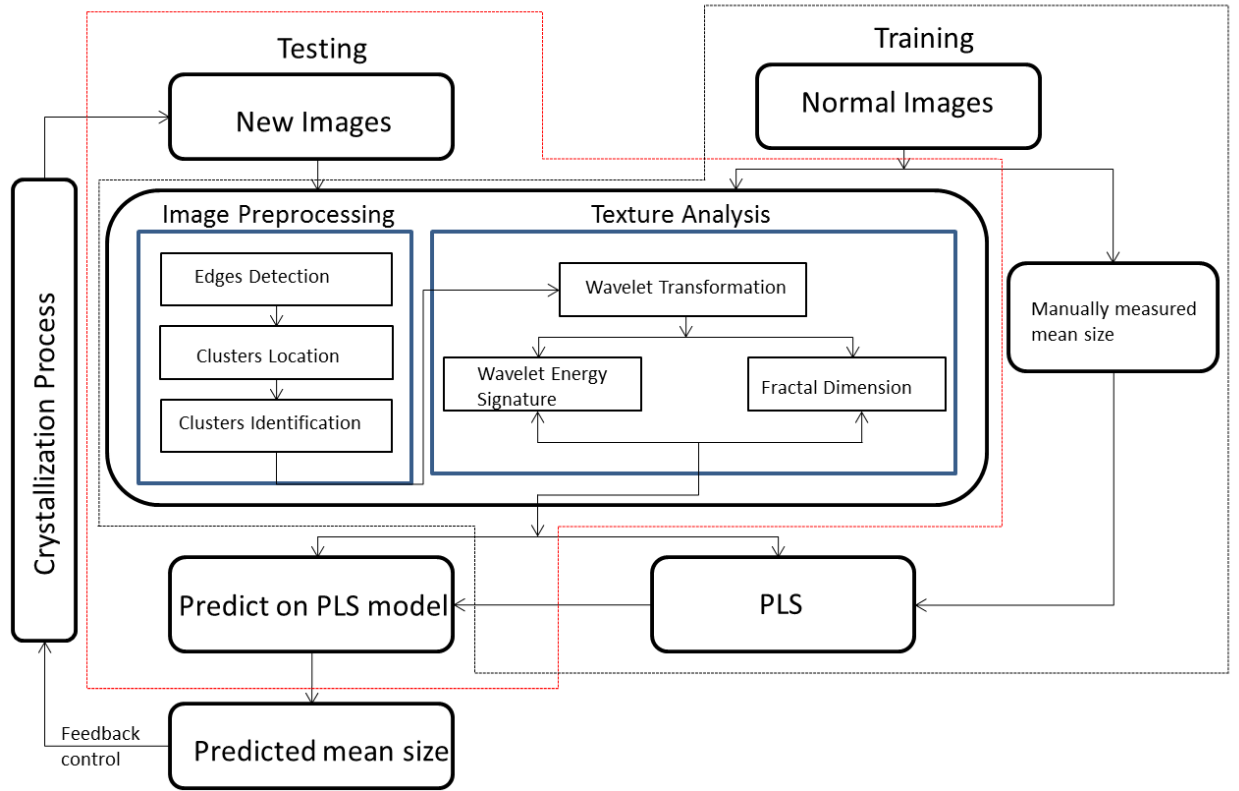


Figure 5.1: Overall architecture of mean size prediction.

5.2.1 Partial Least Squares

For two blocks of data, the predictor variables \mathbf{X} ($n \times m$) and the response variables \mathbf{Y} ($n \times l$) which has the same sample number as \mathbf{X} does, the PLS model decomposes both \mathbf{X} and \mathbf{Y} as the sum of the outer product of score vectors (t_i), or score matrix \mathbf{T} ($n \times k$), and loading

vectors (p_i or q_i), or loading matrix (\mathbf{P} ($m \times k$) or \mathbf{Q} ($l \times k$)), plus a residual matrix (\mathbf{E} or \mathbf{F}) as shown in the following equations:

$$\mathbf{X} = \sum_{i=1}^k t_i p'_i + \mathbf{E} = \mathbf{T} \mathbf{P}' + \mathbf{E} \quad (5.1)$$

$$\mathbf{Y} = \sum_{i=1}^k t_i q'_i + \mathbf{F} = \mathbf{T} \mathbf{Q}' + \mathbf{F} \quad (5.2)$$

$$\mathbf{T} = \mathbf{X} \mathbf{W} \quad (5.3)$$

where k is the number of principal components satisfying the condition that it is less than or equal to the smaller dimension of \mathbf{X} and \mathbf{Y} . \mathbf{X} and \mathbf{Y} are related by sharing the common scores which are the projections of \mathbf{X} onto a weight matrix \mathbf{W} ($m \times k$) defining the relationship between \mathbf{X} and \mathbf{Y} . \mathbf{W} is calculated through maximizing the covariance between \mathbf{X} and \mathbf{Y} and directly related to eigenvectors of $\mathbf{X}' \mathbf{Y} \mathbf{Y}' \mathbf{X}$. The score vectors \mathbf{T} are orthogonal while the weight matrix \mathbf{W} is orthonormal, that is:

$$\begin{aligned} t'_i t_j &= 0, \text{ if } i \neq j \\ w'_i w_j &= 0, \text{ if } i \neq j \text{ and } w'_i w_j = 1, \text{ if } i = j \end{aligned} \quad (5.4)$$

The loading matrix \mathbf{P} and \mathbf{Q} , on the other hand, are not orthonormal any more compared with PCA model because of the constraint in finding the common scores in the decomposition. Combining Equations (5.1), (5.2), and (5.3), a linear model is obtained as:

$$\mathbf{Y} = \mathbf{X} \mathbf{W} \mathbf{Q}' + \mathbf{F} = \mathbf{X} \mathbf{B} + \mathbf{F} \quad (5.5)$$

where, \mathbf{B} is the matrix of regression coefficients. Essentially, PLS model captures features in \mathbf{X} correlated with \mathbf{Y} in a linear regression approach and removes redundant information which does not correlate with \mathbf{Y} . Furthermore, prediction can be implemented using regression coefficients obtained from the PLS model for a new data set \mathbf{X}_n . The prediction validity, defined as how well

the predicted outcomes obtained from the PLS model fit the actual values; can be confirmed by R^2 statistics calculated from equations:

$$R^2 = 1 - \frac{RSS}{TSS}$$

$$\text{where } TSS = \sum_i (y_i - \bar{y})^2, RSS = \sum_i (y_i - y_p)^2 \quad (5.6)$$

where, \bar{y} is the average of all actual values y_i and y_p is the predicted value.

5.2.2 Application

As a continuous work of the previous chapter, models are built here using the same database (crystal images at 9 stages from the anti-solvent crystallization process with operation parameters of temperature at 30°C and anti-solvent flowrate of 1.5mL per min). Two data blocks, predictor variables **X** and response variables **Y**, need to be determined first when building a PLS model for crystal mean size prediction. In our application the texture features (wavelet energy signature and Hurst exponent/FD) were selected as the predictor variables and the crystal mean size as the response variable. In each set of sample images, the first five were used as the training data to establish the model. The predictor variables of the PLS model were stored in **X** as a [45(sample images) x 5(texture features)] matrix shown in Table 5.1, where texture features are the wavelet energy signature at decomposition level 2 to 5 and FD. The wavelet energy signature is the variance of the detail coefficients in this work. The response variable **Y** is a vector of dimension 45 x 1, where the number of rows is equal to the number of sample images per stage (5) multiplied by the number of stages (9). Each value is the manually measured mean size (calculated from the 5 images at each stage), and for each stage, the measured mean size is the same. Before performing further analysis, both **X** and **Y** were normalized as a centered and scaled version of **X** and **Y**.

It is crucial to select the optimal component number for the purpose of maximizing predictive significance in the way of capturing the most correlated variables and reducing redundancy. Several methods can be used to determine the choice of the number of components such as cross-validation, captured variance and so on. In this paper, the selection of components was based on the captured variance, which involves calculating the cumulative variance percent. Figure 5.2 shows the explained cumulative variance percent for **X** and **Y**. Since the first three components can capture 99.07% of the variance in the normalized **X**-block and 77.42% of the variance in the normalized **Y**-block, three components had been chosen for regression analysis in this application.

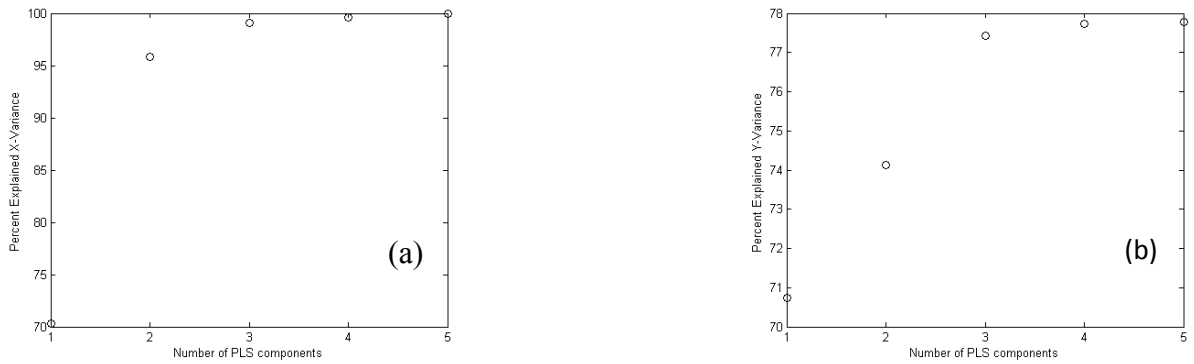


Figure 5.2: The cumulative percent of explained X- (a) and Y- (b) variance.

Implementing PLS regression on normalized **X** and **Y** with three principal components generates a series regression coefficients **B** which can be used for prediction. The prediction equation or the linear relationship of normalized **X** and **Y** in three principal component model has been truncated by deleting **F** which cannot be explained by the three components. With the help of truncated linear relationship, regression coefficients and an inverse normalization operation, the fitted response values for all 45 sample images were calculated. Fitted response

values in the same stage had been averaged and considered as the predicted mean size at that stage. Fitted response values and the predicted mean size at each stage are listed in Table 5.1.

The validity of this PLS model is illustrated by comparing predicted (from training data) and measured mean sizes at all stages. To illustrate the goodness of prediction and the reliability of this PLS model the R^2 statistics and the plot of predicted and measured value were used. For the present study a value of 93.13% was obtained. The circles in Figure 5.3 represent the scenario for the training data and how they track the diagonal line. The root-mean-square-error of calibration (RMSEC) is 5.28, while the standard error of the manually measured mean size is 19.63.

Next, the obtained PLS model was tested using new “unseen” data (data not used for model training). In this regard, the last two sample images at each crystal growth stage (not the one used previously during training) comprise the testing data. The size related information hidden in the testing data was again extracted through texture analysis following the same procedure as those used for training data and stored it in a matrix \mathbf{X}' displayed in Table 5.2. A normalization was operated on \mathbf{X}' to synchronize with the established PLS model. The prediction from testing data was calculated using the same regression coefficients \mathbf{B} and the similar linear relationship of

$$\mathbf{Y}'_n = \mathbf{X}'\mathbf{B} \quad (5.7)$$

where, is \mathbf{Y}'_n the normalized fitted response vector. Again, the inverse normalization operation was performed on \mathbf{Y}'_n to generate the fitted response values which were listed in Table 5.2. The average of the fitted response values in each stage was considered as the predicted mean size and they were also listed in Table 5.2. A R^2 statistic of 80.75% was obtained. Figure 5.3 graphically depicts the fit of the testing data. The root-mean-square-error of prediction (RMSEP) is 8.85.

Table 5.1: Texture analysis results and mean size prediction for training data.

Stage	Sample	Wavelet energy signature				Fractal Dimension	Fitted Response Values (μm)	Predicted Mean Size (μm)
		Scale 2	Scale 3	Scale 4	Scale 5			
1	Image 1	0.0042	0.0324	0.1081	0.2455	1.53	95	87
	Image 2	0.0040	0.0320	0.1239	0.2351	1.52	84	
	Image 3	0.0055	0.0406	0.1234	0.2067	1.63	68	
	Image 4	0.0027	0.0296	0.1162	0.2555	1.41	98	
	Image 5	0.0037	0.0322	0.1077	0.2192	1.53	91	
2	Image 1	0.0034	0.0324	0.1253	0.2787	1.45	94	92
	Image 2	0.0027	0.0280	0.1002	0.2230	1.46	101	
	Image 3	0.0026	0.0294	0.1140	0.2184	1.44	91	
	Image 4	0.0042	0.0389	0.1169	0.2153	1.57	77	
	Image 5	0.0033	0.0299	0.1091	0.2311	1.49	95	
3	Image 1	0.0018	0.0210	0.0921	0.2373	1.34	118	113
	Image 2	0.0019	0.0222	0.1008	0.2690	1.32	118	
	Image 3	0.0013	0.0194	0.0896	0.2166	1.28	118	
	Image 4	0.0024	0.0259	0.1036	0.2433	1.40	106	
	Image 5	0.0026	0.0297	0.1245	0.3032	1.37	103	
4	Image 1	0.0026	0.0295	0.1206	0.2886	1.38	103	116
	Image 2	0.0022	0.0251	0.1160	0.2902	1.34	111	
	Image 3	0.0017	0.0200	0.0966	0.2857	1.28	127	
	Image 4	0.0018	0.0208	0.0924	0.2536	1.33	122	
	Image 5	0.0013	0.0177	0.0907	0.2242	1.26	121	
5	Image 1	0.0010	0.0170	0.1019	0.2135	1.21	113	121
	Image 2	0.0016	0.0192	0.1005	0.3064	1.25	130	
	Image 3	0.0020	0.0247	0.1299	0.3628	1.26	119	
	Image 4	0.0022	0.0239	0.1031	0.2636	1.36	114	
	Image 5	0.0016	0.0173	0.0825	0.2357	1.31	127	
6	Image 1	0.0010	0.0145	0.0921	0.2591	1.17	131	126
	Image 2	0.0021	0.0205	0.0948	0.2627	1.35	122	
	Image 3	0.0019	0.0207	0.1015	0.2815	1.30	122	
	Image 4	0.0015	0.0189	0.0963	0.2831	1.25	128	
	Image 5	0.0015	0.0192	0.1002	0.2916	1.24	128	

(Table 5.1 continued)

(Table 5.1 continued)

Stage	Sample	Wavelet energy signature				Fractal Dimension	Fitted Response Values (μm)	Predicted Mean Size (μm)
		Scale 2	Scale 3	Scale 4	Scale 5			
7	Image 1	0.0014	0.0186	0.0818	0.2340	1.29	127	127
	Image 2	0.0011	0.0144	0.0781	0.2083	1.25	128	
	Image 3	0.0012	0.0144	0.0816	0.2283	1.24	130	
	Image 4	0.0022	0.0232	0.1129	0.3458	1.29	126	
	Image 5	0.0014	0.0169	0.0902	0.2453	1.26	126	
8	Image 1	0.0021	0.0201	0.0838	0.2602	1.35	128	130
	Image 2	0.0022	0.0228	0.0996	0.3072	1.32	126	
	Image 3	0.0011	0.0134	0.0715	0.2131	1.23	134	
	Image 4	0.0011	0.0134	0.0715	0.2131	1.23	131	
	Image 5	0.0010	0.0132	0.0732	0.2009	1.24	129	
9	Image 1	0.0012	0.0148	0.0693	0.1938	1.29	129	124
	Image 2	0.0007	0.0114	0.0778	0.2213	1.11	136	
	Image 3	0.0018	0.0201	0.0855	0.1958	1.38	114	
	Image 4	0.0023	0.0221	0.1027	0.2500	1.37	113	
	Image 5	0.0015	0.0168	0.0853	0.2538	1.28	130	

The solid line in Figure 5.3 represents the regression line for both training and testing data.

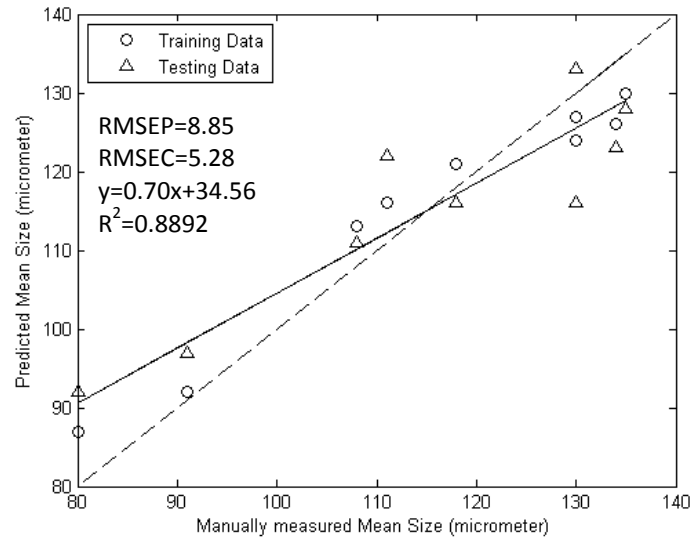


Figure 5.3: Manually measured and predicted mean size.

Table 5.2: Texture analysis results and mean size prediction for testing data.

Stage	Sample	Wavelet energy signature				Fractal Dimension	Fitted Response Values (μm)	Predicted Mean Size (μm)
		Scale 2	Scale 3	Scale 4	Scale 5			
1	Image 6	0.0028	0.0296	0.1058	0.2009	1.48	95	92
	Image 7	0.0037	0.0316	0.1104	0.2175	1.53	90	
2	Image 6	0.0028	0.0282	0.1037	0.2102	1.47	99	97
	Image 7	0.00299	0.0303	0.1145	0.2403	1.45	96	
3	Image 6	0.00189	0.0241	0.1117	0.2609	1.32	111	111
	Image 7	0.00158	0.0214	0.1098	0.2296	1.30	110	
4	Image 6	0.00185	0.0220	0.1048	0.2763	1.30	119	122
	Image 7	0.00134	0.0174	0.0907	0.2359	1.26	124	
5	Image 6	0.00160	0.0200	0.1040	0.2395	1.30	116	116
	Image 7	0.00195	0.0213	0.1046	0.2596	1.33	117	
6	Image 6	0.00170	0.0201	0.1106	0.3186	1.24	126	123
	Image 7	0.00191	0.0191	0.0894	0.2284	1.35	121	
7	Image 6	0.00111	0.0134	0.0789	0.2245	1.22	132	133
	Image 7	0.00069	0.0115	0.0766	0.2266	1.11	135	
8	Image 6	0.00177	0.0205	0.0975	0.2398	1.33	117	128
	Image 7	0.00063	0.0090	0.0596	0.1840	1.14	138	
9	Image 6	0.00264	0.0250	0.1139	0.3073	1.36	115	116
	Image 7	0.00250	0.0224	0.0941	0.2562	1.39	118	

5.3 Crystal Size Detection

Another effective and widely used technique for monitoring is multivariate statistical analysis tool, principal component analysis (PCA) which transforms a set of correlated variables into a set of uncorrelated principal components [2-6]. Because of the multivariate nature of images analysis, techniques based on multivariate statistical image analysis have been considered [7]. So far, application on crystal images is rare while applications on softwood lumber grading [8], coating uniformity assessment for tablets [9], skin quality properties prediction [10], characterizing steel surface [11], monitoring and controlling snack food processes [12] have been shown to be successful. Those papers applied the whole images at different spectra as the input

data for PCA model. However, this technique suffers from a limitation of program execution speed when used for process monitoring and control since industrial environments require high frequency feedback data. The computational cost of using a PCA model depends on the size of the data set. If an image is used as the data, the size of the image affects the computation complexity by the cubic order $O(d^3)$, where d is the number of pixels of the image [13]. Usually, a high resolution image containing more and accurate information has a large size, rendering this difficult for online application. Thus, extracting relevant features from images as the input data instead of whole images could be an efficient way to reduce data size thus executive time.

In this section, we propose a multi-resolution-multivariate-statistics based approach for crystal size monitoring. The size information is represented as the wavelet energy signatures. The multivariate statistical model runs considerably fast since the input data are the wavelet energy signatures having a smaller size of the dataset compared with a whole image. Statistical control charts with normal operation regions can be built based on images representing normal processes which generate target crystal size or size distribution. Size monitoring then is carried out by plotting the corresponding points on the statistical control charts when images representing unknown processes status are coming. Locations of the corresponding points can tell whether the process is operating within specifications (normal status) and quantitatively describe their deviations from the normal process.

5.3.1 Principal Components Analysis

PCA is a well-known orthogonal transformation that converts a set of correlated variables into a set of new variables that are linearly uncorrelated with each other. The total variability in the data set does not change after the transformation and is explained by the uncorrelated

variables called principal components (PCs). This transformation is defined in such a way that the first principal component captures the greatest amount of variance in the data set. The second one has the next greatest variance and so forth. PCA has been used as statistical process control tool for process monitoring by plotting control charts which are figures of sampled data over time in a format that renders an easy identification of in-control and out-of-control statues [14].

5.3.1.1 PCA Model

For a given data matrix \mathbf{X} (n rows of sample \times m columns of variables), PCA decomposes it as the sum of the outer product of score vectors t_i , or the score matrix \mathbf{T} ($n \times k$), and loading vectors p_i , or the loading matrix (\mathbf{P} ($m \times k$)), plus a residual matrix \mathbf{E} as shown in the following equation:

$$\mathbf{X} = \sum_{i=1}^k t_i p_i' + \mathbf{E} = \mathbf{TP}' + \mathbf{E} \quad (5.8)$$

where k is the number of principal components satisfying the condition that it is less than or equal to the smaller dimension of \mathbf{X} . The score vectors t_i are orthogonal and describe how the samples relate to each other while the loading vectors are p_i orthonormal and contain information about how variables are related to each other, that is:

$$\begin{aligned} t_i' t_j &= 0, \text{ if } i \neq j \\ p_i' p_j &= 0, \text{ if } i \neq j \text{ and } p_i' p_j = 1, \text{ if } i = j \end{aligned} \quad (5.9)$$

Usually, several PCs can explain the majority of the total variance because the correlated variables carry common information, generating some degree of redundancy among the variables in reality. There are many methods that can guide the selection of the number of PCs [15]. Among those, one can look at the variance percent explained by each PC and the cumulative

variance percent by k PCs. The calculation of the variance percent resorts to the eigenvalue of the covariance matrix of the data set \mathbf{X} . The cumulative variance percent by k PCs can be calculated in the following equation:

$$\text{Cumulative variance percent} = \frac{\sum_{j=1}^k \lambda_j}{\sum_{j=1}^m \lambda_j} \quad (5.10)$$

5.3.1.2 Multivariate Performance Monitoring

If the PCA model is constructed using historical data that represent the normal operation or desired status of the process, or in-control behavior, the current and future operational status can be referenced against the obtained PCA model. An approach for a multivariate performance monitoring strategy involves a reference region or a normal operating region (NOR) on control charts. The new status is considered normal when it locates within NOR and vice versa. The NOR is established based on normal operating data, producing a fault-free region.

For a k -dimension plot, called a PC direction chart, whose axes are k orthogonal coordinate axes generated by the PCA model if k PCs are selected, the NOR can be constructed as an ellipse. The equation is given as the following in two-dimensional data space:

$$\frac{x^2}{a^2} + \frac{y^2}{b^2} = 1 \quad (5.11)$$

where, the semi-major a and semi-minor b axis lengths are multiplications of a statistical parameter and the diagonal elements of the covariance matrix of principal components. The statistical parameter defines control limits.

Another commonly employed control charts based on the PCA model uses Q or Hotelling's T^2 statistics. The former, also known as the squared prediction error of the residuals of a new observation, is related to the difference between the new sample and its PCA

reconstruction. The Q statistic measures whether the process has shifted outside normal operation. The latter, on the other hand, measures the variation within the PCA model calculating as the distance between its PCA projection and the centroid of the normal operation data. The two statistics can be defined as followings:

$$\begin{aligned} Q_i &= e_i e_i' \\ T_i^2 &= t_i \Lambda^{-1} t_i' \end{aligned} \quad (5.12)$$

where e_i and t_i represent the residual vector and the scores of the i -th observation respectively. Λ stands for covariance matrix for normal operation data.

The determination of the NOR using Q or Hotelling's T^2 statistics depends on the control limits for these statistics. The control limit for Q statistics for a confidence level α is given by [16]:

$$\begin{aligned} Q_{lim} &= \theta_1 \left(\frac{c_\alpha h_0 \sqrt{2\theta_2}}{\theta_1} + \frac{\theta_2 h_0 (h_0 - 1)}{\theta_1^2} \right)^{\frac{1}{h_0}} \\ \theta_i &= \sum_{j=k+1}^m \lambda_j^i, \quad h_0 = 1 - \frac{2\theta_1 \theta_3}{3\theta_2^2} \end{aligned} \quad (5.13)$$

where c_α is value for standard normal distribution for confidence level α , and λ_j^i represents the i -th power of the j -th eigenvalue. As for Hotelling's T^2 statistics, the control limit for a confidence level α is [4]:

$$T_{lim}^2 = \frac{k(n-1)}{n-k} F(k, n, \alpha) \quad (5.14)$$

where $F(k, n, \alpha)$ stands for the F-distribution with k and n degrees of freedom and confidence level α . If the Q or Hotelling's T^2 statistics of a data set locates outside the control limit for a specific confidence level then an off-specification condition is detected and corrective actions will be required.

5.3.2 Methodology for Size Characterization

The essential sequence of steps for implementing the proposed methodology for automatic size detection from crystal images are given inside the dash lines in Figure 5.4. Images from an operating process condition (normal condition), representing the desired crystal size, are required first from historical data to establish a reference PCA model. Each of the images is pre-processed to retain objects and remove backgrounds. The intensities of the objects are rearranged and stored as a 1D signal vector for wavelet decomposition.

Wavelet transformation at several scales generates several details and an approximation; the details at the smallest scale and the approximation are considered as the high and low frequency noise and deleted. Wavelet energy signature for each of the remained details is calculated and used as the input variables for PCA model. The reference PCA model is built with the historical data, and generates multivariate control charts such as a PC direction chart, Q and T^2 statistics graph. An NOR in a PC direction char is needed to be defined for detection of faults. The NOR for the multivariate charts of Q or T^2 statistics is the region below confident limits in both Q and T^2 statistics. The size analysis/detection application can be carried out when a new image representing unknown size is coming. The image is under the same analysis method as the historical data. The wavelet energy signature, Q and T^2 statistics for the new observation are then calculated and plotted onto the multivariate charts to detect whether the point is inside or outside the NOR. Any points out of the NOR are then considered as out of specification condition. This methodology can be adopted for online crystal size control with the knowledge of the relationship between the production parameters and mean sizes by modifying the corresponding parameters when an off-specification condition is detected.

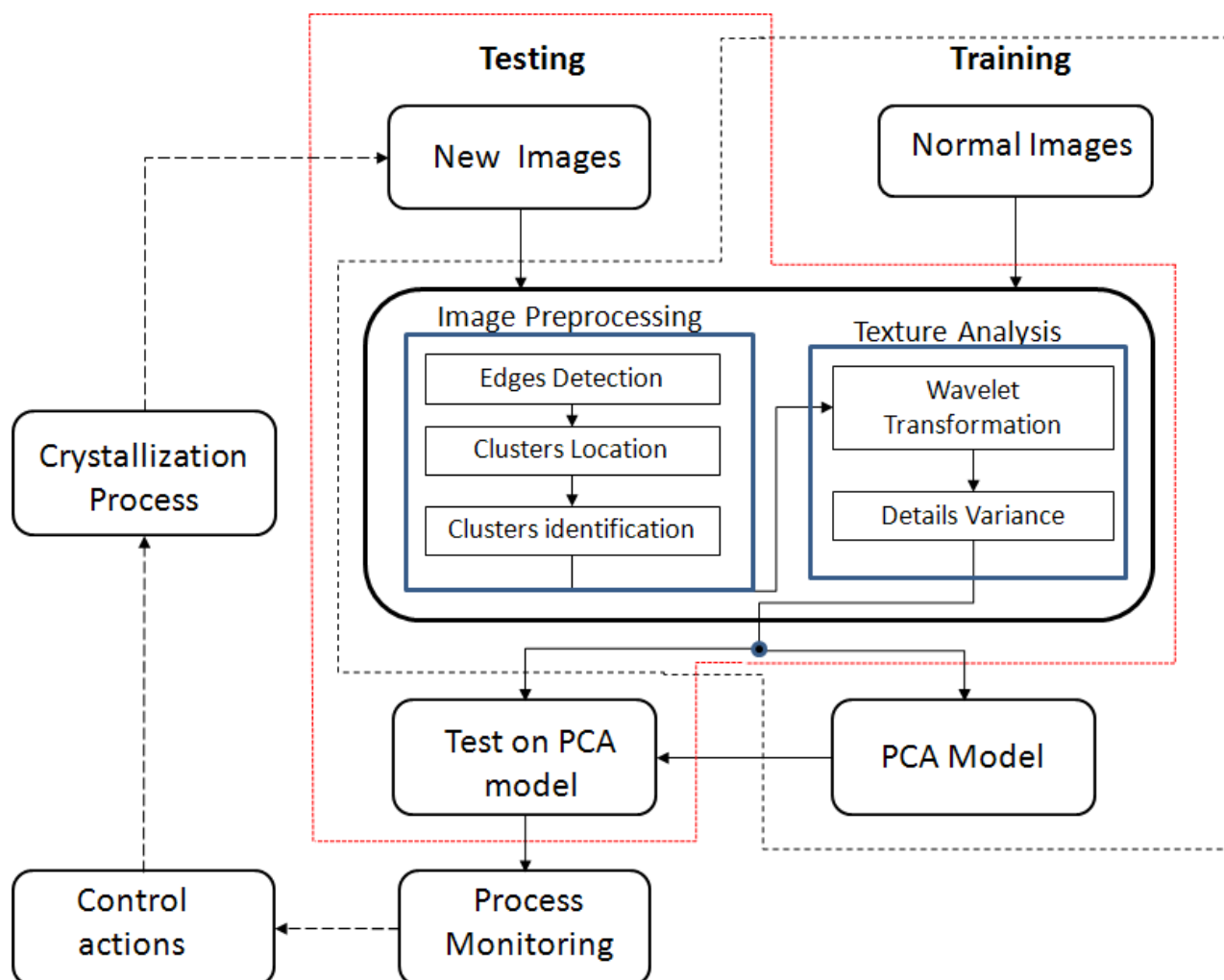


Figure 5.4: Flowchart showing the steps involved in the proposed size monitoring and control technique.

5.3.3 Case Study of Anti-Solvent Crystallization

To illustrate the methodology of using wavelet transformation and multivariate statistical analysis for mean size detection/characterization, a case study was carried out utilising the same crystal image database in Section 4. Two topics were investigated in this case study; one is the size detection with the aim to characterize crystals in desired and off-specification sizes, while the other is monitoring the entire duration of the crystallization process to investigate detecting sensitivity in deviation from desired sizes.

5.3.3.1 Crystal mean size and size distribution

The crystal mean size and crystal size distribution (CSD) were measured and plotted respectively to quantitatively characterize the crystallization process as references for building PCA models and understanding control charts. The mean size for each stage was obtained as described in Section 4.5. Figure 5.5a gives manually measured mean size during crystallization. The mean size grows fast at the first 5 stages and maintains almost stable at the last 4 stages.

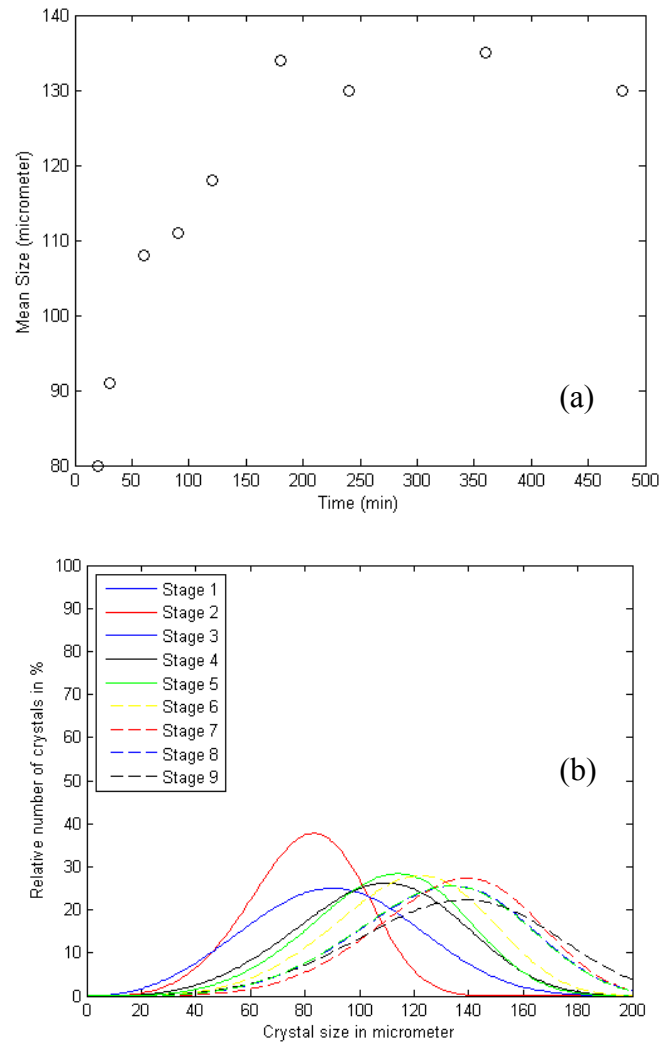


Figure 5.5: (a) Manually measured mean size during crystallization, (b) Fitted CSD for each stage.

CSD provides direct information of the distribution of the crystal length in a certain range and their normalized frequencies. The histogram of crystal lengths for each stage was plotted and fitted with Weibull density probability function. Figure 5.5b shows the fitted CSD curves for 9 stages. The peak of the fitted CSD curve goes from left to right in x-axis (from low to high in crystal size) for the first 5 stages. For the last 4 stages, it nearly doesn't change in x-axis. It is obvious that any two stages have overlapping areas in fitted CSD. The size of overlapping areas can influence the sensitivity of detecting off-specifications: the larger the overlapping area, the more similar the two statuses.

5.3.3.2 Size Detection/Characterization

In most crystal manufacturing processes, a specific mean size with narrow size distribution is demanded and crystals that are smaller or larger compared with the required mean size need to be paid more attention because large amount of those crystals could lead to the mean size deviating the specification or widen the size distribution, and their reliable detection is of relevance. A design reflecting real-life scenarios was developed in this work. It should include a desired, a negative and a positive deviation from the target statues. The selection of statues was based on mean size and CSD (Figure 5.5). Since the aim of this part is checking whether a PCA model can detect size, statues have distinct differences, such as large mean size differences and small overlapping area in CSD, are chosen. Crystal mean size at Stage 4 is selected as the desired value, and those at Stages 1 (smaller) and 9 (larger) were considered off-specification. Images from Stage 4, as historical data, represent the normal status of the process and consequently they were adopted to build a PCA model, which was then used as the reference model when testing images from Stages 1 and 9 (considered as new arrivals since they didn't involve in establishing

the PCA model). Image analysis was performed before PCA model establishment and the root of wavelet energy signature for each detail of the 15 crystal images were provided in Table 5.2.

The PCA model was established with the wavelet feature matrix \mathbf{X} ($n \times m$) whose components are listed in Table 5.2 at Stage 4. The size of the matrix decides the computational cost at $O(d^3)$, where $d = 5 \times 4$. The execution time can be substantially reduced compared when using the original images. In this work, it takes 6.4 seconds to build the PCA model including calculation of the wavelet features.

The data \mathbf{X} was then auto-scaled through dividing each column by its standard deviation. Using the cumulative variance percent it was found that the first two PCs concentrate 96.73% of the overall variation in the auto-scaled \mathbf{X} and thus the first two principal components were selected for further analysis and the multivariate monitoring charts can be established. Figure 5.6 illustrates the first two PCs plot. The blue plus signs represent normal operational conditions. The ellipse shown in Figure 5.6 is defined as the normal operation region (NOR) around the good data, when a 90% confidence level is used.

The future process status estimation can be carried out by calculating and plotting corresponding points of new arrival data onto the multivariate chart. Two sets of observations, images from Stages 1 and 9, are used for this purpose. Following the scaling of the matrix of wavelet energy signature of the new observations, PCA projection model provides new scores and presents them in Figure 5.6, where green circles are scenarios for Stage1 and black stars are for Stage 9. It is distinctively to see that the locations of the scores for the new arrivals are outside the NOR ellipse, indicating that the new arrivals stem from abnormal production process. Another piece of information in this multivariate chart is that the off-specification conditions show well defined patterns. The points representing large sizes lie left to the NOR ellipse, and

those for small size are right above. The orientations for the new arrivals indicate the size deviation direction such as position or negative. Pattern recognition and classification techniques could then be used to guide the process towards the desired target by implementing proper control actions.

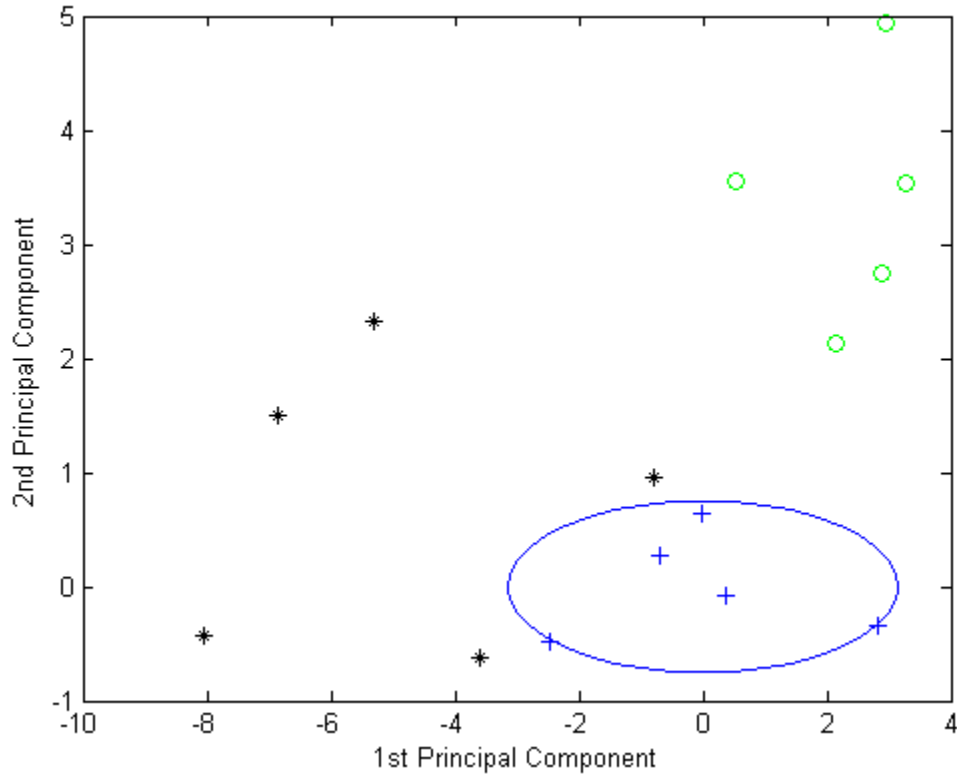


Figure 5.6: Multivariate control chart on the first two principal components. Blue (plus), green (circle) and black (star) represent medium (desired), small and large size respectively

Similar type of information can be obtained through the Q and Hotelling's T^2 statistics. The upper boundary of Q and Hotelling's T^2 statistics based on the PCA model with confidence level of 90% are 0.3209 and 17.48. Q and Hotelling's T^2 statistics for the new observations have been calculated and plotted in the multivariate control chart (Figure 5.7), in which the NOR is defined as the area below limits. Since they all located outside the NOR, they should be perceived as off-specifications. Examining the chart in detail, it shows that all of the new

observations, no matter how small or large they are, their Q values are always over Q_{limit} , but only some have greater value in Hotelling's T^2 statistics. This implies that Q measure is more sensitive to such changes compared to Hotelling's T^2 .

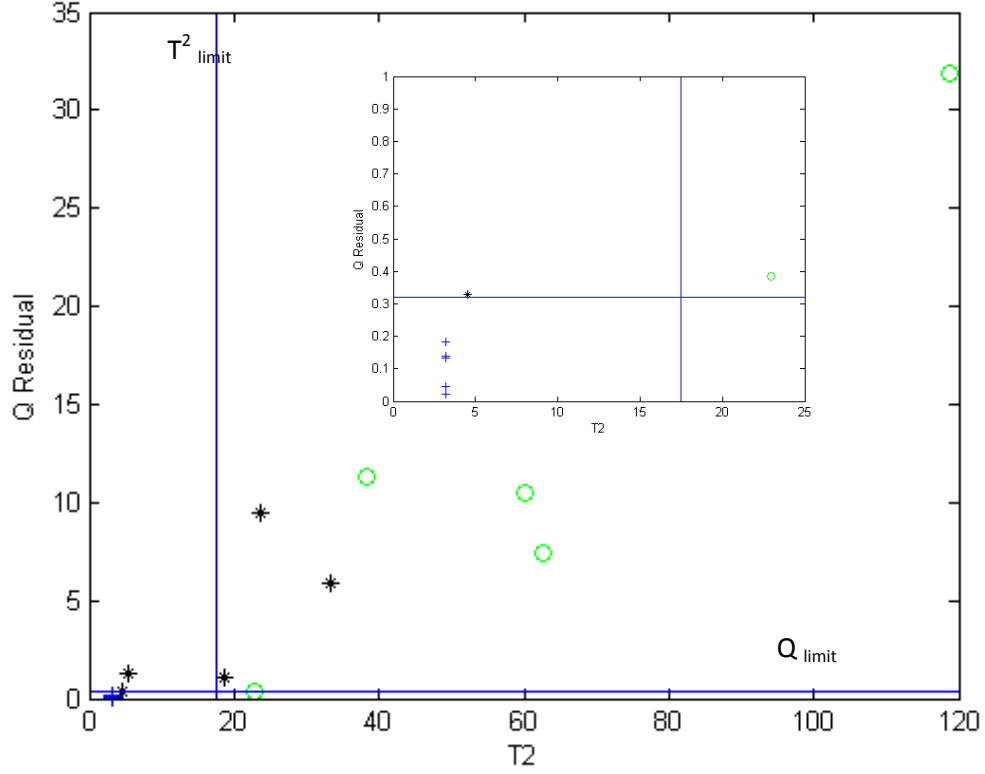


Figure 5.7: Multivariate control chart on Q and T^2 statistics. Blue plus, green circle and black star represent medium (desired), small and large size respectively. The inset enlarges the bottom left corner of the multivariate control chart for better visibility.

5.3.2.3 Deviated Sensitivity Investigation

As previously discussing about CSD, larger overlapping areas lead to fewer differences between two process statuses. It is interesting to investigate whether the proposed approach can detect off-specifications at different deviation level among statues. An analysis was performed using the proposed image-based strategy to monitor the whole batch during the crystallization run. The mean size gradually becomes larger first and then almost stable during crystallization. The overlapping level in CSD with the initial stage becomes lower as crystals grow. Sample

images from each stage are shown in Figure 5.8. A monitoring tool box with a simple user interface was built in Matlab allowing automatic processing/characterization of all images as the crystallization proceeds.

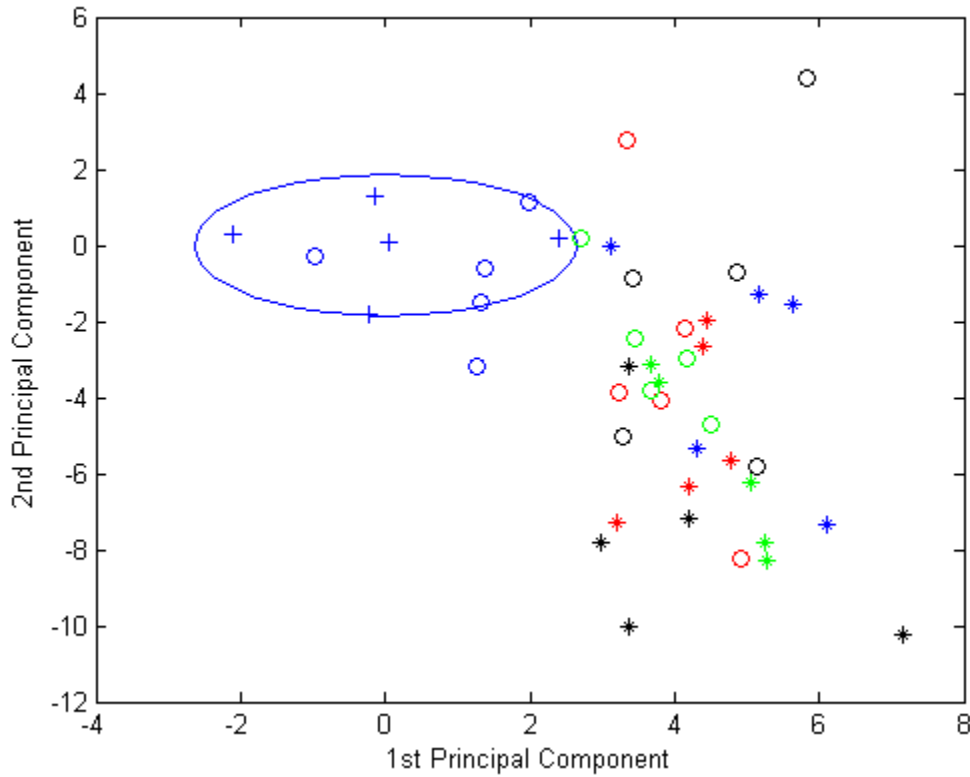


Figure 5.8: PC1 vs PC2 during growth stages. Stage 1 to 9 is blue (plus), blue (circle), red (circle), green (circle), black (circle), blue (star), red (star), green (star) and black (star) respectively.

In this case, images corresponding to the initial stage (initial nucleation) are considered for building the PCA model since this stage can catch all the deviation levels. Subsequent images, corresponding to different sampling times were then plotted into the multivariate charts for monitoring the growth. The first two PCs captures 96.65% information of all the variables in this PCA model. The definition of the normal region with 90% confidence and the statistical control limits is shown in Figure 5.8. 4 out of 5 points represent Stage 2 are located inside the confidence

ellipse. It makes sense because Stage 2 has the largest overlapping area with Stage 1 compared with other stages. For other stages, the algorithm can identify deviations in the PC control chart although some points are close to the confidence ellipse.

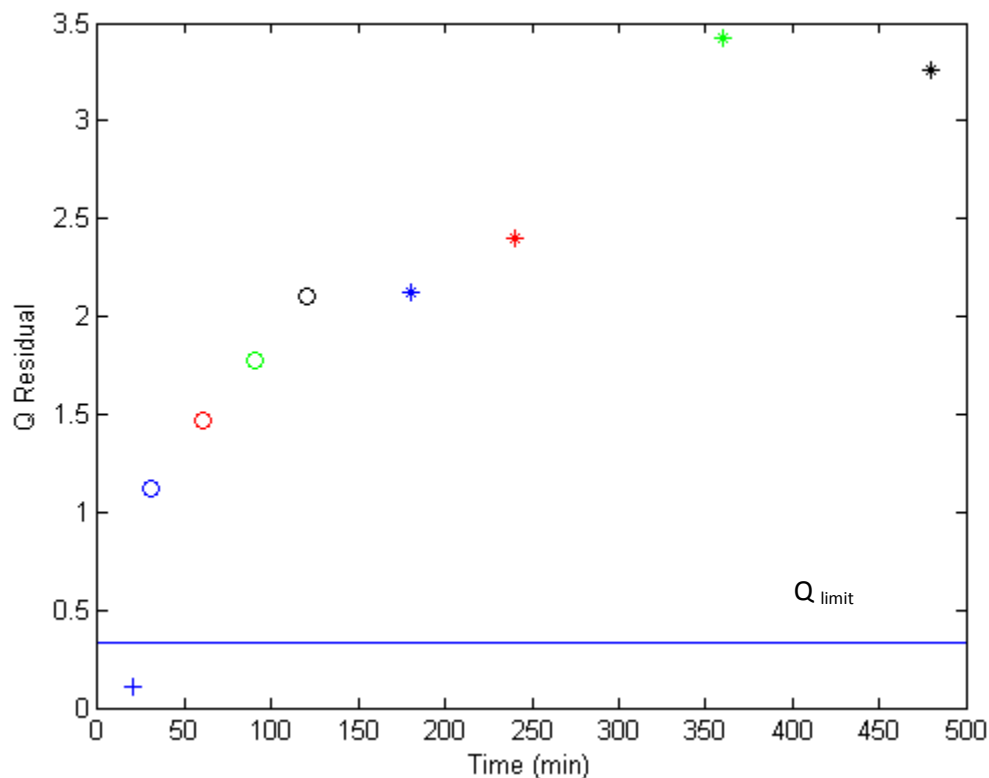


Figure 5.9: Multivariate control chart Q during growth monitoring test. The signs have the same meaning as in Figure 5.8.

Figure 5.9, illustrates the performance of the monitoring tool as the crystallization proceeds towards the end of the batch. In this case images are continuously processed (averages among the processed images at each sampling stage are given) as they become available. The upper boundary of Q statistics with confidence level of 90% is 0.3373. Colours indicate the different stages during the crystal growth. Any stage deviates the initial one can be detected since its corresponding average Q statistics is above the control limits. An exciting finding is that Q statistics increases as crystallization time goes by, which is the similar phenomena of crystal

mean size as in Figure 5.5a. Table 5.3 gives the crystal mean size and Q statistics for each stage. The application of this finding is to quantitatively describe the deviation extent to the target operation status (size and CSD). It can also be used as a feature to characterize crystallization. We can clearly appreciate that the proposed approach is able to capture the crystal growth thus providing a rather simple monitoring tool for his type of operation.

Table 5.3: Crystal mean size and Q statistics for each stage.

Stage	1	2	3	4	5	6	7	8	9
Mean size (micrometer)	80	96	108	111	118	134	130	136	132
Q statistics	0.11	1.12	1.47	1.77	2.10	2.12	2.40	3.42	3.26

5.4 Conclusions

Multi-resolution multivariate approaches to predict and characterize crystal size in anti-solvent crystallization operation have been proposed. The approach incorporates advanced image pre-processing techniques with texture analysis and multivariate statistical analysis tools in a unique way to solve a rather complex characterization problem. The linear relationship of FD and crystal mean size had been extracted and built as a PLS model for predicting crystal mean size. PCA models were developed to detect size differences and deviations during crystal growth. Overall the models provide promising tool for on-line monitoring and controlling a crystal production process.

5.5 References

- [1] G. A. Argaw, M. J. Alport, S. B. Malinga, Automatic measurement of crystal size distribution using image processing, South African Sugar Technologists Association, (2006) 399-411.
- [2] P. Facco, F. Bezzo, M. Barolo, R. Mukherjee, J. A. Romagnoli, Monitoring roughness and edge shape on semiconductors through multiresolution and multivariate image analysis, AIChE Journal, 55 (2009) 1147-1160.

- [3] K. S. Kim, J. W. Ko, Real-time risk monitoring system for chemical plants, *Korean Journal of Chemical Engineering*, 22 (2005) 26-31.
- [4] M. S. Reis, A. Bauer, Wavelet texture analysis of on-line acquired images for paper formation assessment and monitoring, *Chemometrics and Intelligent Laboratory Systems*, 95 (2009) 129-137.
- [5] A. AlGhazzawi, B. Lennox, Monitoring a complex refining process using multivariate statistics, *Control Engineering Practice*, 16 (2008) 294-307.
- [6] P. Ralston, G. DePuy, J.H. Graham, Graphical enhancement to support PCA-based process monitoring and fault diagnosis, *ISA Transaction*, 43 (2004) 639-653.
- [7] M. H. Bharati, J. F. MacGregor, Multivariate image analysis for real-time process monitoring and control, *Industrial & Engineering Chemistry Research*, 37 (1998) 4715-4724.
- [8] M. H. Bharati, J. F. MacGregor, W. Tropper, Softwood lumber grading through on-line multivariate image analysis techniques, *Industrial & Engineering Chemistry Research*, 42 (2003) 5345-5353.
- [9] S. Garcia-Munoz, D. S. Gierer, Coating uniformity assessment for colored immediate release tablets using multivariate image analysis, *International Journal of Pharmaceutics*, 395 (2010) 104-113.
- [10] J. M. Prats-Montalban, A. Ferrer, R. Bro, T. Hanciewicz, Prediction of skin quality properties by different multivariate image analysis methodologies, *Chemometrics and Intelligent Laboratory Systems*, 96 (2009) 6-13.
- [11] M. H. Bharati, J. F. MacGregor, Texture analysis of images using principal component analysis, *Proceedings of SPIE*, 4188 (2001) 27-37.
- [12] H. L. Yu, J. F. MacGregor, G. Haarsma, W. Bourg, Digital imaging for online monitoring and control of industrial snack food processes, *Industrial & Engineering Chemistry Research*, 42 (2003) 3036-3044.
- [13] G. C. Feng, P. C. Yuen, D. Q. Dai, Human face recognition using PCA on wavelet subband, *Journal of Electronic Imaging*, 9 (2000) 226-233.
- [14] J. A. Romagnoli, A. Palazoglu, *Introduction to process control*, CRC Press, Boca Raton, 2006.
- [15] S. Valle, W. H. Li, S. J. Qin, Selection of the number of principal components: The variance of the reconstruction error criterion with a comparison to other methods, *Industrial & Engineering Chemistry Research*, 38 (1999) 4389-4401.
- [16] L. H. Chiang, E. L. Russell, R. D. Braatz, Fault diagnosis in chemical processes using Fisher discriminant analysis, discriminant partial least squares, and principal component analysis, *Chemometrics and Intelligent Laboratory Systems*, 50 (2000) 243-252.

CHAPTER 6. IMAGE-BASED MULTI-RESOLUTION-ANN APPROACH FOR ON-LINE PARTICLE SIZE CHARACTERIZATION

6.1 Introduction

The linear PLS model built in Section 5 shows the powerful predictability based on crystal images from a single anti-solvent crystallization. However, the limitation of the linear model design is that a nominal model may not have the capability of predicting the nonlinear processes in the whole operation range. Therefore, the linear models may not be effective when the operation strays away from the nominal operation condition. Models that can capture the dynamic behaviour of a nonlinear process within the whole operating regime attract attentions. This section takes the challenge of developing a globe model for complex nonlinear systems.

The PCA model in Section 5 can work effectively to maintain normal manufacturing by detecting particle mean size deviation giving the condition that the size distribution keeps at the same/similar width. Therefore besides mean size, the size distribution needs to be investigated to fully understand, monitor and control particulate systems.

In this section an image-based multi-resolution sensor for online prediction of crystal size distribution (CSD) is proposed. The mean and standard deviation of lognormal probability density function as the CSD can be predicted through the on-line sensor. In the proposed approach, texture analysis (fractal dimension (FD) and energy signatures) as characteristic parameters to follow the crystal growth is utilized. The methodology consists of a combination of thresholding and wavelet-texture algorithms. The thresholding method is used to identify crystal clusters and substrate empty backgrounds. Wavelet-fractal and energy signatures are performed afterwards to estimate texture on crystal clusters. Following the texture information extraction, a nonlinear mapping consisting of an artificial neural network (ANN) is incorporated using as inputs the texture information in conjunction with the available on-line process

conditions (flowrate and temperature). The output data for training the ANN models, i.e. the mean and standard deviation of the crystal size distribution, are measured manually at different sampling times as well as in a range of operating conditions.

A fully automated laboratory scale software/hardware framework was setup for image acquisition and processing. It includes a system with a flow cell and a pump (through which samples are continuously circulated), an illumination system for lighting up the imaged region of the flow cell, an optical zoom system for providing magnification and a high speed camera for continuous image capture. A software framework developed in MATLAB enables the configuration of the image acquisition parameters as well as the processing of the on-line images. Validations against experimental data are presented for the NaCl-water-ethanol anti-solvent crystallization system.

The section is organized as follows: The algorithm ANN is first introduced in detail in Sections 6.2. In Section 6.3, we illustrate the proposed methodology. A case study is described in Section 6.4, including the operation regime of crystallization in Section 6.4.1, the results and discussion of fractal dimension from crystal images obtained during crystal growth process at different crystallization operation conditions in Section 6.4.2 and the development of predictive models for CSD estimation in Section 6.4.3. Finally, conclusions are presented in the last section.

6.2 Artificial Neural Network

The human brain is a system able to elaborate a great number of high complexity information. Its cellular units, the neurons, can receive, integer and transmit nervous impulses in order to develop some functions such as pattern recognition, perception and movement control.

This happens in a time really lower than the fastest computers currently existing. Since this, inspired by the biological nervous system, Artificial Neural Networks (ANNs) have been explored as mathematical models to process information. As one of the most active research sector, ANNs have been successfully applied in fields such as industrial, medical, data mining, pattern recognition, classification, signal processing, clustering, financial and many others. This is due to the strong ability of ANNs in capturing complex input/output relationships. The network is composed by a number of nodes or units connected to the inputs and to the outputs. The signals pass throw the connections and are scaled using appropriate weights that are updated following an error-correction rule in order to adapt the network to new situations and aims. So, according to the brain behavior, the network operates by a learning process [1, 2].

A neural network can be seen as a continuous-time nonlinear parallel dynamic system that processes information by a connectionist approach [3]. Such connectionism is realized through the massive interconnection of artificial neurons which are processing elements.

According to the signal transmission manner, neural network models can be divided into feed-forward and recurrent neural networks for different fields of applications.

In our work, two feed-forward neural networks (FNNs) are developed to predict the variance and the mean size of crystals using as inputs among others, the fractal and the wavelet energy obtained by image analysis. FNNs are also known as multilayer networks having a layered architecture. Figure 6.1 gives a topology structure of a three layers network which is also the architecture that our case adopted: an input layer \mathbf{x} consisting of sensory neurons, a hidden layer of computational neurons and an output layer \mathbf{y} of target neurons. The hidden layer \mathbf{a} is connected with the input layer through a transfer function with weights $\mathbf{W1}$ and biases $\mathbf{b1}$, as:

$$\mathbf{a} = f(\mathbf{W1x} + \mathbf{b1}) \quad (6.1)$$

The output layer has the similar connection to the hidden layer:

$$\mathbf{y} = \varphi(\mathbf{W2a} + \mathbf{b2}) \quad (6.2)$$

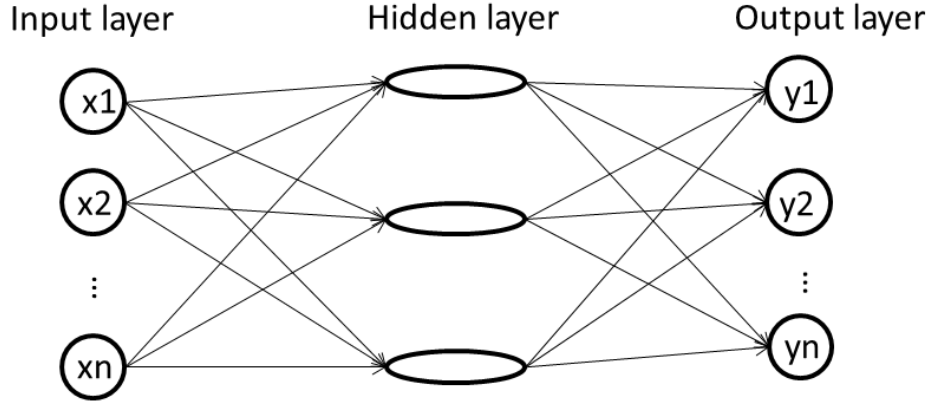


Figure 6.1: A topology structure of three-layer FNN

Nonlinear transfer functions between layers allow the network to capture the nonlinear relationships between input and output. In our case, the input layer and hidden layer take Tan-Sigmoid transfer function and linear transfer function is used between the hidden layer and output layer. The algorithm of the tan-sigmoidal function is:

$$a = \frac{2}{1 + \exp(-2x)} - 1 \quad (6.3)$$

And the algorithm of the linear function is:

$$y = a \quad (6.4)$$

FNN is a supervised learning method with the error back-propagation algorithm. The behavior of FNNs can be classified into a learning phase and updating the connectionist architectures. The input information is processed through the network in a forward direction on a layer-by-layer basis with fixed weights and biases. Then the network adjusts itself by updating

the weights and biases after the error signal is propagated backward to process information meaningfully.

Training FNN models can be started by firstly normalizing the database including both inputs \mathbf{x} and targets \mathbf{t} into -1 to 1 to improve the training efficiency. The outputs can be reversely transformed into the units of the original target data. The data were normalized through the following function:

$$zn = 2 \frac{z - z_{min}}{z_{max} - z_{min}} - 1 \quad (6.5)$$

Where z is a specific element of the original input/target data, z_{min} and z_{max} represent the minimum and maximum values of each row of the input/target matrix, and zn is the corresponding normalized value.

Training the net can be started by first randomly initializing the weights and biases. The network performance here is defined as the mean square error (MSE) between the network outputs and the targets, as:

$$MSE = \frac{\sum \mathbf{e}^2}{n} = \frac{\sum (\mathbf{t} - \mathbf{y})^2}{n} \quad (6.6)$$

where, \mathbf{e} is a vector of the network errors and n is the total number of targets.

The training process is actually iterations of minimizing the MSE with respect to weights and biases with the steepest descent algorithm. That is updating weights and biases in the direction in which the performance function decreases most quickly (the negative of the gradient). Levenberg-Marquardt algorithm with a large value of scale μ is a method to approximate the steepest descent algorithm and is used in this work.

$$\boldsymbol{\delta} = [\mathbf{J}^T \mathbf{J} + \mu \mathbf{I}]^{-1} \mathbf{J}^T \mathbf{e} \quad (6.7)$$

where, δ is the adjusted weights/biases, I is the identity matrix, and J is the Jacobian matrix of errors over weights and biases.

6.3 Methodology of Image-Based Multi-Resolution Sensor

The overall architecture of online crystal size distribution prediction by Image-Based Multi Resolution Sensor is given in Figure 6.2. The crystallization can be carried out in a reactor with suitable volume and designs that allow temperature detection, anti-solvent addition and crystal suspension circulation. To maintain desired crystallization manufacturing parameters, temperature and anti-solvent addition speed in this case, control instruments such as feed pump or equipment with control function are welcomed. Crystal suspension circulates through a cell at which the crystal images are taken by a camera connecting to a microscope and a computer. The images will be stored in a database in the computer and gone through image analysis. The essential and sequence of steps for implementing the proposed methodology for CSD prediction from crystal images are shown in rectangular boxes in Figure 6.2. The sensor needs a prerequisite ANN which can be built at several crystallization conditions with corresponding images. An input image is treated as a 2D array of pixel intensities. A thresholding algorithm is applied for extracting features of interest which are the crystal clusters in this work. This is accomplished through a series of three sub-steps: a) detection of crystal edges by a threshold value differentiating them from the background, b) detection of the locations of the crystal clusters with the help of x-y coordinates on the binary image of crystal clusters, and c) determining and extracting the intensity values belonging to the crystal clusters. The information data of the clusters is then restored into a vector, being processed to generate the texture features by means of wavelet-fractal-energy algorithm. In this regard, it is first decomposed by wavelet

transformation at several levels into details and an approximation. The detail from lower decomposition level and the approximation are considered as the high and low frequency noise to be removed. The remained details are then used for finding their variance and 2-based logarithm of the variance. The 2-based logarithm of the variance at each scale and decomposition scales are then plotted and fitted by a line whose slope is used to calculate the Hurst exponent and consequently the FD. The texture features as well as crystallization parameters can be used for further application such as establishing ANN for the prediction of crystal mean size or standard deviation. When a new image is coming to the ANN, it goes through the same texture analysis procedures and generates the same variables as in the existed ANN. Then the ANN can predict the mean and standard deviation.

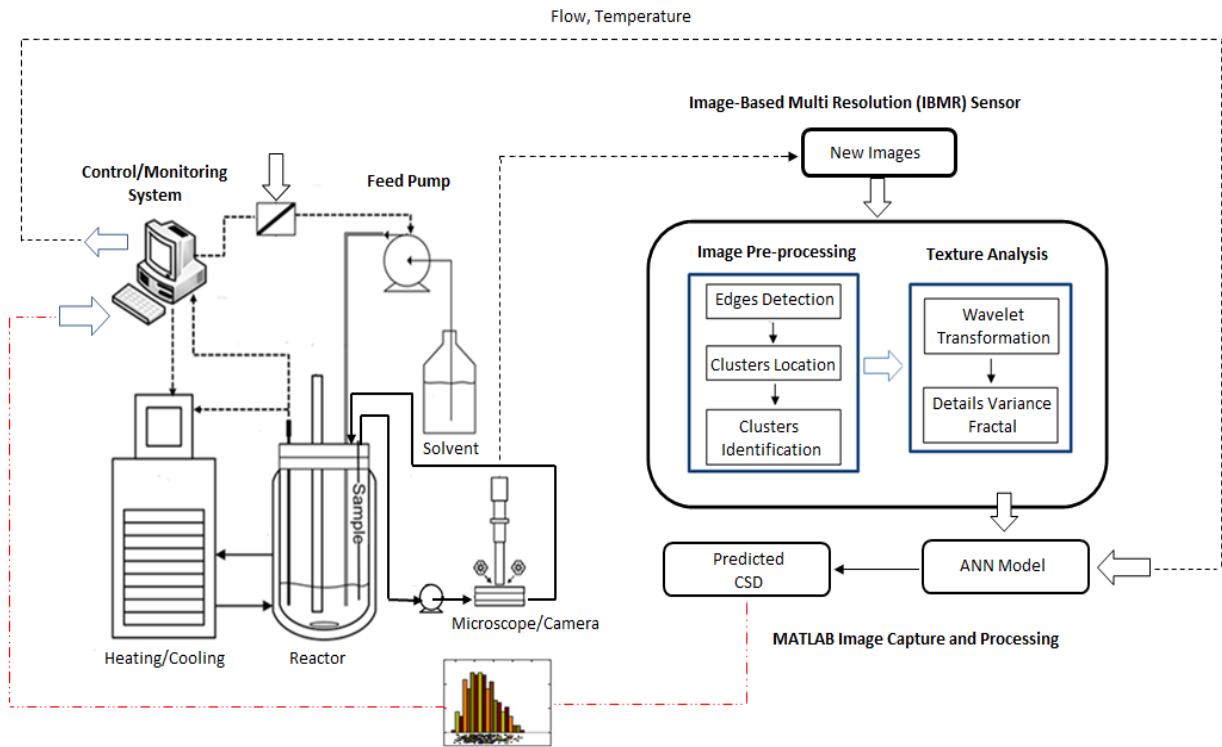


Figure 6.2:Overall architecture of CSD prediction

6.4 Case Study

Following the same ideas as discussed in Chapter 2, a laboratory scale software/hardware framework for capturing crystal images for this case study was setup at LSU Process Systems laboratory, shown in Figure 6.3a. The main difference, with the previous set-up is that in this case the image acquisition is done completely automated on-line during the experimental batch at predefined sampling times. The cylindrical crystallizer (Figure 6.3b) is connected to a heating/cooling bath (Figure 6.3c). The measurement of the solution temperature is achieved through a Resistance Temperature Detector probe which is wired up to the temperature control system. The antisolvent is added by a peristaltic pump whose speed is controlled by a computer control system (Figure 6.3d). The device for online images capturing is a flow cell made in polycarbonate, slide-like shaped, through which the suspension can be circulated from the reactor by another peristaltic pump. An optical microscope, which is connected to a camera, is used to help to provide crystal images at appropriate magnifications. The online image sampling setup is given in Figure 6.3e.

6.4.1 Experiment

A set of anti-solvent crystallization experiments at both constant and changed conditions was carried out with anti-solvent flow rate and temperature as the process parameters. For constant conditions, three different values were chosen: 0.7 [ml/min], 1.5 [ml/min], 3 [ml/min] as flow rate and 10°C, 20°C, 30°C as temperature. For the changed conditions, the temperature and flowrate were changed according to Figure 6.4 respectively. At the startup conditions, the crystallizer was filled with the saline solution composed of 100 g of water and 34 g of NaCl. The solvent solution was made up of 95% of ethanol and was added by the time to the initial solution

using a peristaltic pump. The solution whose temperature was controlled by the heating/cooling system was continuously stirred. As for the crystals growth examination, the suspension was circulated into the flow cell in an online fashion.

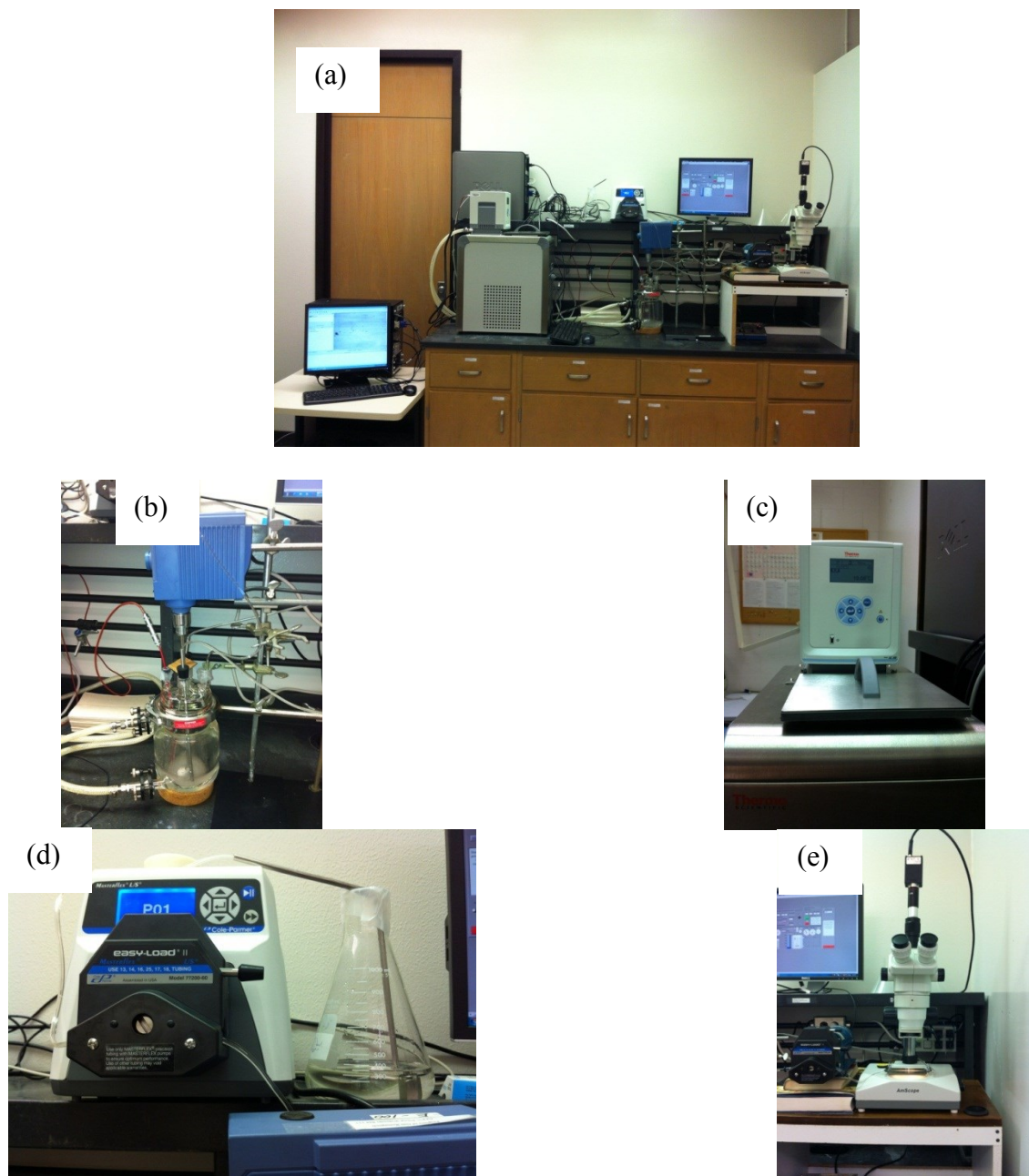


Figure 6.3:(a) Image acquisition setup at LSU, (b) Crystallizer, (c) Thermostatic bath, (d) Peristaltic pump with the antisolvent reservoir, (e) Online sampling device with the optical microscope and the peristaltic pump.

6.4.2 Image Acquisition System

The experimental setting utilizes a mono USB microscope camera (model A631f) with a resolution of 1392 x 1040 pixels, which fits into the side tube on the side of the microscope with one of the supplied adapters and connects to a computer. The Basler Pylon software is utilized to capture images with a resolution of 1280 x 960 pixels, which are imported into AMSCOPE[®] for manual measurement (individual particle analysis). The conversion factor of microns to pixel is 0.42 as the magnification was used to manually measure individual crystal sizes on each image. Images were taken at different crystallization stages which were listed in Table 6.1 for each experiment condition. At each crystal growth stage, a set of at least 10 images capturing different amount of crystals were utilized.

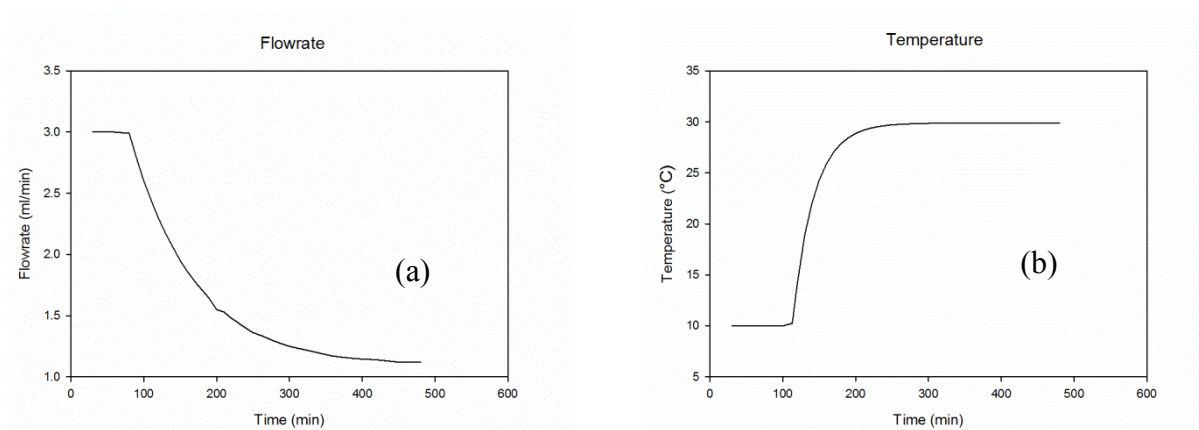


Figure 6.4: The curves for changed flowrate (a) and temperature (b) versus crystallization time

6.4.3 The Relationship between FD and Crystal Growth at Different Process Conditions

This section focuses on investigating the relationship between the FD and the growth of crystals with the sets of images from crystal growth stages during the nine constant conditions of antisolvent crystallization batches. The methodology for FD determination was applied on each image. The mean FD for each stage was the average value obtained from the set of images for

that stage. An inverse second order polynomial model was used to simulate the trend of the mean FD for each crystallization condition.

Table 6.1: Database from different crystallization conditions and stages

Condition		Crystallization stage (min)
Temperature (°C)	Anti-solvent flowrate (mL/min)	
10	0.7	30, 60, 90, 120, 180, 240, 300, 360, 420, 480
10	1.5	30, 60, 90, 120, 180, 240, 300, 360, 420, 480
10	3.0	10, 15, 20, 30, 60, 90, 120, 180, 240, 300
20	0.7	30, 60, 90, 120, 180, 240, 300, 360, 420, 480
20	1.5	30, 60, 90, 120, 180, 240, 300, 360, 420, 480
20	3.0	10, 15, 20, 30, 60, 90, 120, 180, 240, 300
30	0.7	30, 60, 90, 120, 180, 240, 300, 360, 420, 480
30	1.5	30, 60, 90, 120, 180, 240, 300, 360, 420, 480
30	3.0	10, 15, 20, 30, 60, 90, 120, 180, 240, 300
changed	changed	20, 30, 60, 90, 120, 180, 240, 300, 360, 420, 480

Charts for manually measured mean size and the simulated FD for each stage are plotted as well in Figure 6.5 and 6.6, distinctly displaying their tendency over time. During each crystallization process, the measured mean size increase sharply at the beginning and then increase gradually until they reach relatively constant values. The simulated FD decreased quickly as time goes by to reach another relatively constant value. Comparing the mean size for all the crystallizations (Figure 6.4), it is found that high flowrate can make crystals grow not as much as at low flowrate if the temperature is the same; and crystals don't grow very much at low

temperatures if the flowrate is the same. Figure 6.5 shows higher flowrate can generate higher FD at the end of crystallization with the same temperature. While Figure tells that higher FD can come from crystallization at the condition of lower temperature with the same flowrate. As expected, the Figure 6.5 and 6.6 illustrate that simulated FD follows an inverse changing pattern to manually measured mean size.

6.4.4 ANN Models and Prediction

6.4.4.1 ANN Model

The topology structure of BP ANN was designed to be three-layer networks, which including several input neurons/variables and one output/target neuron which is the manually measured mean size or standard deviation. The gradient and the number of validation checks are the training termination criteria. In the case study, $1e-5$ and 6 were set. If the gradient becomes less than $1e-5$, the training process will stop. If the check number goes up to 6, the training will stop as well. The optimum weights and biases for a good network performance can then be obtained.

Images from the constant conditions comprise of the training set for the ANN model while those from the changed conditions are the testing set. For images coming at the same stage from a specific condition, the corresponding outputs, shared the same value. The predicted size for each stage from a specific condition was the average of generated values by the ANN model for corresponding images.

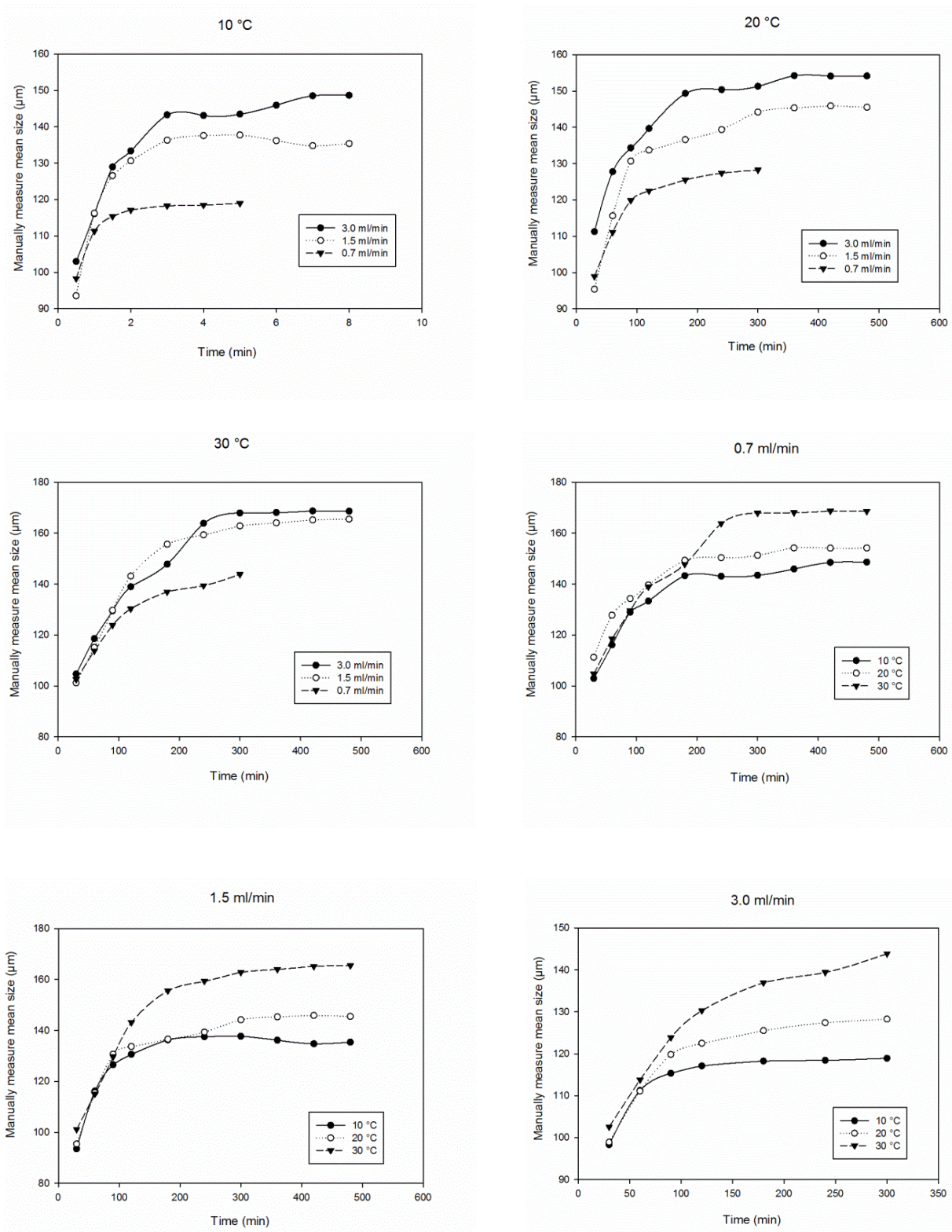


Figure 6.5. Manually measured mean size at different crystallization conditions.

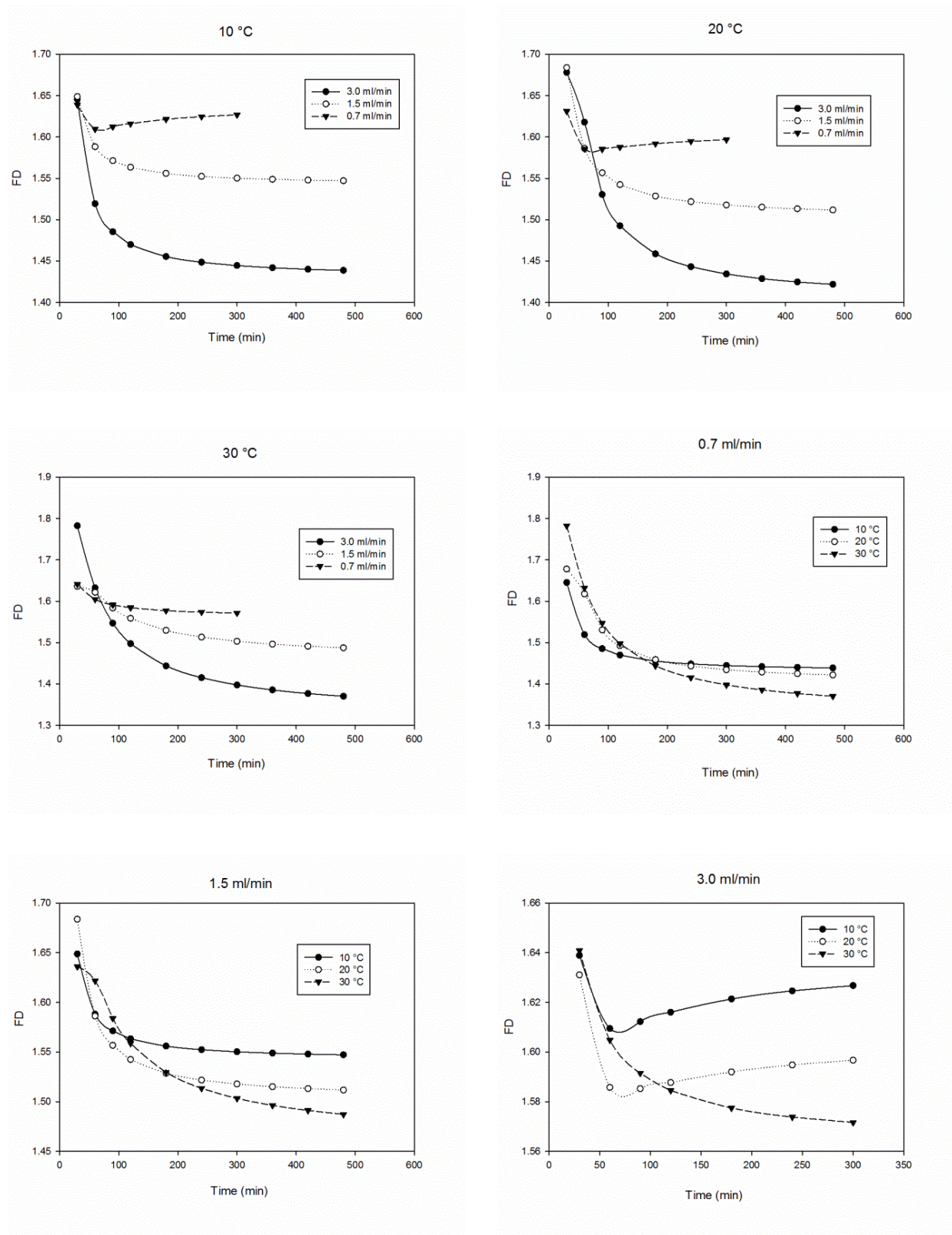


Figure 6.6. Estimated FD at different crystallization conditions

The prediction validity, defined as how well the predicted outcomes obtained from the ANN model fit the experimental values, can be confirmed by the root mean square error (*RMSE*), R^2 statistics and sum of squared residuals (*SSR*) between *exp*, short for experimental, and *pred*, short for predicted values, as:

$$RMSE = \sqrt{\frac{\sum (exp - pred)^2}{n}} \quad (6.8)$$

$$R^2 = 1 - \frac{\sum (exp - avg)^2}{\sum (exp - pred)^2} \quad (6.9)$$

$$SSR = \sum (exp - pred)^2 \quad (6.10)$$

6.4.4.2 Prediction of Mean Size and Standard Deviation by ANN

Four ANN models were built to predict the mean size and standard deviation respectively. Standard deviation from the best global model using nonlinear Fokker-Planck Equation [4] were adopt as the targets for the latter. The available inputs include temperature, flowrate, sampling time, wavelet energy signature at decomposition level 3 to 6, fractal dimension. To investigate the influence of the number of inputs, models built were classified into two classes: ANNs with and without sampling time. The manually measured mean size was used as the outputs for the former. The statistical characterizations of the size prediction for training and testing sets are listed in Table 6.2 and 6.3. Figure 6.7 provides the comparison between manually measured mean size and the predicted value by the ANN-for-size without sampling time. Likely, the prediction validity of standard deviate described statistically is listed in Table 6.4 and 6.5. Their comparisons based on the ANN-for-std without sampling time were plotted in Figure 6.8.

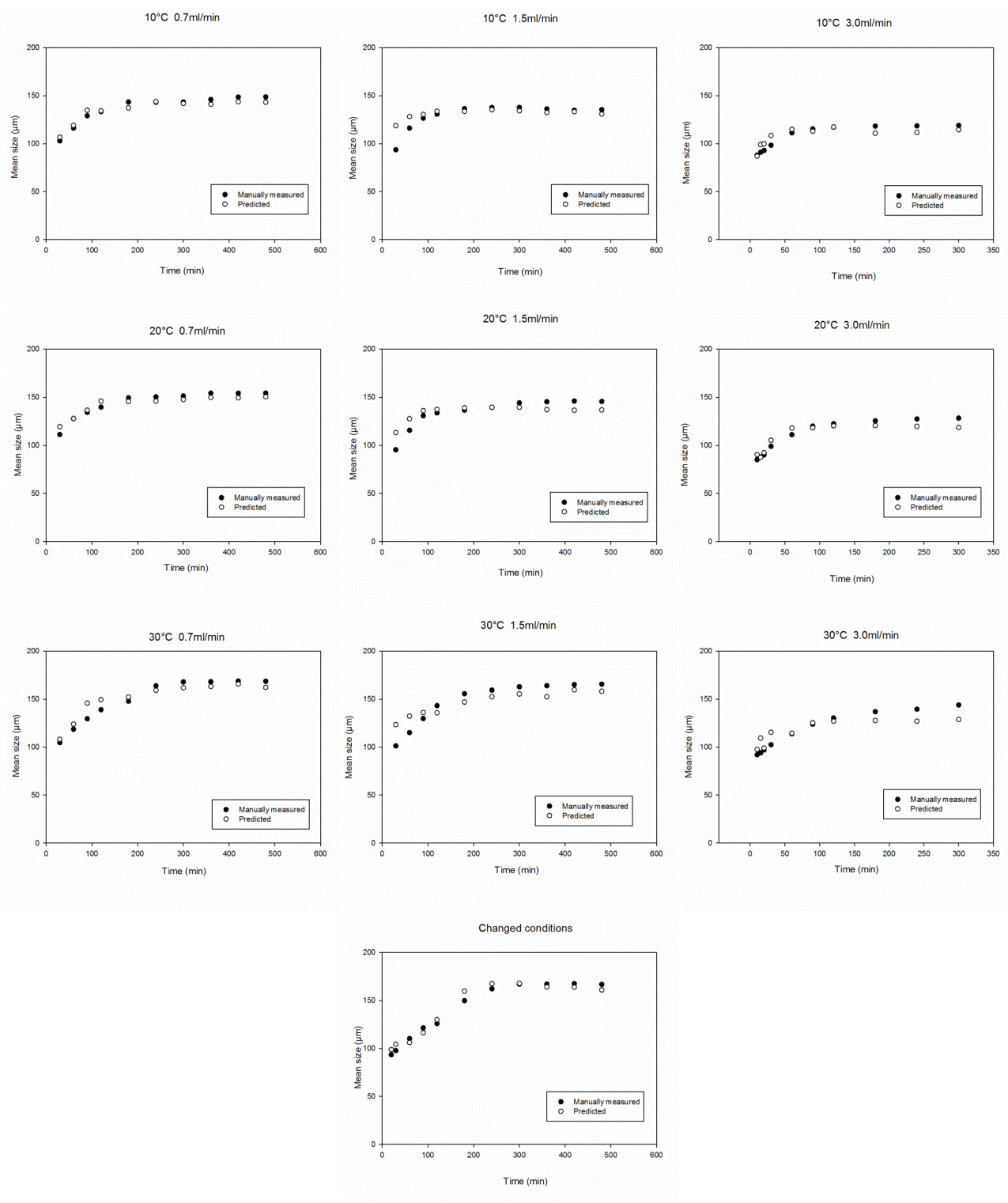


Figure 6.7: Comparison of manually measured mean size and predicted value for each crystallization run by ANN-for-size without sampling time

Table 6.2: Statistical parameters of ANN-for-size without sampling time for size prediction for both training and testing sets

Predicted size by ANN	RMSE	R ²	SSR
10°C, 0.7ml/min	4.18	91%	174
10°C, 1.5ml/min	9.28	51%	861
10°C, 3.0ml/min	6.66	76%	354
20°C, 0.7ml/min	4.62	88%	213
20°C, 1.5ml/min	8.76	68%	767
20°C, 3.0ml/min	6.23	89%	310
30°C, 0.7ml/min	7.5	89%	564
30°C, 1.5ml/min	11.3	74%	1276
30°C, 3.0ml/min	10.7	75%	912
Changed conditions	5.62	96%	319

Table.6.3: Statistical parameters of ANN-for-size with sampling time for size prediction for both training and testing sets

Predicted size by ANN	RMSE	R ²	SSR
10°C, 0.7ml/min	1.29	99.2%	16.5
10°C, 1.5ml/min	6.53	99.6%	0.81
10°C, 3.0ml/min	1.70	98.4%	23.2
20°C, 0.7ml/min	2.74	96.7%	61.0
20°C, 1.5ml/min	26.4	98.9%	1.63
20°C, 3.0ml/min	7.45	99.7%	0.97
30°C, 0.7ml/min	1.78	99.3%	31.2
30°C, 1.5ml/min	1.02	99.8%	10.5
30°C, 3.0ml/min	0.97	99.8%	7.51
Changed conditions	3.77	98%	142

Table 6.4: Statistical parameters of ANN-for-std without sampling time for STD prediction for both training and testing sets

Predicted STD by ANN	RMSE	R ²	SSR
10°C, 0.7ml/min	2.68	62%	72
10°C, 1.5ml/min	2.67	91%	72
10°C, 3.0ml/min	3.97	45%	110
20°C, 0.7ml/min	1.35	94%	18
20°C, 1.5ml/min	2.62	83%	69
20°C, 3.0ml/min	2.00	92%	28
30°C, 0.7ml/min	1.18	87%	14
30°C, 1.5ml/min	0.97	64%	8
30°C, 3.0ml/min	4.39	60%	135
Changed conditions	2.12	91%	45

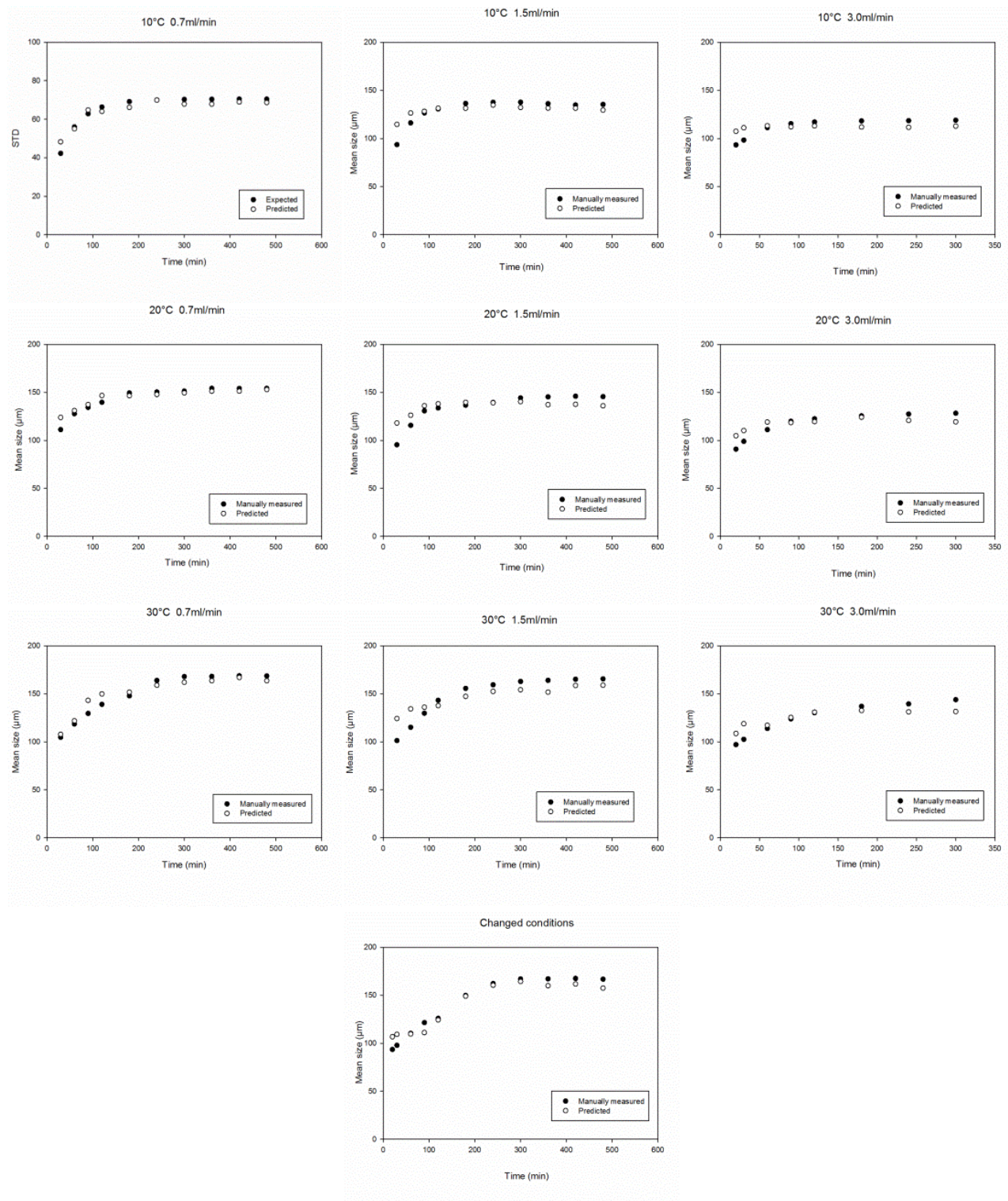


Figure 6.8: Comparison of expected standard deviation and predicted value for each crystallization run by ANN-for-std without sampling time.

Table 6.5: Statistical parameters of ANN-for-std with sampling time for STD prediction for both training and testing sets

Predicted STD by ANN	RMSE	R ²	SSR
10°C, 0.7ml/min	0.37	99.8%	1.35
10°C, 1.5ml/min	1.33	91%	18
10°C, 3.0ml/min	2.73	74%	52
20°C, 0.7ml/min	0.27	99.7%	0.74
20°C, 1.5ml/min	1.18	97%	14
20°C, 3.0ml/min	1.44	96%	14.5
30°C, 0.7ml/min	1.16	87%	13.4
30°C, 1.5ml/min	0.59	86%	3.2
30°C, 3.0ml/min	3.01	81%	64
Changed conditions	2.9	82.99%	84

6.4.4.3 CSD Prediction and Comparison

The CSD can be assumed to be either normal or log-normal distribution. The probability density functions for both the normal (pdf) and log-normal (pdf_{LN}) distributions are:

$$pdf = \frac{1}{\sqrt{2\pi}s^2} \exp\left(-\frac{(x-m)^2}{2s^2}\right) \quad (6.11)$$

$$pdf_{LN} = \frac{1}{\sqrt{2\pi}\sigma^2} \exp\left(-\frac{(x-\mu)^2}{2\sigma^2}\right) \quad (6.12)$$

The lognormal distribution has parameters μ and σ , which can be calculated from the mean m and standard deviation s of normal distribution.

$$\mu = \ln(m^2/\sqrt{s^2 + m^2}) \quad (6.13)$$

$$\sigma = \sqrt{\ln\left(\frac{s^2}{m^2} + 1\right)} \quad (6.14)$$

To determine which distribution can well fit the raw data, Shapiro-Wilk method [5] was selected to test the normality. In Shapiro-Wilk, the null hypothesis that the data follow a normally distributed population is tested. The null hypothesis is rejected if the p-value is smaller than a chosen alpha level. In our case, an alpha level of 0.05 was chosen. Table 6.6 shows the

number of samples from each run that passed either the normality (N) or log-normality (LN) test. The data passed the Shapiro-Wilk log-normality test 64% of the time which was more than the normality test pass rate of 0.1% so the data was modeled as a log-normal distribution with a corresponding log-normal mean and variance.

Table 6.6: Number of experimental samples that passed normality (N) or log-normality (LN) test.

	0.7 mL/min		1.5 mL/min		3.0 mL/min		Overall	
	N	LN	N	LN	N	LN	N	LN
10 °C	0/10	7/10	0/10	6/10	0/10	7/10	0/30	20/30
20 °C	1/10	5/10	0/10	7/10	0/10	5/10	1/30	17/30
30 °C	0/10	7/10	0/10	6/10	0/10	8/10	0/30	21/30
Overall	1/30	19/30	0/30	19/30	0/30	20/30	1/90	58/90

Table 6.7 and Figure 6.8 gives the lognormal parameters based on both manually measured and predicted mean size and standard deviation of counted crystals at each sampling time of the crystallization with changed operation conditions.

Table 6.7: Manually measured and predicted lognormal distribution parameters at each sampling time from the crystallization at changed operation conditions

Time (min)	Manually measured		Predicted (with sampling time)		Predicted (without sampling time)	
	μ	σ	μ	σ	μ	σ
20	4.45	0.43	4.47	0.39	4.50	0.44
30	4.43	0.55	4.51	0.41	4.55	0.44
60	4.59	0.471	4.57	0.45	4.57	0.44
90	4.69	0.47	4.62	0.44	4.67	0.43
120	4.72	0.47	4.77	0.40	4.77	0.43
180	4.93	0.40	4.90	0.40	5.01	0.37
240	5.02	0.37	4.99	0.38	5.05	0.38
300	5.06	0.35	5.03	0.38	5.05	0.39
360	5.05	0.36	5.04	0.38	5.02	0.41
420	5.06	0.34	5.05	0.38	5.02	0.41
480	5.06	0.34	5.05	0.39	5.00	0.41

Figure 6.9 show how the CSD model predictions compare to the raw histogram experimental data and the estimated probability density function (pdf) of the raw data. They show the samples taken at 20, 30, 60, 90, 120, 180, 240, 300, 360, 420 and 480 minutes for the crystallization experiment with changed conditions. The image-based multi-resolution sensor does a good job of matching both the smoothed data and the raw data histograms. ANN models built with sampling time can simulate better than those without sampling time.

6.5 Conclusions

An image-based approach of texture analysis combining thresholding and wavelet-fractal with ANN for the prediction of CSD was proposed and applied on a case study. This method could successfully and automatically identify crystal clusters and estimate the texture by means of FD and wavelet energy signature. The FD transformation tendency for different crystallization operation conditions had been investigated with the results that higher FD can be obtain at higher flowrate for a given temperature and at lower temperature for a given flowrate. The pattern of FD and crystal mean size for different crystallization conditions were compared showing their similarity. The relationship of FD and crystal mean size had been extracted and built as an ANN model for predicting crystal mean size as well as for standard deviation. The predicted CSD in lognormal probability density function was plotted and compared with experimental data. These results attest the potential application of the proposed method for crystal production process monitoring and control.

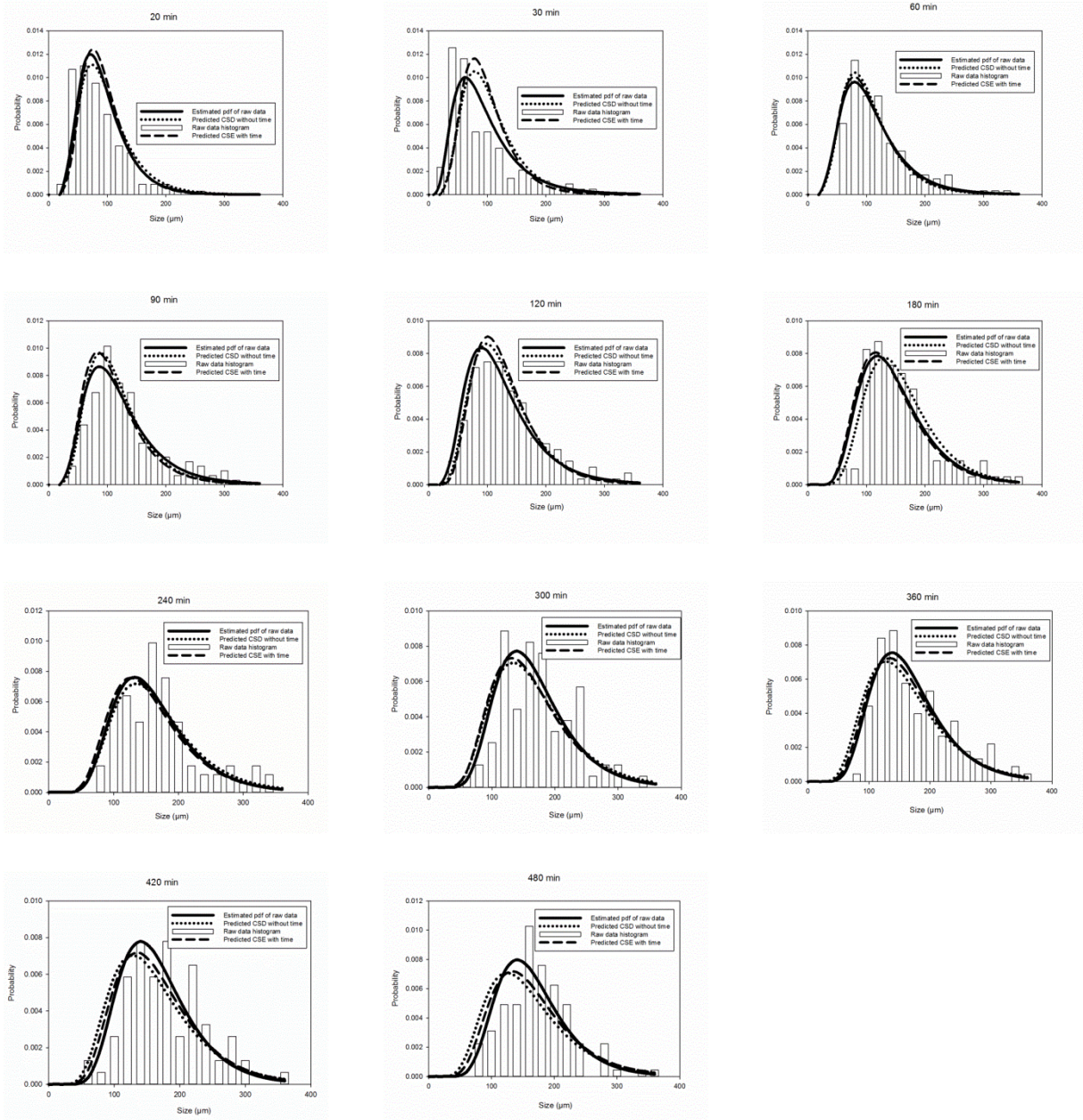


Figure 6.9: Comparison of predicted CSD, raw histogram and the smoothed approximation with the manually measured lognormal distribution parameters at each sampling time from the crystallization at changed operation conditions

6.6 Reference

- [1] H. Tang, K. C. Tan, Y. Zhang, Neural networks: computational models and applications, 2007.
- [2] S. Haykin, Neural network – a comprehensive foundation MacMillan Publishing Company, 1994.

- [3] J. S. R. Jang, C. T. Sun, E. Mizutani, Neuro-Fuzzy and soft computing, Prentice Hall Inc. , New Jersey, 1997.
- [4] M. Grosso, G. Cogoni, R. Baratti, J. A. Romagnoli, Stochastic Approach for the prediction of PSD in crystallization processes: formulation and comparative assessment of different stochastic models, Industrial & Engineering Chemistry Research, 50 (2011) 2133-2143.
- [5] S. S. Shapiro, M. B. Wilk, An analysis of variance test for normality (complete samples), Biometrika, 52 (1965) 591–611.

CHAPTER 7. CONCLUSIONS & RECOMMENDATIONS

7.1 Conclusions

This doctoral thesis has focused on the development of algorithms and models for image-based process monitoring directed at online monitoring of particulate processes such as crystallization, comminution and granulation. The present work systematically addressed the problems of image acquisition setup, image analysis, feature extraction, statistical monitoring/predictive models and experimental validation. Methodologies have been designed and proposed, that has direct potential for application in particulate processes in a wide range of industries including chemical, pharmaceutical, mineral processing among others to maintain desired process performances.

The proposed methodologies combined tools from different disciplines - specifically in the areas of image processing, data mining modelling and process control theory. The main contributions are outlined in the following:

1. Multi-resolution fuzzy clustering approach was developed and implemented for the segmentation of touching areas on particle images in Chapter 2. A particle image from a laboratory scale online image acquisition system was used to test the validity of the proposed method. Noise removal was achieved through wavelet decomposition while segmentation was performed with Fuzzy C-mean clustering. The touching regions can be successfully identified and divided by this algorithm.
2. An algorithm combining the usage of intensity and geometry features of touching and overlapping areas was developed and successfully used to separate objects in Chapter 3. The overlapping areas show distinct characteristics in intensity, that is their intensity is lower than those from objects but not low enough to be considered as those from backgrounds. The key

feature of overlapping regions is the existence of a high level of concavity on the boundaries. This method was implemented to provide a robust separation and its efficiency was found to be superior to existing methods.

3. An automatic image-based estimation of texture analysis to capture the size information when overlapping problems become severe was proposed and performed in Chapter 4. From the viewpoint of roughness, as the texture, it will change of rough to flat as crystals grow. The texture was represented by statistical measurements such as energy and FD. FD estimation by the proposed method was adopted on a serial of crystal images from a crystallization process and showed an interesting inverse changing tendency to the manually measured mean size during crystallization.
4. To use the texture information, predictive models and statistical control models were designed and built in Chapter 5. The relationship between texture features and the manually measured mean size was capture/linked by PLS models which could predict the mean size from new coming images. PCA models built based on historical normal process data could tell whether the new point representing current process status was on track in mean size. The extent of mean size deviation could also be analyzed through PCA models.
5. An image-based multi-resolution-ANN sensor for online prediction of crystal size distribution was designed in Chapter 6. ANNs, as the globe models to be able to be applied on nonlinear plant in the whole operating range, was established. Not only the mean size, but also the size distribution was predicted by this sensor. The efficiency of the ANNs was confirmed by comparing with manually measured parameters.
- 6.

7.2 Future Work

There are several ways that future research can extend this dissertation research:

1. The proposed frameworks for image-based monitoring can be combined with feedback controllers and applied to specific particulate processes, or can be used alone to detect failure. It would be interesting to compare the control/detection performances by the proposed frameworks and by traditional methods. The differences/agreements will help to develop and validate the frameworks.
2. The image-based monitoring frameworks may combine with the non-isothermal crystallization model framework, producing a crystallization monitoring and control framework. This would incorporate the image-based monitoring frameworks into a model-predictive controller. It would forecast the mean size set point trajectory throughout the process. It would either adjust the antisolvent feed rate or temperature to create a new set point trajectory if substantial variation between the measured mean size and the set point exists.
3. The proposed image processing methods including segmentation and texture analysis can be extended to various particle size scales with appropriate magnification systems, from nano, micro, meso to macro. Thus, these methods can be applied on images from SEM/TEM, optical microscope and regular optics.
4. The executive time of the image-based monitoring sensors may be investigated with the needed monitoring stages of an industrial manufacturing process involving particles, either accelerating the executive time or designing taken-actions to somewhat delay. This would allow the sensors provide in time outputs for the process.

APPENDIX: LETTERS OF PERMISSION

Title: Multi-resolution fuzzy clustering approach for image-based particle characterization for particle systems

Author: B. Zhang,A. Abbas,J.A. Romagnoli

Publication: Chemometrics and Intelligent Laboratory Systems

Publisher: Elsevier

Date: May 2011

Copyright © 2011, Elsevier

Logged in as:

Bing Zhang

Order Completed

Thank you very much for your order.

This is a License Agreement between Bing Zhang ("You") and Elsevier ("Elsevier"). The license consists of your order details, the terms and conditions provided by Elsevier, and the payment terms and conditions.

License number 3063771085508

License date Jan 07, 2013

Licensed content publisher Elsevier

Licensed content publication Chemometrics and Intelligent Laboratory Systems

Licensed content title Multi-resolution fuzzy clustering approach for image-based particle characterization for particle systems

Licensed content author B. Zhang,A. Abbas,J.A. Romagnoli

Licensed content date May 2011

Number of pages 10

Type of Use reuse in a thesis/dissertation

Portion full article

Format both print and electronic

Are you the author of this Elsevier article? Yes

Will you be translating? No

Order reference number

Title of your thesis/dissertation Digital Image-Based Frameworks for Monitoring and

Controlling Particulate Systems

Expected completion date Mar 2013

Estimated size (number of pages) 100

Elsevier VAT number GB 494 6272 12

Permissions price 0.00 USD

VAT/Local Sales Tax 0.00 USD / GBP

Total 0.00 USD

Copyright © 2013 Copyright Clearance Center, Inc. All Rights Reserved. Privacy statement.

ELSEVIER LICENSE TERMS AND CONDITIONS

Jan 07, 2013

This is a License Agreement between Bing Zhang ("You") and Elsevier ("Elsevier") provided by Copyright Clearance Center ("CCC"). The license consists of your order details, the terms and conditions provided by Elsevier, and the payment terms and conditions.

All payments must be made in full to CCC. For payment instructions, please see information listed at the bottom of this form.

Supplier Elsevier Limited

The Boulevard, Langford Lane

Kidlington, Oxford, OX5 1GB, UK

Registered Company Number 1982084

Customer name Bing Zhang

Customer address 999 N. 9TH. STR. Baton Rouge, LA 70802

License number 3063771085508

License date Jan 07, 2013

Licensed content publisher Elsevier

Licensed content publication Chemometrics and Intelligent Laboratory Systems

Licensed content title Multi-resolution fuzzy clustering approach for image-based particle characterization for particle systems

Licensed content author B. Zhang, A. Abbas, J.A. Romagnoli

Licensed content date May 2011

Licensed content volume number 107

Licensed content issue number 1

Number of pages 10

Start Page 155

End Page 164

Type of Use reuse in a thesis/dissertation

Portion full article

Format both print and electronic

Are you the author of this Elsevier article? Yes

Will you be translating? No

Order reference number

Title of your thesis/dissertation Digital Image-Based Frameworks for Monitoring and
Controlling Particulate Systems

Expected completion date Mar 2013

Estimated size (number of pages) 100

Elsevier VAT number GB 494 6272 12

Permissions price 0.00 USD

VAT/Local Sales Tax 0.0 USD / 0.0 GBP

Total 0.00 USD

Title: Automatic image-based estimation of texture analysis as a monitoring tool for crystal growth

Author: B. Zhang,A. Abbas,J.A. Romagnoli

Publication: Chemometrics and Intelligent Laboratory Systems

Publisher: Elsevier

Date: 15 February 2013

Copyright © 2013, Elsevier

Logged in as:

Bing Zhang

Order Completed

Thank you very much for your order.

This is a License Agreement between Bing Zhang ("You") and Elsevier ("Elsevier"). The license consists of your order details, the terms and conditions provided by Elsevier, and the payment terms and conditions.

License number 3063780009717

License date Jan 07, 2013

Licensed content publisher Elsevier

Licensed content publication Chemometrics and Intelligent Laboratory Systems

Licensed content title Automatic image-based estimation of texture analysis as a monitoring tool for crystal growth

Licensed content author B. Zhang,A. Abbas,J.A. Romagnoli

Licensed content date 15 February 2013

Number of pages 10

Type of Use reuse in a thesis/dissertation

Portion full article

Format both print and electronic

Are you the author of this Elsevier article? Yes

Will you be translating? No

Order reference number

Title of your thesis/dissertation Digital Image-Based Frameworks for Monitoring and
Controlling Particulate Systems

Expected completion date Mar 2013

Estimated size (number of pages) 100

Elsevier VAT number GB 494 6272 12

Permissions price 0.00 USD

VAT/Local Sales Tax 0.00 USD / GBP

Total 0.00 USD

Copyright © 2013 Copyright Clearance Center, Inc. All Rights Reserved. Privacy statement.

ELSEVIER LICENSE TERMS AND CONDITIONS

Jan 07, 2013

This is a License Agreement between Bing Zhang ("You") and Elsevier ("Elsevier") provided by Copyright Clearance Center ("CCC"). The license consists of your order details, the terms and conditions provided by Elsevier, and the payment terms and conditions.

All payments must be made in full to CCC. For payment instructions, please see information listed at the bottom of this form.

Supplier Elsevier Limited

The Boulevard,Langford Lane

Kidlington,Oxford,OX5 1GB,UK

Registered Company Number 1982084

Customer name Bing Zhang

Customer address 999 N. 9TH. STR Baton Rouge, LA 70802

License number 3063780009717

License date Jan 07, 2013

Licensed content publisher Elsevier

Licensed content publication Chemometrics and Intelligent Laboratory Systems

Licensed content title Automatic image-based estimation of texture analysis as a monitoring tool
for crystal growth

Licensed content author B. Zhang,A. Abbas,J.A. Romagnoli

Licensed content date 15 February 2013

Licensed content volume number 121

Licensed content issue number

Number of pages 10

Start Page 42

End Page 51

Type of Use reuse in a thesis/dissertation

Portion full article

Format both print and electronic

Are you the author of this Elsevier article? Yes

Will you be translating? No

Order reference number

Title of your thesis/dissertation Digital Image-Based Frameworks for Monitoring and Controlling Particulate Systems

Expected completion date Mar 2013

Estimated size (number of pages) 100

Elsevier VAT number GB 494 6272 12

Permissions price 0.00 USD

VAT/Local Sales Tax 0.0 USD / 0.0 GBP

Total 0.00 USD

VITA

Bing Zhang was born in Hubei, China in 1981. She enrolled at Wuhan University of Science and Technology in Sep 1999, and graduated with a Bachelor of Chemical Engineering. After that she enrolled at Tsinghua University in August 2003, and graduated with a Master degree in chemistry in June 2006..

After receiving her master degree, she worked for C-bons Group in Hubei, China. She was involved in various research projects of inventing personal care products to design formula, perform laboratory experiment, develop pilot-scale production, and establish standards for purchasing raw material and test criteria for end products.

In the fall of 2008, she traveled to Louisiana where she enrolled as a doctoral student in Chemical Engineering at Louisiana State University. There she joined Professor Jose Romagnoli's Process Systems Engineering Research Group in December 2008. During her doctoral program, the main focus of her research was the development of image-based frameworks for monitoring and controlling particulate systems. She expects to receive the Doctor of Philosophy degree in Chemical Engineering in May 2013. To date she is the author of five peer-reviewed journal articles and conference proceedings on the research area of process system engineering. Her research has also been presented at three major international conferences.